CHARACTERIZATION OF EXTREMELY LOW-LEVEL OPTICAL ABSORPTION AND SCATTERING IN CRYSTALLINE MATERIALS FOR HIGH-ENERGY LASERS APPLICATIONS

by
Jessica G Ma

A dissertation submitted to Johns Hopkins University in conformity with the requirements for

the degree of Doctor of Philosophy

Baltimore, Maryland
March 2021

Abstract

Window materials used in the current generation of high-energy laser (HEL) systems cannot be used for next-generation systems since these aim to operate at or near the megawatt level under CW operation. Related intensities will lead to beam distortion and possibly damage of current optical materials. These materials include polycrystalline spinel and single-crystal sapphire – both have undesirable optical absorption and scattering near the 1 μm wavelength that limit their performance in future HEL applications. However, phenomena associated with optical absorption and scattering have not been comprehensively studied for the crystalline materials of interest and, as a result, the physical mechanisms underlying both optical losses in these materials are not well understood.

The overall goal for this research is to obtain a comprehensive understanding of low-level absorption and scattering in sapphire and spinel at and near the 1 μm wavelength region using the commercially available samples. In this work, ultraviolet-visible spectroscopy and photothermal common-path interferometry are used to measure bulk and surface absorption losses in different samples in the UV-visible-near-infrared wavelength regions. The absorption coefficient values obtained are in the range of 10^{-5} to 10^{0} cm^{-1} and increase as the wavelength decreases. In addition, scattering measurements on samples with different surface polishing conditions are made at 405, 532, 633, 1064, and 1550 nm using an instrument developed to assess the bidirectional scatterance probability distribution function. The total integrated scatterance is in the range of 10^{-5} to 10^{-1} and increases for all samples as the wavelength decreases. Different absorption and scattering models are applied to interpret the measured data. Materials characterization techniques including positron annihilation lifetime spectroscopy, laser ablation inductively coupled plasma mass spectroscopy, secondary ion mass spectroscopy, Raman spectroscopy, atomic force microscopy, and optical and electron microscopies are utilized to characterize bulk and surface defects in different samples. Overall, the measurement results indicate that both weak absorption and scattering losses are strongly related to defect structures such as lattice disorder and impurities that were introduced during crystal growth or post-growth processing. Understanding these defects and their contributions to optical loss can lead to improved manufacturing and processing methods.

Primary Reader: Prof. James Spicer

Secondary Readers: Prof. Michael Thomas, Prof. Patricia McGuiggan

Acknowledgments

I would like to first thank Professors Patricia McGuiggan, Tyrel McQueen, James Spicer, Michael Thomas, and June Wicks for serving on my thesis committee. I am thankful to Professor James Spicer for inviting me to join his research group and guiding me through this adventurous but fantastic journey. Many times in the past five years and half, I thought I would not make to this final destination but somehow he pushed me through, it must be these chocolates I shared with him that provided him enough magic power. I am also deeply grateful to Professor Michael Thomas for introducing me to the world of optical materials. I have to admit that as a student coming from a mechanical engineering background with little knowledge of electromagnetics and optics, I struggled a lot but also learned much more. Luckily, I have been able to grasp his expertise and advice all the time that I really enjoyed talking to him and “bothering” him. I would also like to offer my special thanks to Professor Patricia McGuiggan for all the experimental and intellectual support, but more importantly, her emotional support accompanied me so well in the past few years. As a female researcher, I have always been inspired by her hardworking attitude. I would like to extend my sincere thanks to Professors Tyrel McQueen and June Wicks for their insightful comments and suggestions to this work as their valuable expertise can help me to make further improvements. I would also like to thank Dr. Kenneth Livi and Mr. Sammuel Norris for helping me to acquire different electron micrographs and providing subject expertise. Furthermore, I also want to thank Dr. Timothy Mueller for offering generous assistance on the DFT calculations. Additionally, I wish to offer special thanks to Ms. Erin Pyce from IIC for training me on different optical microscopes and also taking a few optical micrographs for me at the beginning of the pandemics when the access to the lab was restricted. Last but not least, I want to thank Dr. Freya

George and Dr. Robert Holder from Dr.Daniel Viete's research group for performing the mass spectroscopy measurements and being generous to share with me their knowledge.

Outside of JHU, I would like to thank Mr. Marc Airola, Dr. David Brown, Dr. Dajie Zhang from Johns Hopkins Applied Physics Laboratory, Dr.Xunxiang Hu, Dr.Congyi Li, and Professor Brian Wirth from the Oak Ridge National Laboratory and the University of Tennessee. I want to thank Mr. Marc Airola and Dr. David Brown training me on different instruments at APL and sharing their valuable knowledge with me. I would like to express my special gratitude to Dr. Dajie Zhang answering all of my questions regarding chemistry and materials science all the time. He has always been like a guru to me and talking to him has always been my last resort if I could not find answers to my problems using all other ways. I am very thankful to Dr. Xunxiang Hu, Dr. Congyi Li, and Professor Brian Wirth, for making the positron measurements and providing me with their insights on the measurement results.

I would not have survived without the support and love I acquired from the departmental staffs and my friends from other research labs across the campus. Special thanks to Jeanine Majewski, Ellen Libao, Kyra Vocci, Meghan Tully, Ada Simari, Tanea Melvin, Sainjali Hussain, Phillip Chapman, and Bryan Crawford for administrative and lab support although some of you already left DMSE. I really enjoyed talking to you about different things. I am deeply grateful to my friends and colleagues from other research labs at JHU and outside of JHU for offering me assistance both in the lab and in my life. Especially, to Yan Cheng, Helen Hou, Andrew Jiang, Anita Li, Chenyang Li, Alliuson Liu, Dihui Ruan, Ju Xue, and Judith Yang, I would not be able to make this far in graduate school and in my life without meeting you.

I felt so lucky for joining a wonderful research group at JHU. Dr. Michael Brupbacher and Dr. Fan Zeng, thank you so much for guiding me through the graduate school life during the first half of this journey. Bella Hunt and Adam Peters, thank you very much for making the second half so wonderful that we together have had a lot of fun. Although we have been working on very different research projects, we all love to take power naps in the office at different times during the day. Hopefully our dreams of having comfortable couches and group pets in the office will come true in the near future. Lorna Alvarez and Emily Chambers, although I have not interacted with you for long, I really appreciate your insights to my work when we have group meetings. Since I will be in Baltimore for a while after graduate school, I have the luxury to bother you all and I will do so.

I want to dedicate this dissertation to my parents, Mei Wang and Huiwu Ma, and my fiancée, Qingjie Li. Thank you all for giving me infinite love and tolerance during all these tough times. It has never been easy as a first-generation immigrant in the U.S. I still remember that fourteen years ago, when my family and I first landed in the U.S., we felt so helpless since we barely understood and spoke English. But my parents were not afraid to live in this strange and tough environment and because of them I struggled through and gained many eye-opening experiences. Thank you, mom and dad, for believing in me all the time. Qingjie, meeting you at JHU has been the best thing in my life and I cannot wait to start a new life journey with you.

To my cats Huzi and Sake, thank you for staying up late with me for many nights.

To my grandparents who raised me, I finally grew up and I miss you.

Table of Contents

List of Tables

List of Figures

Chapter 1. Introduction

1.1 General Background

1.1.1 High Energy Laser Applications

High-energy laser (HEL) systems produce very high optical fluences or intensities. Their primary applications include both defensive and offensive weapons to block ballistic missiles and achieve a long-distance precision strike [1]–[4]. Pulsed HELs have also been used in the materials processing field including cutting and welding [5]. HEL weapons demonstrate several advantages including speed of light delivery, undercover operation, high precision, low collateral damage, and a wide operational range that can include non-lethal, disruptive, or destructive effects [1]. Furthermore, different types of HELs such as hydrogen fluoride (HF) and deuterium fluoride (DF) lasers, the chemical Oxygen-Iodine laser, and solid-state lasers have been developed over the last five decades with power output from several kilowatts to 1 MW and operating wavelengths from 1 to 10 μm [1]. Among these different HELs, solid-state lasers require the gain medium to be solid (i.e. doped crystalline materials and optical fibers) and this class of laser has received significant attention in recent years for the following reasons:

1. Major advances in solid-state laser technology have allowed these lasers to be manufactured easily and efficiently;
2. Diode pumping resulted in a significant reduction of the price per watt since the 1980s which made the solid-state lasers more affordable [2], [3] and also increased the average power outputs;
3. Increased durability of solid-state lasers has increased the service lifetimes of critical components.

Currently, solid-state high-power lasers operate near the 1 μm wavelength region with a power output up to tens of kilowatts under continuous wave (cw) emission or hundreds of terawatts under pulsed mode operation and the optical powers associated with these systems are generally limited by the materials used in their optics [1], [3], [6].

1.1.2 Motivation and Introduction Overview

Window materials (i.e. materials that separate the lasing medium from the surrounding environment) used in the current generation of HEL systems cannot be used for next-generation systems since these aim to operate at or near the megawatt level under cw operation [6]–[8]. Such a high operational power would result in nonuniform heating in the window materials leading to thermally-induced beam distortion and beam quality degradation. Additionally, this heating could also induce different types of thermal stresses that could cause structural degradation in these materials [8]–[10]. Therefore, the ideal window material candidates should have excellent optical, thermal, and mechanical properties that allow them to sustain exposure to megawatt level powers. Previously, numerous studies have analyzed optical materials such as calcium fluoride (CaF_2) and fused silica due to their excellent optical properties, and fused silica windows are commonly used in current HEL systems [6], [8], [9]. However, these materials are mechanically weak, are vulnerable to thermal shock and fracture resulting from a large thermal load, and can also fail to withstand other aspects of the harsh operating environment. New window material candidates must be considered for the next-generation of HEL. This study mainly investigates the optical and physical properties of synthetic, c-plane, single-crystal sapphire (Al_2O_3) and polycrystalline spinel ($MgAl_2O_4$) since both materials have the potential to serve as window materials for future HEL applications. Specifically, this work focuses on studying the low-level absorption and scattering observed in sapphire and spinel in the near-infrared wavelength region as well as the defect structures associated with the optical losses.

The remaining parts of the introduction address several aspects to provide background for the issues associated with the optical materials of interest. The next two sections will discuss the problems associated with the current window materials as well as the requirements of HEL windows. Then, basic knowledge of light-materials interactions will be presented to provide a better understanding of the optical properties of sapphire and spinel. Materials growth methods along with the common defects and disorders present in the materials of interest will also be examined. Lastly, an overview of the remaining thesis work will be provided.

1.1.3 Low-Level Optical Losses in Sapphire and Spinel

Simple considerations of electronic structure indicate that materials such as fused silica, CaF_2, sapphire, and spinel should have near zero absorption around the 1 μm wavelength region because this region resides well below the bandgap of these materials. The transparent region typically defines a wavelength range where materials should have zero absorption if no defect states are present. Figure 1.1, shows wavelength versus optical extinction coefficient (scattering plus absorption) for fused silica in the range of 0.1 to 100 μm [11]. The left region of the graph includes the upper part of the Urbach tail and represents the classical electronic absorption edge of fused silica. The multiphonon absorption regime appears on the other side of the graph. Both absorption phenomena are well-characterized and their mechanisms are clearly understood [6]. The region in between the two absorption regimes is typically where the material is considered to be fully transparent. However, as the absorption model associated with the solid red line in Fig. 1.1 indicates, this is not the case and there is residual absorption near the 1μm wavelength region in fused silica and this loss is commonly referred to as the weak absorption tail. Beyond absorption, the scattering coefficient of fused silica is on the order of 10^{-6} cm^{-1} in the same region. Density variations are responsible for scattering and related mechanisms are relatively well-understood compared to the ones responsible for weak absorption [6].

The weak absorption tail was first observed in amorphous semiconductors in 1972 [12]. Other materials such as optical fibers and certain types of glasses were also found to exhibit the weak absorption phenomenon in the transparent region. Among these different materials, the weak absorption tail is generated from sublevels below the conduction band edge and above the valence band edge and is related to the additional states generated by lattice disorder, impurities, and other defects [6]. For example, the weak absorption tail in Ge-Sb-Se optical fibers was found to be related to dangling bonds [13]. It is generally assumed that material defects are responsible for the loss in this region, but specific mechanism-based descriptions have not been satisfactorily established by any work to date. Even so, experimental measurements tend to indicate that the

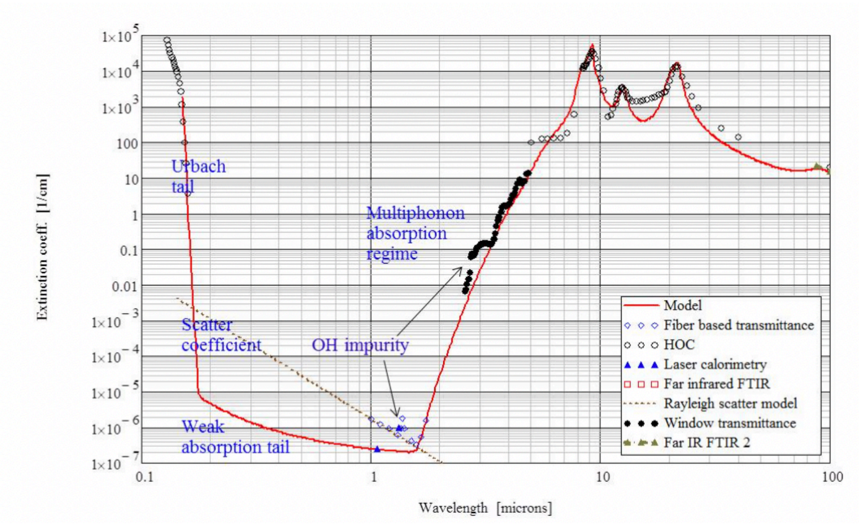

Figure 1.1. The extinction coefficient of high purity fused silica as a function of wavelength. The scatter coefficient model is the dotted curve and the absorption coefficient model is the solid curve. Experimental results are plotted from a variety of sources [6].

weak absorption tail represents a background continuum absorption between the electronic band gap edge and the multiphonon absorption edge as shown in Fig. 1.1 [6]. Despite lacking concrete physical mechanisms associated with absorption in this region, an empirical mathematical model can be created for the absorption coefficient β_{abs} based on data collected from different amorphous semiconductors which has the following form:

$$\beta_{abs}(v) = \beta_0 \exp\left(\frac{v}{v_0}\right) \tag{1.1}$$

where v is the frequency and β_0 and v_0 are parameters used to fit the model the experimental data [6]. The weak absorption tail phenomenon is likely to be an extrinsic effect, meaning the tail form is affected by different impurities and defects introduced during growth and post-growth treatments.

The weak absorption tail has not been fully characterized for crystalline materials, and the lack of experimental measurements in this region is due, in part, to the high quality of current materials for the applications in which they are used [6]. However, this is not the case for the next generation of HEL since weak absorption in current laser materials can lead to catastrophic failure. Despite the lack of absorption data, various studies have included isolated measurements that suggest the existence of the weak absorption tail in these materials. Both Figs. 1.2 and 1.3 show absorption models and data from the *Handbook of Optical Constants* indicating that absorption of the form of the weak absorption tail is present in polycrystalline spinel and in single crystal sapphire [6]. Note that the absorption coefficient for spinel is on the order of 10^{-3} cm^{-1} and the one for sapphire is on the order of 10^{-4} cm^{-1} in the 1 μm wavelength region. Both are much larger than the coefficient for high purity fused silica (10^{-7} cm^{-1}), and this makes these laser materials more vulnerable to thermal lensing effects. One potential cause for the higher values is the different levels of impurities and defects being introduced into the materials during the manufacturing process. Another cause could be related to the material grain structure since absorption and scattering levels are typically higher in polycrystalline materials than in single crystals due to the presence of grain boundaries.

There are several scattering sources for all window materials: surface topography, surface contamination, bulk index fluctuations, and bulk defects. Surface topography mainly refers to the surface roughness along with scratches and digs due to grinding and polishing which cause phase deviations of the light wavefront when it is transmitted through or reflected from the window. Surface contamination typically includes dust particulates, polishing solution residue, and other impurity elements. Bulk index fluctuations are caused by subsurface damage and bulk defects such as dislocations, vacancies, strain, grain boundaries, and planar defects. Lastly, impurity aggregates, pores, and bubble inclusions are also bulk defects that produce scattering loss.

Therefore, in the next section, evaluations of sapphire and spinel will be performed to examine the impact of the low-level, near-infrared absorption on their performance as exit window materials for the next-generation HEL. The required absorption loss level for both materials will also be discussed.

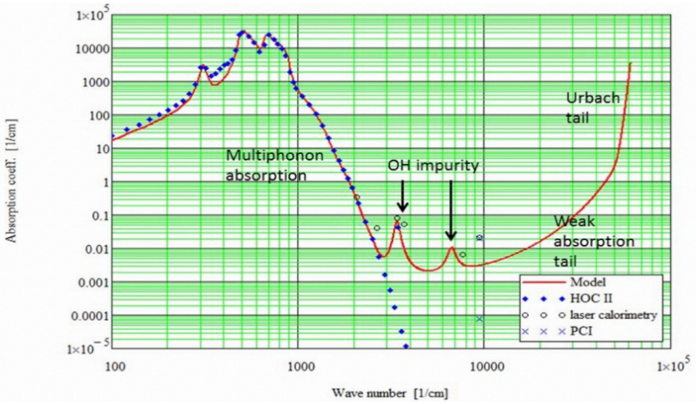

Figure 1.2. The absorption coefficient of polycrystalline spinel as a function of wave number. Data obtained from multiple sources [6].

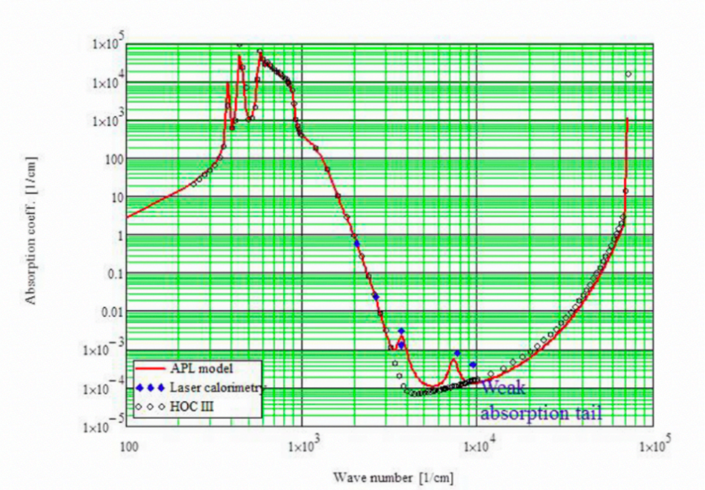

Figure 1.3. The absorption coefficient of single crystal sapphire as a function of wave number. Data obtained from multiple sources [6].

1.1.4 HEL Window Requirements

While scattering mainly causes the beam path deviation from its desired destination when a laser beam travels through a window, optical absorption induces photothermal heating within the window medium that ultimately leads to beam distortion. Since scattering does not cause any changes within the window material, the required scattering level primarily depends on the operating environment as well as damage thresholds of other optical components within a HEL. It is generally recommended that the scattering coefficient of a HEL window to be less than 10^{-3}

cm^{-1} [14]. On the other hand, given the low-level absorption loss in sapphire and spinel at the near-infrared wavelength region, thermal lensing issues must be considered. Thermal lensing is related to the process of beam defocusing and distortion due to thermally-induced phase aberrations. When a window absorbs a portion of the incident laser beam, local heating occurs that leads to the changes in the refractive index along with the physical path length, which ultimately alters the incident beam path and shape. Furthermore, temperature gradients within the window also generate mechanical stresses that can eventually fracture the material. The ideal HEL window candidate should not only transmit the laser beam with minimum distortion but also needs to be strong and tough to sustain a large power load under various environments. Previously, a set of figures of merit (FOM) were developed to characterize the impact of optical distortion and stressed-induced failure modes to evaluate different HEL window material candidates using their physical and optical properties [8], [9]. Here, three evaluation criteria (required window thickness, allowable peak fluence due to thermal lensing, and allowable peak fluence due to planar stress) will be used to evaluate the materials of interest (single crystal sapphire and polycrystalline spinel) against two other popular HEL window candidate choices (fused silica and fusion-cast CaF_2). Among these materials, fused silica is known to have the lowest optical absorption (as low as 10^{-7} cm^{-1}) at 1 μm while CaF_2 has a negative thermo-optic coefficient (dn/dT) that could greatly reduce the optical distortion but both materials are less mechanically durable compared to sapphire and spinel [6], [8]. Although sapphire and spinel have a relatively higher optical absorption at 1 μm (10^{-5}/cm to 10^{-3}/cm) and a positive dn/dT, both materials have excellent mechanical and thermal properties that allow them to operate in many extreme environments [14]. Lowering the optical absorption in both materials could help them outperform the other two candidates if all evaluation criteria are considered.

Three FOM quantities will be used to evaluate each window candidate at the laser operating wavelength of 1 μm. The first FOM is the required window thickness, L, (under the pressure differential is of the order of 1 atm) and it is given by

$$L = \frac{353(\frac{\pi}{4})^{\frac{1}{2}m} D(\frac{D}{cm})^{\frac{1}{m}}}{\sqrt{\sigma_c}} \tag{1.2}$$

where *D* is the window diameter, *m* is the Weibull shape factor, 1/cm indicates that the window diameter should be provided in centimeters, and σ_c denotes the characteristic strength (in Pa) of a material when 1-cm^2 of it is subjected to an equi-axial tensile stress. The second FOM considered is the allowable peak fluence due to the optical distortion and it is expressed as

$$J_{All}^{O.D} = \frac{1.668}{k} \frac{C_p}{\chi \beta_a L} \tag{1.3}$$

where t represents the time, k is the propagation constant, $\frac{2\pi}{\lambda}$, C_p is the volumetric heat capacity, χ is the thermal lensing coefficient, L is the required thickness, and β_a is the optical absorption coefficient [9]. The thermal lensing coefficient is a combination of two optical distortion coefficients, χ_+ and χ_-, that can be expressed as

$$\chi = |\chi_+| \sqrt{1 + G_0 (\frac{\chi_-}{\chi_+})^2} \tag{1.4}$$

where G_0 is a parameter that depends on the Gaussian beam truncation parameter given in [8] and equals 0.755. Both χ_+ and χ_- are given as

$$\chi_+ = \frac{dn}{dT}(n-1)\alpha(1+\upsilon)\frac{n^3 \alpha E}{4}(q_{\parallel} + q_{\perp}) \tag{1.5}$$

$$\chi_- = \frac{n^3 \alpha E}{4}(q_{\parallel} - q_{\perp}) \tag{1.6}$$

where n represents the index of refraction, α is the thermal expansion coefficient, υ is the Poisson ratio, E is the elastic modulus and $q_{\parallel}$ and $q_{\perp}$ are related to the stress-optic coefficients, q_{11}, q_{12}, and q_{44} by

$$q_{\parallel} + q_{\perp} = q_{11} + q_{12} + \frac{j_3}{5}[q_{44} - (q_{11} - q_{12})] \tag{1.7}$$

$$q_{\parallel} - q_{\perp} = q_{11} - q_{12} + \frac{j_3}{5}[q_{44} - (q_{11} - q_{12})] \tag{1.8}$$

where j_3 is given as

$$j_3 = \frac{5c_{44}(3K + 4G)}{G(9K + 8G) + 6c_{44}(K + 2G)} \tag{1.9}$$

where K and G are bulk and shear moduli, respectively [8], [9]. Note that Eq. (1.7) and Eq. (1.8) apply to single crystal materials where anisotropy exists. For isotropic materials, $q_{\parallel} + q_{\perp}$ and $q_{\parallel} - q_{\perp}$ simply equal $q_{11} + q_{12}$ and $q_{11} - q_{12}$, respectively. The last FOM characterizes the allowable peak fluence due to planar stress and is given by [9]

$$J_{All}^{P.S} = \frac{\frac{3.52C_p}{\alpha E}S^*}{B^*D^{-1}(\frac{D}{cm})^{\frac{1}{m}} + \beta_a(\frac{D}{cm})^{\frac{2}{m}}} \tag{1.10}$$

where

$$S^* = \frac{\sigma_c}{4 * (\frac{\pi}{4})^{\frac{1}{m}}} \tag{1.11}$$

$$L^* = 177\sqrt{\frac{Pa}{S^*}} \tag{1.12}$$

$$B^* = \frac{6 * 10^{-5}}{L^*} \tag{1.13}$$

Physical and optical properties of fused silica, fusion-cast CaF_2, sapphire, and spinel at 1.064 μm can be found in in Table 1.1 and these values were used to compute different FOM values for each material [7], [14]–[21]. Note that photo-elastic constants of fused silica and fusion-cast CaF_2 used were the values reported at 1.315 μm while those of sapphire were the ones reported at 633 nm

[8], [18]. Using the properties provided in Table 1.1, different FOM values of each sample were calculated and are shown in Table 1.2. The required thickness was calculated based on a 100-cm diameter disk. It can be seen that both sapphire and spinel require a relatively smaller thickness owning to their higher characteristic strength. For the lensing coefficient, CaF_2 outperforms other candidates due to its negative dn/dT value. No literature data were available on stress-optic

Table 1.1. Physical and Optical Properties of Different Window Candidate Materials

Property	Fused Silica	CaF_2	Sapphire (C-plane)	Spinel
Young's Modulus (GPa)	72.4[a]	110[a]	344[b]	271[b]
Poisson's Ratio	0.16[a]	0.28[a]	0.27[b]	0.26[b]
Bulk Modulus (GPa)	35.5[a]	83[a]	249[c]	200[h]
Shear Modulus (GPa)	31.2[a]	43[a]	135[c]	104[i]
Characteristic Strength (MPa)	~50[a]	~80[a]	946[d]	396[g]
Shape Parameter	4.5[a]	3.5[a]	3.4[d]	7.3[g]
Heat Capacity (per unit volume) ($Jcm^{-3}K^{-1}$, room temperature)	1.66[a]	2.58[a]	3.10[b]	2.93[b]
Thermal Expansion ($10^{-6}K^{-1}$, room temperature)	0.52[a]	21.3[a]	7.15[b]	6.97 [b]
Thermal Conductivity ($Wcm^{-1}K^{-1}$)	0.013[a]	0.08[a]	0.46[b]	0.25[b]
Refractive Index	1.4504[b]	1.4289[b]	1.756[b]	1.701[b]
Thermo-optic Coefficient (10^{-6} K^{-1})	10[b]	-8.1[b]	12.6[b]	9[b]
Absorption Coefficient (cm^{-1})	$3*10^{-7}$ [b]	$5*10^{-5}$ [b]	$5*10^{-5}$ [e]	0.003[b]
Piezo-optic constant (q_{11}) $(TPa)^{-1}$	0.58[a]	-0.4[a]	-0.52[f]	N/A
Piezo-optic constant (q_{12}) $(TPa)^{-1}$	2.8[a]	1.09[a]	0.08[f]	N/A
Piezo-optic constant (q_{44}) $(TPa)^{-1}$	N/A	0.72[a]	-0.71[f]	N/A

** [a]Ref [8]; [b]Ref[14];[c]Ref[16];[d]Ref[17];[e]Ref[7]; [f]Ref[18];[g]Ref[19];[h]Ref[20];[i]Ref[21] constant of spinel so the lensing coefficient was estimated solely based on its dn/dT value as it has the dominant contribution to the distortion coefficient. For the allowable peak fluence values, one must compare them with an actual operating value. Consider a HEL operating at a peak power level of 1 MW at 1 μm with a beam diameter of 30 cm for 5 minutes, the converted peak fluence is approximately 0.42 MJ/cm^2. Looking at the allowable peak fluence associated with the amount of optical distortion for each window material shown in Table 1.2, with all physical and optical properties considered, only fused silica satisfies the required performance. The $J_{All}^{O,D}$ value of sapphire is lower than the required fluence by a factor of 10. Since $J_{All}^{O,D}$ is inversely proportional to the absorption coefficient, if the absorption loss can be reduced to a level of ppm or less, then sapphire would be able to sustain the large power load with a minimal optical distortion. Similar statements can be made for spinel.; If its absorption coefficient level were to reach 10^{-6} cm^{-1}, then it could be a window candidate for the next generation of HEL. Similarly, the calculated $J_{All}^{P,S}$ for all materials suggest that both fused silica (with low optical absorption and thermal expansion coefficients) and sapphire (with a relatively low optical absorption and high characteristic strength) can tolerate the associated planar stress of the higher energy beam. In the case of spinel, the high absorption value still undermines its ability to sustain exposure to high beam fluences. However, with improvements, both sapphire and spinel could serve as window materials for the next generation of HEL systems, since they show high characteristic strength and relatively low thermal expansion. To do so, their absorption losses should be lowered to the level of 10^{-7} cm^{-1} or below.

Table 1.2. Calculated Figure-of-Merits of Different Window Candidate Materials

	Fused Silica	CaF_2	C-plane Sapphire	Spinel
Required Thickness L (cm)	8.07	9.63	2.95	1.38
Distortion Coefficient χ_+ (10^{-6} K^{-1})	10.4	5.23	17.4	~15

Distortion Coefficient χ_{-} (10^{-6} K^{-1})	-0.0255	-0.137	-2.91	N/A
Lensing Coefficient χ (10^{-6} K^{-1})	10.4	5.23	17.6	~15
$J_{\mathrm{All}}^{\mathrm{O.D}}$(MJ/cm^2)	5.59	0.029	0.034	~0.0013
$J_{\mathrm{All}}^{\mathrm{P.S}}$(MJ/cm^2)	58	0.11	1.2	0.052

Moreover, Thomas et al. have developed a set of equations describing the net ray deviation $\Delta\theta_{ne}$ as a function of the radial distance and time is related to the thermo-optic coefficient and the temperature rise, $\Delta T(r,t)$, by [14]

$$\Delta\theta_{ne}(r,t) = -L\left\{\frac{1}{\mathrm{n}(r)}\frac{\mathrm{dn}}{\mathrm{dt}} + \alpha\left(\frac{\mathrm{n(r)}}{\mathrm{n_{air}}} - 1\right)\right\}\frac{\mathrm{d}\Delta T(r,t)}{\mathrm{d}r} \tag{1.14}$$

Note that the temperature rise is directly proportional to the optical absorption coefficient, $\upbeta_{\mathrm{a}}$, through

$$\Delta T(r) = \frac{\upbeta_{\mathrm{a}}\mathrm{M}}{\mathrm{kw_0}\uppi^{1.5}}\int_{r}^{r_0}\frac{1}{r'}\left(\int_{0}^{r'} r''\exp\left(-\frac{r''^2}{\mathrm{w_0}^2}\right)\mathrm{d}r''\right)\mathrm{d}r' \tag{1.15}$$

where M and w_0 are the laser irradiance and beam waist respectively. Using the materials properties given in Table 1.1, assuming a 1 MW Gaussian beam with a 10 cm diameter passing through a laser window with a 5 mm thickness and a 35 cm diameter, the net ray deviations as a function of radial distance for sapphire, spinel, CaF_2, and fused silica are shown in Fig. 1.4. According to Fig. 1.4, the net ray deviation shows a large difference among different materials. Fused silica has the lowest deviation due to its extremely low absorption coefficient and small thermal expansion coefficient. CaF_2 also has a relatively low deviation since it has a negative dn/dT value that counter balances the deviation due to thermal expansion. Sapphire and spinel both have a high net ray deviation due to their higher absorption losses. Again, if the absorption is lowered, then a much smaller ray deviation could be achieved.

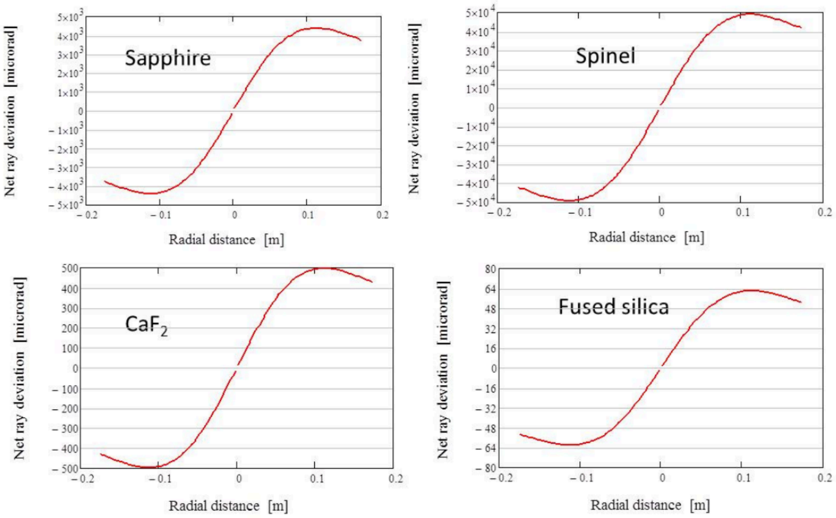

Figure 1.4. Net ray deviation at 1.064 μm wavelength for different laser window materials candidates with a power level of 1 MW [6].

In the next sections, basic principles of light-material interactions will be introduced to provide a deeper understanding of different optical phenomena such as transmission, reflection, absorption, and scattering, etc. It is important to know that the electromagnetic wave propagation is different in sapphire and spinel since the two materials have different crystal structures.

1.2 Electromagnetic Wave Propagation in the Dielectric Medium

1.2.1 Plane Wave Solutions in Isotopic and Anisotropic Media

In this study, polycrystalline spinel is an isotropic material due to its cubic crystal structure while single crystal sapphire is an anisotropic, uniaxial material with a trigonal crystal structure. Plane wave solutions to the Maxwell's equations for electromagnetic wave propagation in an isotropic dielectric media are given by solutions to the following equations:

$$\nabla^2\mathbf{E} - \frac{\mathrm{n}}{\mathrm{c}^2}\frac{\partial^2\mathbf{E}}{\partial \mathrm{t}^2} = 0 \tag{1.16}$$

$$\nabla^2\mathbf{B} - \frac{n}{c^2}\frac{\partial^2\mathbf{B}}{\partial t^2} = 0 \tag{1.17}$$

where **E** and **B** are the electric field and magnetic field vectors, respectively [11]. The speed of light that travels through the medium could be further expressed as

$$c = \frac{c_0}{\sqrt{\mu_m \varepsilon_m}} \tag{1.18}$$

where c_0 is the speed of light traveling through vacuum, μ_m and ε_m are the magnetic permittivity and the dielectric permittivity of the medium, respectively. The ratio of c_0/c is known as the refractive index, n, which is a unitless quantity that represents the relative speed of light in a medium. The refractive index has both real and imaginary parts; the real part in typical materials is always positive and greater than 1 while the imaginary part is associated with the optical absorbance or gain in the medium.

The electric field plane wave solution for an electromagnetic wave traveling through an isotropic medium can be expressed as

$$\mathbf{E} = E_0 e^{-i(\mathbf{k}\cdot\mathbf{r}-\omega t)} \tag{1.19}$$

where E_0 is a constant, **k** is the wave vector, **r** represents the radial distance vector, ω is the angular frequency, and t represents the time. In this study, polycrystalline spinel is considered as an isotropic material due to its cubic crystal structure.

Anisotropic media display birefringence that can be associated with different indices of refraction for propagation along principal axes that depend on polarization direction. For a uniaxial material, two of these indices are equal while the third differs: $n_x = n_y \neq n_z$. For this case, the z-axis is known as the principal optic axis. A laser beam traveling through a uniaxial material can be decomposed into two orthogonal, linearly polarized states that relate to ordinary and extraordinary waves. In anisotropic, uniaxial materials, the dielectric constant is a second-rank tensor with different values that depend on the direction. The full expression of the displacement, **D**, due to electric induction field vector, **E**, is then written as

$$\begin{bmatrix} D_x(\mathbf{r}) \\ D_y(\mathbf{r}) \\ D_z(\mathbf{r}) \end{bmatrix} = \begin{bmatrix} \varepsilon_o & 0 & 0 \\ 0 & \varepsilon_o & 0 \\ 0 & 0 & \varepsilon_e \end{bmatrix} \begin{bmatrix} E_x(\mathbf{r}) \\ E_y(\mathbf{r}) \\ E_z(\mathbf{r}) \end{bmatrix} \tag{1.20}$$

where ε_o represents the dielectric constant along the ordinary axis and ε_e is the dielectric permittivity along the extraordinary axis. An electromagnetic wave (with **E** field that has both *y* and *z* components) traveling through a uniaxial medium in the x direction can be expressed as follows:

$$\mathbf{E}(\mathbf{r}) = \hat{z}E_z e^{-i(\mathbf{k}_e x - \omega t)} + \hat{y}E_y e^{-i(\mathbf{k}_o x - \omega t)} \tag{1.21}$$

1.2.2 Optical Birefringence in Sapphire

Birefringence in a medium causes the light entering to split into two distinct, polarized rays that refract along different paths. For a sapphire window being used in the HEL applications, birefringence must be minimized. In anisotropic, uniaxial materials, the ordinary wave has a refractive index of n_o which does not change with the propagation direction while the extraordinary wave has an index of refraction of n_e that depends on the propagation direction. The ordinary wave has the polarization perpendicular to the z- axis and the extraordinary wave is polarized parallel to the z-axis. In sapphire, the principal optic axis is the crystallographic c-axis shown in Fig. 1.5 [22] . Any ray traveling along the c-axis has a refractive index of n_o as it is considered as an ordinary ray with *E* field perpendicular to the c-axis. To minimize the birefringence effect, c-plane sapphire is typically chosen for windows and is oriented such that the window face is the crystallographic c plane perpendicular to the c-axis. The normally-incident ray traveling along the c-axis direction and perpendicular to the window face propagates as a normal ray, n_o component.

Sometimes, the two surfaces of a sapphire window might not be perfectly parallel due to imprecise preparation causing the ray to travel at a small angle with respect to the c-axis. Although the angle is typically very small, it is still worth noting the refractive index associated with it. In this case, a principal plane containing both the incoming ray and the c-axis must be defined. According to Fig.1.6 [22], the ordinary ray has oscillating *E*-field perpendicular to the plane while the extraordinary ray has the *E*-field parallel to the plane. Note that any ray traveling along the c-axis of sapphire is an ordinary ray. The extraordinary ray that travels at an angle ϕ with respect to the c-axis has a refractive index of $n_e(\phi)$ given as

$$n_e(\phi) = \frac{n_o n_e}{\sqrt{n_e^2 \cos^2\phi + n_o^2 \sin^2\phi}} \tag{1.22}$$

with the value $n_e(\phi)$ goes to n_o when ϕ approaches zero degrees and to n_e when $\phi=\frac{\pi}{2}$ [22].

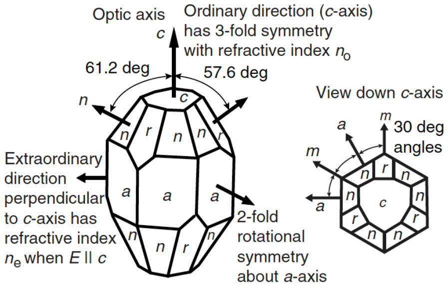

Figure 1.5. Sapphire crystal with 2-fold and 3-fold symmetry directions with c-axis is normal to the c-plane [22].

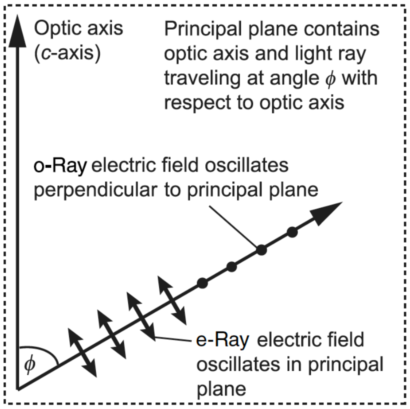

Figure 1.6. Illustration of electric filed oscillation direction with respect to each ray type [22].

1.2.3 Laws of Refraction and Reflection

When a laser beam travels at the interface between air and a window material with different indices of refraction, a portion of the light is reflected while the rest transmits through the medium at a refracted angle assuming no other optical losses [11]. For the case of refraction in an isotropic medium such as polycrystalline spinel, Snell's law describes the relationship between the angle of incidence, θ_1, and the angle of refraction, $\theta_{2,}$ through $n_1\sin\theta_1 = n_2\sin\theta_2$, with n_1 represents the index of refraction of medium 1 and n_2 is that of medium 2. Generally, n_1 is less than n_2 when light travels through the air or vacuum into a denser medium with a reduced speed. The refracted ray bends toward the surface normal. If the light ray travels from a denser medium into the air or vacuum, the refracted ray bends away from the surface normal and the maximum angle of refraction is 90°. A critical angle of incidence can be found when the refraction angle becomes 90°. Any ray travels with an angle of incidence that is larger than the critical angle will become fully reflected without any refraction, a phenomenon known as total internal reflection. The refraction phenomenon is somewhat more complicated in an anisotropic medium such as sapphire where birefringence could divide the refracted ray into both ordinary and extraordinary components. In this study, only normal and near-normal angles of incidence are considered for c-plane sapphire so the birefringence effect is minimized.

The portion of the light being reflected from the interface of two media depends on both angle of incidence and polarization state, which is usually described using the Fresnel reflection coefficients. The angle of reflected ray is always equal to the incident angle (both angles are with respect to the surface normal). The *E*-field orientation of a light beam can be expressed in terms of s- and p-polarizations. The p-polarization represents the *E*-field that is in the plane of incidence while the s-polarization denotes the *E*-field that is perpendicular to the plane of incidence. For HEL applications, the laser beam might be polarized depending on the final purpose and different light polarization states result in different Fresnel reflection coefficients that represent the total light reflectance. For the isotropic medium, the single-surface Fresnel reflection coefficient for both s- and p-polarized light, R_s and R_p, can be expressed as follows:

$$R_s = \frac{(a - \cos\theta_i)^2 + b^2}{(a + \cos\theta_i)^2 + b^2} \tag{1.23}$$

and

$$R_p = R_s\left[\frac{(a - \sin\theta_i\tan\theta_i)^2 + b^2}{(a + \sin\theta_i\tan\theta_i)^2 + b^2}\right] \tag{1.24}$$

where

$$a^2 = \frac{1}{2}\left\{[(n^2 - k_a^2 - \sin^2\theta_i)^2 + 4n^2k_a^2]^{\frac{1}{2}} + (n^2 - k_a^2 - \sin^2\theta_i)\right\} \tag{1.25}$$

and

$$b^2 = \frac{1}{2}\left\{[(n^2 - k_a^2 - \sin^2\theta_i)^2 + 4n^2k_a^2]^{\frac{1}{2}} - (n^2 - k_a^2 - \sin^2\theta_i)\right\} \tag{1.26}$$

where θ_i is the angle of incidence, n and k_a are the real and complex parts of the refractive index, respectively [11]. For unpolarized light with only the real part of the index of refraction, the single-surface Fresnel reflection coefficient can be simplified [11]:

$$R_{unpol} = \frac{1}{2}\left[\left\{\left|\frac{n^2\cos\theta_i - \sqrt{n^2 - \sin^2\theta_i}}{n^2\cos\theta_i + \sqrt{n^2 - \sin^2\theta_i}}\right|\right\}^2 + \left\{\left|\frac{\cos\theta_i - \sqrt{n^2 - \sin^2\theta_i}}{\cos\theta_i + \sqrt{n^2 - \sin^2\theta_i}}\right|\right\}^2\right] \tag{1.27}$$

On the other hand, the general Fresnel reflection coefficient solution for an anisotropic, uniaxial medium is quite complicated. However, special cases have been previously investigated and for the case of sapphire in this work where the crystallographic c-axis is the principal axis, for an unpolarized light beam propagating through a plane-parallel sapphire window at a near-normal angle of incidence, the single-surface Fresnel reflection coefficient can be approximated as [11]

$$R_o = \left(\frac{1 - n_o}{1 + n_o}\right)^2 \tag{1.28}$$

A closer inspection of Eq. (1.28) shows R_o is equivalent to R_{unpol} from Eq. (1.27) under a zero-degree angle of incidence condition.

1.2.4 Total Power Law

When a laser beam propagates through a window, it is either transmitted and or reflected according to the Fresnel coefficients assuming negligible absorption and scattering losses [11]. In the case of scattering, power is not being lost to some other form of energy but it is being lost from the transmitted/reflected beams. Also, scattering is often considered as diffuse transmittance and reflectance. Therefore, as many window materials exhibit both absorption and scattering, the total power of the traveling laser beam must satisfy the following total power law:

$$\tau_s(\theta_i, \omega) + \rho_s(\theta_i, \omega) + \alpha_{abs}(\theta_i, \omega) + \alpha_{sca}(\theta_i, \omega) = 1 \tag{1.29}$$

where τ_s is the specular transmittance, ρ_s is the specular reflectance, α_{abs} represents the total absorbance, α_{sca} denotes the total scatterance, θ_i is the angle of incidence, and ω denotes the angular frequency. The subscript s represents the specular term in the case for the nearly parallel surfaces where the reflected angle is equivalent to the negative of the incident angle and the transmitted angle approximately equals the angle of incidence. Scattering loss would be counted as the diffuse reflectance in both forward and backward directions making $\tau_s(\theta_i, \omega)$ and $\rho_s(\theta_i, \omega)$ become less than the theoretical values when considering surface roughness and other types of bulk and sub-surface defects under the practical situation. Furthermore, both $\tau_s(\theta_i, \omega)$ and $\rho_s(\theta_i, \omega)$ are a function of the complex index of refraction and for a spectrally-averaged polarized light incident on a parallel slab with a thickness, d, both terms can be expressed as follows when the effects of interference, fluorescence, and diffraction are ignored [11]:

$$\tau_s(\theta_i, \omega) = \frac{[1 - R(\theta_i, \omega)]^2 \exp\left(-\frac{\beta_{abs}(\omega) d}{\cos\theta_a}\right)}{1 - R^2(\theta_i, \omega)\exp\left(-\frac{2\beta_{abs}(\omega) d}{\cos\theta_a}\right)} \tag{1.30}$$

$$\rho_s(\theta_i, \omega) = \frac{R(\theta_i, \omega) + R(\theta_i, \omega)[1 - 2R(\theta_i, \omega)]\exp\left(-\frac{2\beta_{abs}(\omega) d}{\cos\theta_a}\right)}{1 - R^2(\theta_i, \omega)\exp\left(-\frac{2\beta_{abs}(\omega) d}{\cos\theta_a}\right)} \tag{1.31}$$

where R represents the single-surface Fresnel reflection coefficient, β_{abs} is the optical absorption coefficient, and θ_a is the refracted angle within the medium. For HEL window materials studied in this work, the value of β_{abs} is typically <<1 so the lossless specular transmittance could be further simplified as [11]

$$\tau_{s-lossless}(\theta_i, \omega) = \frac{[1 - R(\theta_i, \omega)]^2}{1 - R^2(\theta_i, \omega)} = \frac{1 - R(\theta_i, \omega)}{1 + R(\theta_i, \omega)} \tag{1.32}$$

1.2.5 Index of Refraction and the Absorption Coefficient

In Section 1.2.1, it has been mentioned that the refractive index, n, is equivalent to $\sqrt{\mu\varepsilon}$ according to the plane wave solutions to the Maxwell equations. For non-magnetic materials studied in this work, μ=1 and n is now directly equal to the square root of the relative permittivity (dielectric constant). Since ε has a wavelength dependence, n also depends on the light wavelength. When an

EM wave propagates through a lossy medium, it experiences attenuation due to loss of energy resulting from different mechanisms such as absorption and phonon generation, etc. In this situation, the refractive index is a complex function of the light frequency and can be expressed as in the following:

$$\mathrm{n}^{*} = \mathrm{n} + \mathrm{iK} = \sqrt{\varepsilon} = \sqrt{\varepsilon' + \mathrm{i}\varepsilon''} \tag{1.33}$$

where n^{*} is the complex refractive index, n is the index of refraction, K is the index of absorption that is related to the EM wave attenuation, and ε' and ε'' are the real and imaginary parts of the relative permittivity, respectively. In the absence of scattering and other loss mechanisms, the light with intensity I_0 travelling through a lossy medium with thickness z might be mainly attenuated due to optical absorption and the reduced light intensity I (z) is related to the absorption coefficient, β_{abs}, by:

$$\mathrm{I}(z) = \mathrm{I}_0 \exp^{-\beta_{\mathrm{abs}} z} \tag{1.34}$$

To relate β_{abs} and K, one can take a plane wave traveling along a certain direction as shown in Eq. (1.34) and k, the wave vector, is related to n^{*} by k= $\mathrm{n}^{*}\omega/c=(\mathrm{n} + \mathrm{iK})(\omega/c)$. Note that in free space, k=k_0= ω/c=2π/λ with λ being the free space wavelength. Since I is directly proportional to $|\mathrm{E}|^2$ and using the relationship between k and n^{*}, one can find that $\mathrm{I} \propto \exp\,[-2(\omega/c)\mathrm{K}\vec{\mathrm{r}}]$, suggesting I decays exponentially with the propagation distance. Using Eq. (1.34), β_{abs} is related to K by

$$\beta_{\mathrm{abs}} = 2(\omega/\mathrm{c})\mathrm{K} \tag{1.35}$$

The wavelength dependent refractive index can be determined by the Sellmeier equation for many materials [11], [23]. The Sellmeier equation provides an empirical relationship between the light wavelength and the refractive index of a material using a series of single dipole oscillator terms that can be expressed as follows:

$$n^2 = 1 + \frac{A_1\lambda^2}{\lambda^2 - \lambda_1^2} + \frac{A_2\lambda^2}{\lambda^2 - \lambda_2^2} + \frac{A_3\lambda^2}{\lambda^2 - \lambda_3^2} \tag{1.36}$$

where A_1, A_2, A_3, λ_1, λ_2, and λ_3 are called Sellmeier coefficients that are determined by fitting the model to experimental data. For ordinary-ray sapphire and polycrystalline spinel, the values of the Sellmeier coefficients are provided in Table 1.1 [23], [24].

Table 1.3 Sellmeier Coefficients for o-Ray Sapphire and Spinel

	A_1	A_2	A_3	λ_1	λ_2	λ_3
O-ray Sapphire	1.4313493	0.65054713	5.3414021	0.0726631	0.1193242	18.028251
Polycrystalline Spinel	1.8938	3.0755	N/A?	0.09942	15.826	N/A?

1.2.6 Optical Scattering

When an EM field interacts with the charged particles associated with atoms or molecules in a solid, dipole moments can be induced in the material in addition to the permanent ones that might already exist in the system. When dipoles are created or stretched by an EM field, they absorb energy from the excitation field and the absorbed energy takes the form of a secondary field as the accelerated charges produce EM radiation [25]. However, these fields do not necessarily propagate in the same direction or with the same phase as the excitation field due to the difference in permittivity of the particle and medium, leading to scattering phenomena [25]. A reflected or transmitted beam of light can be viewed as a combination of a large number of scattering events that are similar in direction, phase, and frequency. This study mainly investigates the elastic scattering which is a type of particle scattering where the propagation path direction is changed while the energy is conserved. There are two domains of elastic scattering falling into the scope of this work: Rayleigh scattering and Mie scattering. Rayleigh scattering mainly involves the scattering by a spherical particle with a diameter that is much less than the wavelength of the light (about 1/10th of the incident light wavelength). The probability that the sphere scatters the light at an angle θ is proportional to the differential scattering cross section, $\frac{d\sigma(\theta)}{d\Omega}$, which denotes the ratio of power scattered into the solid angle between θ and $d\theta$ to the incident power per unit area. The total Rayleigh scattering cross section is given by

$$\sigma_r(\lambda, \theta, r) = \frac{8}{3}\pi\left(\frac{2\pi n_0}{\lambda}\right)^4 r^6 \left[\frac{(\varepsilon - \varepsilon_0)}{(\varepsilon + 2\varepsilon_0)}\right]^2 (1 + \cos^2\theta) \tag{1.37}$$

where r is the particle radius, n_0 and ε_0 are the relative permittivity and the refractive index of the surrounding medium, and n and ε are the ones of the particle, respectively [26]. For spherical particles with sizes that are comparable to or larger than the incident wavelength, Mie scattering can be used to describe the scattering phenomenon and the total scattering cross section is represented as

$$\sigma_m = \frac{\lambda^2}{2\pi {n_0}^2} \sum_{i=1}^{\infty} (2m + 1)(|a_i|^2 + |b_i|^2) \tag{1.38}$$

where coefficients a_i and b_i are expressed in terms of spherical Hankel and spherical Bessel functions of the first kind respectively, and both of them have a dependence on the magnetic permeabilities of the surrounding medium and the sphere; m is an effective index of refraction factor that takes the value of $\frac{n}{n_0}$[26]. Furthermore, another size parameter, x, which takes the value of $\frac{2\pi r n_0}{\lambda}$, is also commonly used to describe the scattering efficiency. The scattering efficiency, Q, which equals $\frac{\sigma}{\pi r^2}$, is approximately the same for both Rayleigh and Mie scattering when $mx \ll 1$ (with λ^{-4} dependence) and when mx becomes larger than 1, the Mie scattering efficiency departs from the λ^{-4} dependence and reaches a limiting value of 2 [11] [26].

In the next few sections, common growth methods of sapphire and spinel will be introduced briefly because growth conditions and parameters are crucial to the physical and optical properties of the resulting materials. Furthermore, typical defects found in both materials will be examined since they are responsible for the low-level optical losses in sapphire and spinel.

1.3 Growth Methods and Structural Defects

1.3.1 Materials Growth Methods

Both synthetic sapphire and spinel are mainly commercially grown from raw powders under different methods that typically require high temperatures (above 1500 °C). Therefore, the powder purity, crucible and chamber contaminant, heating/cooling rate, as well as post-growth thermal and mechanical treatments are critical to both physical and optical properties of these materials [4], [16], [27], [28]. The most common sapphire growth methods include the Verneuil process, the Czochralski process, the Kyropoulos process, the heat exchange method (HEM), and the edge-defined film-fed method (EFG) [16], [29]. Among these methods, the Verneuil process is the oldest method, and it is still used to produce sapphire seed crystals for other growth methods. This process involves spraying alumina powder into an oxygen-hydrogen flame and the main drawback of this method is that a relatively high residual stress remains in the sapphire that is produced and it cannot be used to produce large crystals [27]. The Czochralski process (CZ) is a common growth method for semiconductors which involves growing materials from melt in a crucible. In this method, the seed crystal is attached to a cooling rod and the rod rotates at a controlled rate. Single crystal sapphire grows at the interface between the seed and the melt while the seed is being pulled as shown in Fig. 1.7 [27]. However, this method creates challenges for growing c-axis sapphire

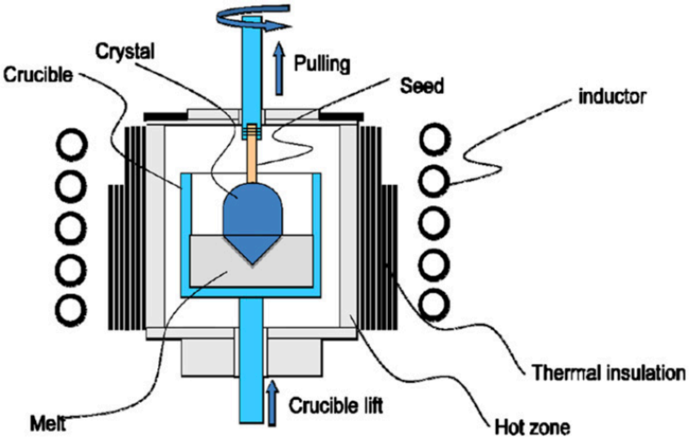

Figure 1.7. An illustration of the Czochralski sapphire growth process [27].

as well as larger diameter crystals. The Kyropoulos process also employs dipping a seed crystal into a crucible with a melt. However, this method produces crystals with a sharp, convex shape for the crystallization front under conditions in the hot zone shown in Fig. 1.8. Furthermore, the seed is only rotated during the early stage of growth process to allow a slow decrease of the hot zone's temperature without subsequent rotation. The resulting crystal only touches the crucible on the lower portion of the crucible as well as the bottom. This technique allows the production of large sapphire crystals with a lower temperature gradient and a lower level of residual stress [27]. The

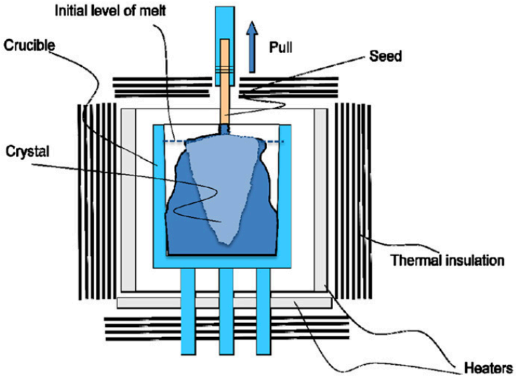

Figure 1.8. An illustration of the Kyropoulus sapphire growth process [27].

HEM method, shown in Fig. 1.9, allows a vertical directional crystallization under a low temperature gradient at the bottom of the crucible. The seed sits at the bottom of the crucible and it is constantly cooled using a helium gas flow. While it allows the growth of large sapphire crystals, the process is difficult to control automatically because different growth parameters require precise monitoring and control [27]. Lastly, the EFG process uses a die (also acts as a shape controller) that is made of a material (e.g., molybdenum in the case for sapphire) wetted by the melt with one or more capillaries immersed in the melt. The growth process starts when the capillary force raises the melt above the upper surface die to contact the seed crystal. A thin film of melt separating the die and the growing crystal is also formed as is shown in Fig. 1.10. The temperature of the thin film melt must be precisely controlled to avoid the attachment of the grown crystal to the die. The main advantage of the EFG method is that it allows for the production of small crystals with near net shape for applications with size constraints. However, EFG-grown sapphire has been reported to contain more bubbles compared with those produced from other techniques [27].

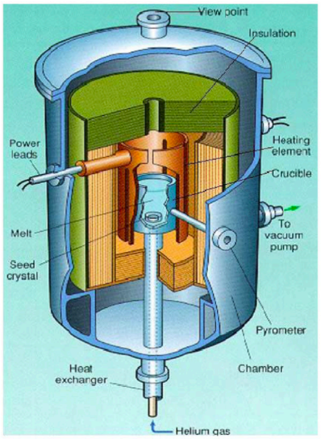

Figure 1.9. An illustration of the HEM sapphire growth process [27].

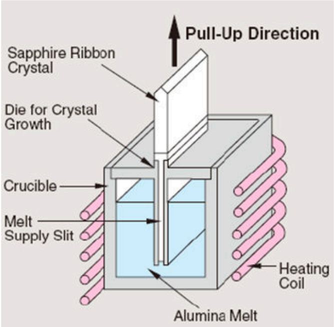

Figure 1.10. An illustration of the EFG sapphire growth process [27].

Polycrystalline spinel is typically synthesized using a sintering process in which powders are compacted and heated (often under pressure) without melting the starting materials. It is the most popular technique to manufacture the transparent spinel in bulk due to the lower manufacturing cost and the ability to scale up production. There are two driving forces that cause sintering to occur. One of them is to minimize the solid/gas interfacial energy by closing the pores in between each particle and this mechanism is named densification. Another driving force is coarsening which involves the growth of particle size to minimize the individual particle curvature. However, the later mechanism does not stimulate pore elimination and the two mechanisms are always competing with each other during sintering. Furthermore, coarsening tends to dominate at lower temperatures while densification occurs more readily at higher temperatures [30]. Ideally, a perfect sintering event requires both mechanisms to occur with densification being the main process. Nevertheless, there are many factors that influence the sintering event such as particle diffusion and volume change in the bulk, which can vary for different materials. Overall, it is a complicated process that is currently not well understood.

There are three conventional sintering techniques but all of them have disadvantages that can impair the properties of the sintered spinel. The pressureless sintering process requires the sample to stay in the oven for 12 hours or longer and the resulting material has a very large grain size that leads to low fracture toughness [31]. The hot-pressing method also requires longer processing times along with high temperatures and pressures which result in higher energy input. The longer processing time allows secondary phases associated with impurities to grow near the grain boundaries. Both methods involve the use of sintering aids such as lithium fluoride to accelerate and smooth the sintering process. These aids often remain in the final product as an impurity and often degrade the spinel properties. Additionally, both methods demand a further hot isostatic pressing (HIP) process to achieve full density [32]. Spark plasma sintering is another technique that has a faster processing times and lower processing temperatures due to the assistance of high pressure [33]. However, all three techniques suffer from nonuniform heating of the sample which can produce nonuniform grain sizes as well as cracks in regions where too much heating occurs. In recent years, there has been an interest in using microwave heating to synthesize spinel since this technique has several advantages over other techniques including the ability to produce volumetric heating with rapid heating rates. However, to grow large windows, microwave beam control becomes crucial as any inhomogeneities in the beam profile can result in undesirable hot spots which then cause cracking during the synthesis process.

1.3.2 Point Defects

Point defects such as vacancies and impurities can greatly affect structural and optical properties in metal-based oxide materials. Impurities typically originate from the raw powder (the starting material) for both sapphire and spinel as well as from the crucibles used to grow these materials [16], [34]. In sapphire, isovalent impurities such as Cr^{3+}, Ti^{3+}, Co^{3+}, Ni^{3+}, Fe^{3+}, Mn^{3+}, V^{3+} etc. can trap electrons or holes thus causing optical absorption loss. Furthermore, heterovalent impurities such as Cr^{4+}, Ti^{4+}, Si^{4+}, Mg^{2+} etc. are also trapping centers that cause formation of cationic vacancies to compensate their charges during the sapphire growth process [16]. Similarly, in spinel, Cr^{3+}, Fe^{3+}, Mn^{2+}, V^{3+}, Co^{3+}, and Cu^{2+} have been reported to cause various absorption bands in the optical spectrum [16]. The concentration of different impurity elements can be reduced if the starting materials are further purified.

Both sapphire and spinel are compounds that are vulnerable to vacancy-type defects. Both cationic and anionic vacancies in various charge states, vacancy-impurity complexes and vacancy aggregates are commonly found in these materials [35]–[42]. Furthermore, interstitial ions and substitutional ions in cationic and anionic sites are also possible. In sapphire, vacancy pairs such as Schottky defects (two aluminum vacancies plus three oxygen vacancies) and Frenkel defects (one intestinal ion plus one vacancy of the same charge) form in the bulk of the crystal and near the surface [16]. Numerous studies have reported formation energies of different types of vacancies in both sapphire and spinel and most of these energies are in the range of -10 to 25 eV at different Fermi energy levels [16], [38], [43] (theoretically, a negative formation energy occurs at very low Fermi energy level which does not apply to this work). Under thermodynamic equilibrium, the concentration of point defects should be in the range of 10^{-30} to 10^{-60} cm^{-3} at room temperature which is extremely low [16]. However, in reality, point defect concentrations are not at equilibrium levels in either sapphire or spinel due to a reducing growth environment and subsequent annealing processes [16]. Indeed, in most commercially-available sapphire and spinel materials, F-centers (electron trapping due to oxygen vacancies) and V-centers (hole trapping due to cationic vacancies) are commonly observed in the absorption spectra in the UV and visible regions of these materials [37], [40], [41], [44]–[47]. By performing a subsequent annealing in an oxidizing environment, the oxygen vacancy content can be further lowered in these materials [44], [48].

1.3.3 Dislocations

There are several dislocation formation mechanisms in sapphire. Dislocations can be inherited from the seed crystal during the growth process [16], [49]. If thermal gradients occur in a particular region within the boule, the thermoelastic-stress-induced, plastic deformation can also produce dislocations. Additionally, impurity trapping and vacancy aggregation are mechanisms for dislocation (loop) formation since both cause lattice distortion. The typical density of dislocations in different sapphire samples has been found to be roughly 10^6 cm^{-2} [16]. In spinel, dislocations are mainly produced at the beginning of hot-pressing processes due to a high, effective-stress concentration at the neck region [50]. Furthermore, in the subsequent HIP process where spinel becomes fully densified, the applied stress increases the density of dislocations. Since both sapphire and spinel windows require different grinding and polishing treatments, dislocations can be generated near the sub-surfaces in these materials, which can result in surface absorbance and scattering.

1.3.4 Block Structures and Grain Boundaries

Block or sub-grain boundaries due to a small crystallographic misorientation (less than 10 degrees) have been observed in synthetic single-crystal sapphire materials [16], [29]. These sub-grain boundaries are caused by the lineage structure appearing in the melt crystallization process and their presence could be reduced by decreasing thermal stresses that occur during growth. Additionally, sub-grain boundaries can be formed by dislocation pile-ups during cooling and annealing processes. Mobile dislocations can migrate to low energy positions and form these types of boundaries [16], [29]. Grain boundaries in polycrystalline spinel are known for impurity trapping and nonstoichiometry [51]–[53]. Moreover, these grain boundaries are often decorated by triple junctions and porosity which mainly act as scattering centers that greatly reduce the transmittance of spinel [51], [54]. By controlling the grain size and utilizing chemical agents as cleaners, absorption and scattering losses due to grain boundaries can be reduced.

1.3.5 Bubbles and Porosity

Small bubbles, also known as micro-voids, have been observed in sapphire samples that are grown under different conditions [55]–[57]. The bubble size ranges from a few micrometers to hundreds of micrometers which sometimes can be detected by human eyes under a strong white light. One major cause of the bubble formation is the thermal decomposition of molten alumina near the walls of the crucible and the locking-in of the resulting gas inclusions at the crystallization interface. It has been observed that the bubble formation can be mitigated by reducing the surface roughness of the crucible walls as well as the impurity content in the starting materials [55]. Another cause of bubble formation is the growth atmosphere itself. Sapphire is commonly grown under vacuum or inert atmospheres such as Ar, He, N_2, and H_2, which contain some water and oxygen. If the growth chamber is not sealed tightly or high vacuum is not achieved before the melting of the raw materials, the amount of gas in the melt can result in bubble formation [16], [57]. Furthermore, chemical components such as oxygen and carbon which are in the initial starting materials can later form dissolved gases during sapphire growth, thus resulting in the bubble formation. Numerous works have shown that the crystal pulling rate has a great effect on the bubble formation in sapphire if the growth technique involves either the Czochralski or the Micropulling Down Technique [56].

Incomplete densification during sintering often results in porosity predominately between grains [58], [59] . In spinel, pores can serve as the main scatter centers in addition to grain boundaries and sintering aid residuals. The sizes of pores are also important since those with sizes comparable to the operating wavelength can cause strong scattering. Indeed, 100 ppm of 400-nm diameter pores reduces the theoretical transparency of 1-mm thick spinel to about 50% at a wavelength of 600 nm [59]. Pore sizes comparable to the operating wavelength should be avoided to minimize scattering losses.

1.4 Study Outline

This thesis includes three main chapters that are associated with different aspects of HEL window materials. Chapter 2 focuses on the absorption measurements of different sapphire and spinel samples. Results are presented for UV-Visible spectroscopy and photothermal common-path interferometry and are analyzed to identify absorption bands and trends. An empirical absorption model is applied to fit the absorption data. Additionally, a pyrometry technique (using a long-wave, infrared camera) has been developed to measure sample surface temperatures rise due to absorption. In Chapter 3, surface scattering and surface morphologies are mainly discussed. Specifically, a confocal microscope and a stereo microscope are employed to obtain optical micrographs to study the surface morphologies of selected sapphire and spinel samples. Atomic force microscopy (AFM) images of selected samples are also used to study surface roughness information. Measured scattering losses using the bidirectional scatterance probability distribution function (BSPDF) of sapphire and spinel samples with different polished surface conditions are also presented. A simple, empirical single scatter model is developed and used to fit the scattering data of sapphire. Spherical anomalous diffraction approximation (ADA) models are utilized to fit the diffuse scatterance of spinel. Lastly, Chapter 4 focuses on the characterization of different bulk and surface-related defects that exist in sapphire and spinel samples studied in this work. Positron annihilation lifetime spectroscopy (PALS) is used to detect cationic vacancy-type defect near the sample surface and the results along with the measured surface absorbance are discussed. Trace element impurity concentration of selected samples are obtained using Laser ablation inductively coupled mass spectroscopy (LA-ICO-MS) and the results are discussed with the observed absorption bands in these samples. Raman spectroscopy and secondary ion mass spectroscopy (SIMS) are used to study surface impurities in different samples. Finally, images acquired using transmission electron microscopy (TEM) and secondary electron microscopy (SEM) with a cathodoluminescence (CL) detector are presented to demonstrate different types of sub-surface damage that is produced by grinding and polishing of the optic surface.

Chapter 2. Optical Absorption Measurements

2.1 Introduction

Synthetic sapphire and spinel are promising window materials for high energy laser (HEL) applications due to their high transparency and superior mechanical properties [6], [27], [60]–[62]. Future HEL systems will operate at or near the megawatt level in continuous wave (cw) operation and will require optical materials that are highly transparent at wavelengths near 1 μm . An optical material is generally considered to be "highly transparent" if it has both extremely low absorption and scatter ($< 10^{-5}$ cm^{-1}) [6]. For HEL windows, highly transparent materials are required because absorption and scatter can lead to photothermal heating that results in material deformation and refractive index changes that produce ray deviation. As mentioned in Chapter 1, a figure of merit for thick window materials was developed and it suggested that an ideal HEL window should have both a negative value of the thermo-optic coefficient (dn/dT) and an ultra-low bulk absorption coefficient (about 10^{-5} cm^{-1}) [8]. However, since sapphire and spinel both have positive thermo-optic coefficients, much lower bulk absorption is needed in these materials to effectively achieve the desired performance [8]. The first task that must be completed to improve sapphire and spinel as candidate HEL materials is to measure the absorption and scatter in samples produced using current processing techniques using state-of-the-art methods.

A sensitive absorption measurement technique must be used to measure the ultra-low-level absorption of transparent materials since many of the conventional methods do not have the required sensitivity. Standard methods such as Fourier-transform infrared (FTIR) spectrometry or UV-VIS-NIR spectrometry are designed to measure losses in materials that are not ultra-transparent and generally cannot be used to measure the low losses in materials considered for

HEL applications. Part of the reason for the lack of sensitivity of these techniques is that they are designed to measure transmitted (or reflected) light and losses are inferred from the absence of transmitted (reflected) light. Simple models are used to interpret the measured data to extract the absorption coefficient. In contrast, laser calorimetry, PCI, laser-induced deflection (LID), and photoacoustic absorption spectroscopy, all depend on the heating effect generated by the laser beam when being absorbed by the material [63], [64]. Laser calorimetry uses a thermal detector attached to the side of a sample to measure the temperature rise of the material induced by laser irradiation. In this technique, the detector does not measure the temperature at the location where there is a direct interaction between the laser beam and the sample, and it depends on thermal transport from the interaction region to the edge of the sample to obtain an estimate for the amount of energy that the sample absorbs. Owing to the indirect nature of the measurement, the sensitivity of the current laser calorimetry method is limited and cannot be used to make measurements in low-loss materials [63]. By contrast, both the PCI and LID techniques have been used to make more direct measurements of absorption since they measure changes in the refractive index in the beam interaction zone. Both techniques use pump-probe configurations that rely on changes to the probe beam propagation that are related to the local temperature gradients induced by the pump. Typically, both of these techniques require a high continuous wave (cw) or quasi-cw pump and the measurement time is relatively short [63]. Furthermore, photoacoustic absorption spectroscopy employs pulsed lasers as the pump light sources, but it relies on a calibration factor that is obtained using other techniques such as FTIR, to interpret the absorption results [63]. Another method, whispering gallery resonator-based absorption spectroscopy, calculates the absorption coefficient based on total internal reflectance. The critical disadvantage of this method is that it requires the resonator to be manufactured out of the material of interest [64]. The sensitivity levels for each of these techniques are given in Table 1. In the end, the methods that should be used must have the necessary sensitivity while having the fewest calibration requirements and demands on sample fabrication.

Table 2.1 Measurement Sensitivity Level of Different Absorption Measurement Techniques

Absorption Measurement Techniques	Current Sensitivity Level [64]–[66]
FTIR/UV-VIS	10^{-3}/cm
Laser Calorimetry	10^{-4}/cm
Photoacoustic Spectroscopy	10^{-6}/cm
PCI	10^{-7}/cm
LID	10^{-5}/cm

In this chapter, absorption measurements in a variety of single-crystal sapphire and polycrystalline spinel samples obtained from different vendors are reported. UV-VIS spectroscopy was used to measure the transmittance of sapphire and spinel in the wavelength range 190 to 600 nm to detect impurity absorption bands. Photothermal common-path interferometry (PCI) was used to measure the weak absorption at 1064 nm as well as to confirm the calculated absorption values at 355 and 532 nm. Finally, a pyrometry technique using a long-wave, infrared camera and a high energy laser was developed to demonstrate photothermal heating in spinel. Analytical models of laser heating as well as COMSOL simulation results were used to interpret various results.

2.2 Materials and Method

2.2.1 Materials

Five single-crystal, c-axis sapphire disks with diameters of 25.4 mm, two polycrystalline spinel disks with varying diameters (from 25.4 to 38 mm), and two spinel square samples (15 mm by 15 mm) from different manufacturers were used in this study. The thickness and synthesis methods are summarized in Table 2.2. All samples were polished to an optical grade finish corresponding to the measured surface scratch and dig values given in Table 2.2.

Table 2.2 Sapphire and Spinel Sample Specifications and Synthesis Methods

Sample	Thickness (mm)	Scratch/Dig	Synthesis Method
GTAT 1 (Sapphire)	10.19	<60/40	HEM
GTAT 2 (Sapphire)	10.15	<60/40	HEM
GTAT 3 (Sapphire)	10.15	<60/40	HEM
Guild 1 (Sapphire)	10.03	<40/20	HEM
KO 1(Sapphire)	9.97	<60/40	Kyropoulos
CN Disk 1 (spinel)	2	<60/20	Conventional sintering with subsequent HIP
CN SQ 1 (spinel)	7	<80/50	Conventional sintering with subsequent HIP
CN SQ 2 (spinel)	7	<40/20	Conventional sintering with subsequent HIP
JHUAPL Disk	4	<60/40	Hot Pressed

GTAT stands for GT Advanced Technologies, Guild stands for Guild Optics, KO stands for Knight Optical, HEM stands for heat exchange method, CN stands for Cera Nova

2.2.2 UV-VIS Spectroscopy

Survey scans of the optical transmission from the ultraviolet (190 nm) to the visible (600 nm) were performed using a PerkinElmer Lambda 950 integrating-sphere spectrometer for selected samples. Each measurement was performed using 0° angle of incidence. The instrumental variability, which represents how much the measured transmittance deviates from 100% in a background measurement, was determined as the change in transmittance ($\Delta\tau$). The long-term variability was obtained by taking the ratio from two background runs over the chosen spectral range that occurred ten days apart yielding a $\Delta\tau$ of ±0.3%. The short-term instrumental variability was obtained by running nine consecutive background transmittance measurements and the result indicated an average $\Delta\tau$ of ±0.14% with a standard deviation of ±0.095%.

2.2.3 PCI

A PCI system was used to perform optical absorption measurements. PCI measurements at 355, 532, and 1064 nm were conducted by Stanford Photo-Thermal Solutions (Pahoa, HI) on different sapphire and spinel samples to detect bulk and surface absorption losses. A schematic of the PCI measurement apparatus is shown in Fig. 2.1 where a pump-probe approach is used to assess absorption. For all measurements, the probe used was a HeNe laser which had a spot size of 70 microns while the pump laser beam diameters varied depending on the wavelength of interest. A lock-in amplifier was used to detect the probe beam signal at the modulation frequency. Furthermore, the translational stage in this case allowed both horizontal and vertical sample movements to enable both longitudinal and transverse scans. For example, to obtain a spatially resolved bulk absorption coefficient, longitudinal scans were performed by moving samples along the probe laser beam path (see Fig. 2.1). Changing the intersection point of the focused pump and collimated probe beams inside each sample permitted the absorption coefficient to be mapped through the sample thickness. Once a spot in the bulk was identified using the longitudinal scan, a transverse scan was performed along the center of the sample to assess the homogeneity. Similar procedures were also used for the surface absorbance measurements except that an additional time-dependent scan (where the surface was exposed to the focused pump beam) was performed.

The governing principle behind the PCI measurement is that the refractive index of the sample changes due to photothermal heating by the pump beam at the modulation frequency. The change in refractive index leads to phase variations of the probe beam which are measured using interferometric methods [67]. At quadrature, the change in probe intensity, ΔI , associated with a phase change, $\Delta\phi$, can be expressed as follows:

$$\frac{\Delta I}{I} = \Delta\phi = \frac{2\pi}{\lambda}(\Delta n L + n \Delta L) \tag{2.1}$$

where I is the intensity of the probe beam, λ is the probe laser wavelength, Δn is the index change, L is the physical path length in the sample, n is the index of refraction, and ΔL is the change in the sample thickness produced by thermal expansion[68], [69]. Equation (2.1) indicates that two major contributors to the signal are associated with index and path length changes resulting from heating. While the linearity of this signal at small phase changes permits an absolute measurement to be made, a relative measurement can also be made using a calibration factor developed using a PCI measurement at the wavelength of interest on a material with a known absorption coefficient [69]. The PCI technique has a sensitivity as low as 10^{-6} cm^{-1} being limited by quantum noise (shot noise) in the detector as well as by the pump laser power that is available [69].

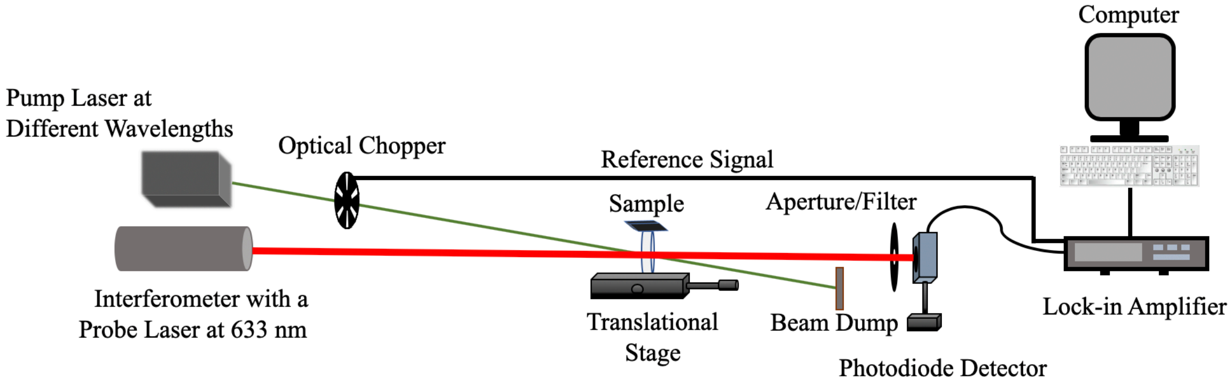

Figure 2.1. Schematic illustration of the PCI apparatus used for measurement of optical absorption. Both probe and pump beams transmit through the sample. Probe beam phase changes are measured interferometrically.

2.2.4 HEL Photothermal Heating

To study the temperature rise in the window material candidates in this study, a photothermal heating experiment using a high power pump laser was conducted at JHUAPL. A schematic of the experimental setup is presented in Fig 2.2. Two 200-W, fiber-coupled semiconductor cw lasers (operating wavelength at 973.2 nm, beam diameter of 1.8 mm) were used with one being used as the sample heating source while the other served as a reference beam. A FLIR A325sc longwave infrared camera with a spectral range of 7.5 to 13 μm was used to detect temperature rises due to photothermal heating. A camera operating in this wavelength range was chosen since it is not sensitive at the pump wavelength and the sample (spinel) has an emissivity that is close to 1 near 10 μm and this simplifies calibration of the measurement. The reference beam travelled through an aperture on the chamber wall without interacting with any optics was absorbed by a ceramic plate in the chamber. The purpose of using a reference beam and a ceramic plate was to compare the two beam shapes to detect any beam distortion of the laser beam that transmitted through the spinel window. The reflected beam spots were recorded using a camcorder that operated at visible wavelengths.

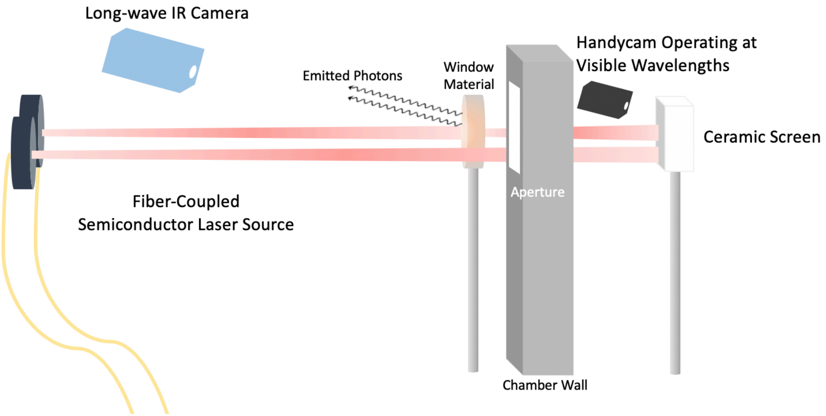

Figure 2.2. An illustration of the HEL photothermal experimental setup. The long-wave IR camera was placed approximately 14 cm apart from the sample. The visible camera was located behind the chamber aperture.

2.3 Results and Discussion

2.3.1 Sapphire

The UV-VIS measurement was performed on GTAT 1-3, Guild 1, and KO 1 to detect the absorption band features in the wavelength region from 190 to 600 nm. The results are shown in Fig. 2.3 where the absorption coefficient is plotted on a logarithmic scale as a function of the wavelength. The measured transmittance data, τ, along with the calculated Fresnel reflectance, R, were used to calculate the extinction coefficient, β_{ext}, for each sample using the following equation:

$$\beta_{\mathrm{ext}} = \frac{\ln(2\mathrm{R}^2\tau) - \ln\left[\sqrt{(1-\mathrm{R})^4 + 4\mathrm{R}^2\tau^2} - (1-\mathrm{R})^2\right]}{\frac{\mathrm{d}}{\cos\theta}} \tag{2.2}$$

where d is the sample thickness and θ is the refracted angle inside the window. To obtain the absorption coefficient, the frequency-dependent scattering contribution can be removed from the extinction using a model for the scattering. The model used for this purpose took the form of $A\nu^4 + B\nu^P$ where A, B, p are coefficients used for fitting purposes and ν denotes the optical frequency. This model accounts for both Rayleigh ($A\nu^4$) and Mie ($B\nu^P$) scattering with the former contributing more in the wavelength region of interest (since $p < 4$). A more detailed derivation for scattering losses will be presented in the scattering measurement section. Since results presented here are meant to highlight absorption band features in each sample, only one set of

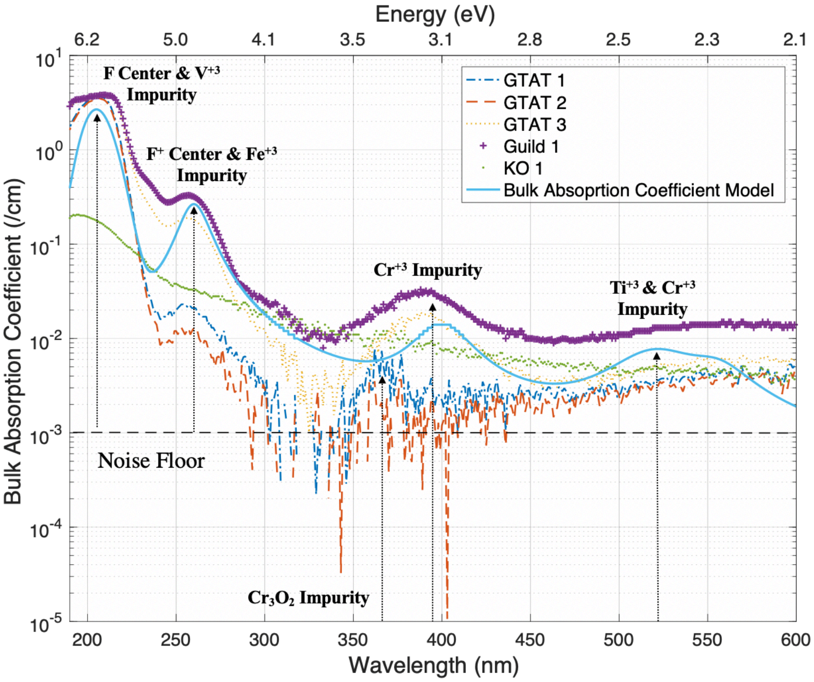

Figure 2.3. Absorption coefficients for GTAT 1-3, KO 1, and Guild 1 as a function of wavelength shown in dark blue, orange, yellow, purple, and green broken lines, respectively. The absorption coefficient model (based on the OPTPROPX code along with possible defect bands) is shown by the light blue solid line.

fitting parameters for the scattering model was used for all samples. These parameters were identified empirically with the following values being used: A=4.5x10^{-21} cm^3, B=10^{-9} $cm^{-0.3}$, and p=1.3.

The absorption coefficients for the GTAT and Guild samples (all were HEM-grown) are enhanced in bands centered at various wavelengths according to Fig. 2.3. Detailed information of each absorption band along with its associated absorption level in each sample are reported in Table 2.3. The band at 206 nm (6.1 eV) has been studied previously and is likely related to the F center (two electrons trapped due to an anionic vacancy); bands at 225 nm (5.5 eV) and 255 nm (4.8 eV) are associated with the F^+ center (one electron trapped due to an anionic vacancy) and a small amount of Fe^{3+} impurity [34], [70], [71]. Beyond F center-related absorption, at 215 nm (5.7 eV), absorption loss due to V^{3+} has been reported and this type of impurity could be contributing to absorption in this wavelength range [34]. Absorption levels due to these centers appear to be one order of magnitude less in KO 1 compared to those of other samples suggesting a lower anionic vacancy concentration. In addition, both GTAT 1 and 2 which were HEM-grown show a lower absorption level due to F^+ center and Fe^{3+} compared to the other samples with the same growth technique suggesting the absorption losses may be controllable during the manufacturing process. The absorption band at 360 nm (3.5 eV) of GTAT 1, GTAT 2 and KO 1 as well as the band at 395 nm (3.1 eV) of GTAT 3 and Guild 1 are associated with chromium oxide and Cr^{3+} [72],[73] . Again, both GTAT 1 and 2 show a relatively lower absorption level associated with chromium impurity compared to all other samples. However, the location of the Cr-related impurity band in these two samples and the KO sample tends to shift toward higher energy (3.5 eV) compared to the other two HEM-grown samples. One possible explanation is that the Cr-related absorption bands at 3.5

eV in GTAT 1, 2 and KO 1 are due to Cr_2O_3 as these have been reported to have a spectral line at that photon energy whereas the bands of GTAT 3 and Guild 1 were more likely caused by Cr^{3+} ions [72],[73] . Furthermore, other works have reported an absorption band at 360 nm (3.44 eV) observed in sapphire and assigned it to be due to either Fe^{3+} impurities or F^+ centers [34], [48]. Additional bands centered at 530 nm (2.33 eV) and 550 nm (2.25 eV) are caused by Ti^{+3} and Cr^{+3}, respectively [34], [70]. However, the appearance of these two adjacent bands is not noticeable in all samples, but a subtle increase in the absorption coefficient in some samples is detected in that region, which could be due to a small amount of these impurities. Generally, the types of impurity elements as well as the absorption at the measured wavelengths of all samples studied in this work were similar to those reported three decades ago indicating that any improvements to the single crystal growth techniques used to produce these materials have generally not improved the optical properties [34], [70].

Table 2.3 Strength of absorption bands caused by different types of impurities and defects at various wavelength regions in GTAT, Guild, and KO samples.

Defect (Region)	Absorption Coefficient (cm^{-1})				
	GTAT 1	GTAT 2	GTAT 3	Guild 1	KO 1
F Center and V^{+3} Impurity (203 nm 6.1 to 5.5 eV)	~1	~1	~1	~1	~0.1
F^+ Center and Fe^{+3} impurity (225 nm, 258 to 275 nm 4.8 to 4.5 eV)	~0.01	~0.01	~0.1	~0.1	~0.01
Cr^{+3} Impurity & Cr_3O_2 (354 to 406 nm 3.5 to 3.05 eV)	~0.001	~0.001	~0.001 to 0.01	~0.01	~0.001 to 0.01
Ti^{+3} and Cr^{+3} Impurities (530 to 550 nm 2.33 to 2.25 eV)	~0.001	~0.001	~0.001	~0.01	~0.001

To further assist in the identification of features in these spectra, a bulk absorption coefficient model (based on the OPTPROPX code) that simulates various impurity and defect-related absorption bands in sapphire was used [76]. Using this model, the two, oxygen-vacancy-dominated, defect bands at 205 and 260 nm, as well as the impurity bands at 400 nm (Cr^{+3}), 520 nm (Ti^{+3}), and 555 nm (Cr^{+3}) could be identified. The modeled result, shown by the solid blue line in Fig. 2.3, was generated using parameters that roughly correspond to those for GTAT 3 and Guild 1 used in this study [62], [76]. Absorption bands were modeled using a classical oscillator strength model given in Eq (2.3):

$$\beta_{\mathrm{abs}}(\upsilon) = \frac{\upsilon^2}{\mathrm{nc}} \sum_i \frac{\upsilon_{0i}^2 \Delta\varepsilon_i \Gamma_i}{(\upsilon_{0i}^2 - \upsilon^2)^2 + (\upsilon\Gamma_i)^2} \tag{2.3}$$

where the summation is over the different electronic transitions, υ is the wavenumber, n is the index of refraction, c is the speed of light, υ_o represents the oscillator location (in wavenumbers), $\Delta\varepsilon$ is related to oscillator strength and is proportional to the number density of each impurity or defect, and Γ is the oscillator width. The oscillator strength is a dimensionless quantity that denotes the absorption probability in all allowed transitions between two energy levels in the medium. All absorption features represented by this model use a modified Lorentzian line shape.

By varying different parameters in Eq. (2.3), the model could be adjusted to fit different absorption features observed in different samples. While various impurities and defects are associated with increased absorption in specific wavelength regions, the model has a background, functional form that is expressed by the following:

$$\beta_{abs}(\nu) = \beta_0 \exp\left(\frac{\nu}{\nu_0}\right) \tag{2.4}$$

where β_0 and υ_0 are fitting parameters and ν is the frequency. The validity of this model has been established empirically using measured absorption coefficient values from numerous works [6], [77].

Overall, the model accurately represents different absorption bands as well as overall absorption trends in the wavelength region of 190 nm to 600 nm. However, at longer wavelengths (from 600 to 1000 nm), the calculated absorption values based on the UV-VIS measurements deviate from the model. The model suggests that the absorption coefficients should continually decrease (from 10^{-3} to 10^{-4} cm^{-1}) going from 600 nm toward longer wavelengths. However, the calculated values of all samples stay at the 10^{-3} cm^{-1} level in this wavelength region. A UV-VIS instrumental artifact which is associated with a detector change occurred near 800 nm which resulted in unavoidable background noise in the measured data in the wavelength region between 600 nm to 800 nm. As the wavelength further shifted to the near-infrared region, an accurate absorption coefficient became even harder to obtain as the predicted values approached 10^{-4} to 10^{-5} /cm.

One possible reason for this difficulty could be that the instrumental variability of ±0.3% leads to a ±0.35% difference in the total extinction loss at 1064 nm in sapphire having a thickness of 1 cm [78]. While this error might be small compared to the absorption loss at shorter wavelengths, it becomes significant in the near-infrared region as the absorption value decreases to the same order of magnitude. Another possible explanation for the disagreement can be that the calculations did not account for surface absorbance and scatterance of sapphire. There has been no detailed investigation of models for the surface-related losses that could be used in the calculations, but the surface absorbances of sapphire at 355, 532, and 1064 nm have been found to be negligible (shown later in the chapter) compared to the bulk loss at those wavelengths. On the other hand, the surface scatterance at each measured wavelength (shown later in the scattering results section) is comparable or even higher than the bulk absorbance. Focusing on the 1 μm wavelength region, the surface scatterance values could be one or two orders of magnitude higher than the bulk absorbance values for sapphire so the calculations might not accurately differentiate between the two losses. These results indicate that a direct, sensitive absorption measurement technique is required to record low-level absorption losses at longer wavelengths.

Sapphire is a mainly ionic compound containing different point defects including vacancies and interstitial ions. Both the HEM and the Kyropoulos methods require growth from a seed crystal placed in a crucible with an Al_2O_3 melt under high temperature (above 2000 °C) in either a reducing or a vacuum environment. During the growth process, impurities and dislocations can add to the overall defect content of the single crystal [16], [27], [79]. In particular, both types of F centers that impact the spectra shown in Fig. 2.3 can be caused by oxygen deficiency [16], [71] especially when growth occurs under reducing conditions. When argon, hydrogen, and carbon are present, the tendency for formation of anionic defects increases markedly [16]. Previously, for a specific defect in an insulator, Smakula derived a relationship between the defects per unit volume, ρ_D, and the optical absorption coefficient caused by such defect, β_{abs}, through the oscillator strength, f_D, and the damping constant, γ, which is given by the following:

$$\rho_D = \frac{9}{2}\frac{mc}{e^2 h}\frac{n_o}{(n_o^2 + 2)^2 f_D}\beta_{abs}\gamma\hbar \tag{2.5}$$

where e and m are the electronic charge and mass, respectively, h represents Planck's constant, c is the speed of light, and n_o is the real part of the index of refraction of the host medium [80] . Equation 2.5 also assumes the area under the defect absorption band to be Lorentzian [80]. For different F centers in sapphire, a set of constants that are equivalent to $\frac{9}{2}\frac{mc}{e^2 h}\frac{n_o}{(n_o^2+2)^2 f_D}\gamma\hbar$ were determined through experiment and could be used to estimate a range for the total anionic vacancy concentration associated with F and F^+ centers. The resulting expression for the vacancy concentration is as follows:

$$[V_o] = [F] + [F^+] = (1.86\beta_{206} + 0.292\beta_{225} + 0.167\beta_{255}) \text{ x } 10^{16} = 4.2 \text{ x } 10^{15} \text{ to } 7.2 \text{ x } 10^{16} \text{ cm}^{-3} \tag{2.6}$$

where β_{206}, β_{225}, and β_{255} are the sapphire absorption coefficients at wavelengths of 206, 225, and 255 nm, respectively [16], [70], [81].

As shown in Fig. 2.3, samples that were grown by the HEM show a much higher oxygen vacancy content compared to the sample manufactured by the Kyropoulos method. Indeed, HEM has been known for causing significant numbers of oxygen vacancies due to the growth environment,[16], [79], [82] but results in Fig. 2.3 also indicate that vacancy concentrations can vary greatly in HEM-grown samples. Both GTAT 1 and 2 have absorption coefficients that are approximately one order of magnitude below the values for GTAT 3 produced by the same manufacturer using the same technique. This wide variation might be related to boule-level inhomogeneity produced during the crystal growth process or to post-growth treatments. It is well known that the structure as well as the defect concentration in the region near the crystallization front is significantly different from those in other regions of the bulk [16]. Even a relatively small temperature gradient can result in variations in sapphire composition [16]. On the other hand, KO 1 shows broader vacancy-related absorption bands, suggesting a low vacancy concentration. It seems possible that the KO sample was grown in a more oxidizing environment. Oxidizing conditions during both crystal growth and post-growth processing have the tendency to remove oxygen vacancies [70].

Just as the formation of vacancies can be related to the chemistry present during the growth process, impurity elements can also be introduced during crystal growth. These impurities tend to occupy either the lattice sites if they are chemically similar to the matrix atoms or the interstitial sites if they are smaller in size [16]. Common isovalent impurity elements include Cr^{3+}, Ti^{3+}, Co^{3+}, Ni^{3+}, Fe^{3+}, Mn^{3+}, and V^{3+}. They can trap both electrons and holes to increase the absorption loss [16], [34]. Other heterovalent impurities such as Cr^{4+}, Ti^{4+}, Si^{4+}, Mg^{2+}, Fe^{2+}, and Li^{+} have also been found in sapphire and they are responsible for the creation of cationic vacancies [16]. Although the impurity concentrations of each species are not exactly known in the samples in this work, the concentration levels are typically in the ppm range according to previous studies [34], [83], [84]. The sources of these impurities could be the melt during production of the seed crystal or during growth using the HEM and Kyropoulos processes [16], [85]. Both manufacturing methods use refractory crucibles and these are typically made using tungsten or molybdenum alloys which contain elements such as Cr and Ti. Elemental diffusion from the crucible to the melt can occur [16]. For both GTAT and Guild samples, the absorption bands related to Cr^{3+}, Ti^{+3}, Fe^{+3}, and V^{+3} are evident in Fig. 2.3. Differences in the coefficient levels reported in Table 2.3 suggest that there are variations in the corresponding impurity concentrations, but detailed interpretation of the absorption measurements requires care. While GTAT 1, 2, 3 and Guild 1 follow a consistent decreasing trend in the measured wavelength region shown in Fig. 2.3, an inconsistency of the KO absorption values can be observed. At certain wavelengths (i.e. 230 nm), the KO sample has the lowest overall absorption value but at other wavelengths (i.e. 330 nm), it has the highest value. It is difficult to explain the observed absorption behavior of KO sapphire, but it might be related to additional impurities present in the sample that do not occur in the other materials. Indeed, impurity concentrations measured by ICP-MS will be presented in Chapter 4 in GTAT 1, Guild 1, and KO 1, and their relationships with the observed absorption losses will be discussed.

While standard UV-VIS measurements can provide useful information in wavelength regions where absorption is relatively high, techniques such as PCI are needed in other regions since the measurement background for UV-VIS is high when determining optical loss. In regions where the measurements can be compared, differences between the techniques must be considered. UV-VIS measurements are typically representative of large regions of the sample while PCI measurements generally represent relatively small volumes. Since there are sample-to-sample variations indicated by the UV-VIS measurements, multiple PCI measurements within specific samples must be made to establish an average value indicative of the bulk property. PCI measurements were performed at three wavelengths and representative results for Guild 1 measured at 1064 nm are shown in Fig. 2.4(a) and Fig. 2.4(b). The absorption coefficient is plotted as a function of the distance either along the sample thickness (for the longitudinal scan) or along the sample horizontally (for the transverse scan). As shown in Fig. 2.4(a), two absorption maxima show up at 1.2 and 6.2 mm that are related to an increase in the signal at the air/sample boundary where the pump beam enters and exits the sample. Moreover, the longitudinal scan distance was affected by both a slight sample tilt and the refractive index of the sample so the distance shown in Fig. 2.4(a) appears to be shorter than the sample thickness [69]. For this particular measurement, the measured absorption values between 2 and 5.5 mm were recorded for the calculation of the mean bulk absorption coefficient. A subsequent transverse scan was performed along the sample at a depth of 3 mm to check sample homogeneity. The results shown in Fig. 2.4(b) indicate that the absorption coefficient in the central region of the sample is generally uniform, but at two locations, the absorption seems to increase slightly possibly due to increased defect concentration in these regions. The absorption coefficients obtained from the transverse scan were then added to the values acquired from the longitudinal scan to compute the final average bulk absorption coefficient of the sample at 1064 nm.

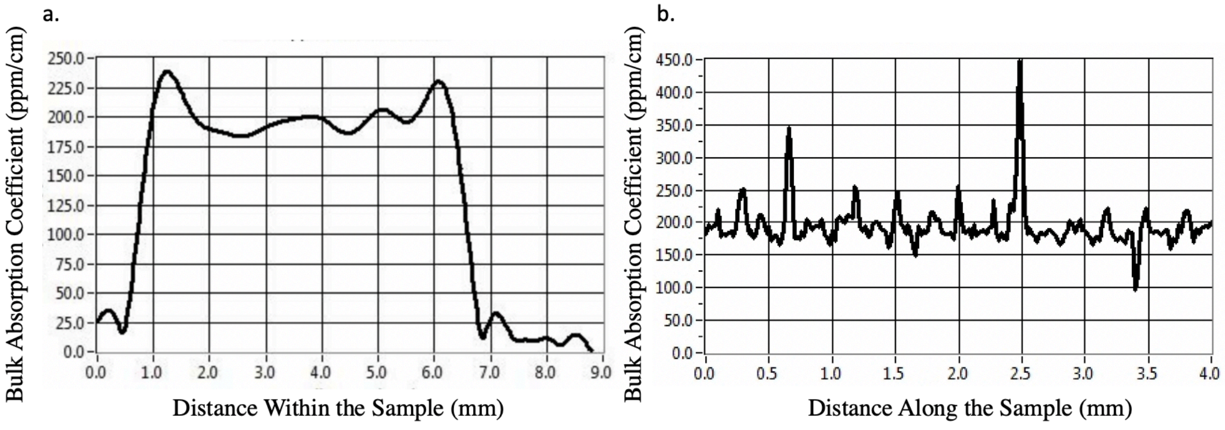

Figure 2.4. (a) A longitudinal scan of bulk absorption as a function of position through the thickness of Guild 1 obtained at 1064 nm using the PCI technique; (b) A PCI transverse scan performed along the center of Guild 1 at 1064 nm.

Table 2.4 summarizes the bulk absorption coefficients for GTAT 1-3, Guild 1, and KO 1. It appeared that the KO sapphire had more variation in the PCI results obtained in both the longitudinal and transverse scans at all wavelengths and a standard deviation is reported for the measurements in that sample. Overall, the absolute bulk absorption coefficients at 355 nm and 532 nm shown in Table 2.4 are in a good agreement with the calculated absorption values based on the UV-VIS results in Table 2.3. Furthermore, the values from Table 2.4 were plotted together with the results obtained using two bulk absorption models (shown in Fig. 2.5). Both models are an extended version of the absorption model shown in Fig. 2.3 with different fitting parameters. The

Table 2.4. Bulk Absorption Values Obtained from PCI Measurements

	Bulk Absorption Coefficient (ppm/cm) at Wavelength		
	355 nm	532 nm	1064 nm
GTAT 1	1870	1710	64
GTAT 2	1790	1070	45
GTAT 3	4590	6210	180
Guild 1	15000	9250	189
KO 1	6580±573	4950± 590	1276±564

(PCI data of GTAT samples were provided by Kurt Schmid from GTAT[62]) bulk absorption model 1 in Fig. 2.5 represents a model fit to the averaged PCI-based bulk absorption coefficients of GTAT 3 and Guild 1, while the bulk absorption model 2 displays another model fit to the averaged absorption coefficients of KO 1 and the bulk absorption model 3 exhibits the model fit to those of GTAT 1 and 2. According to the modeled results, the absorption coefficient at 532 nm should be slightly higher than the one at 355 nm due to Ti^{3+} impurity. The UV-VIS results in Fig. 2.3 suggest that all samples except KO 1 have a comparable or slightly higher absorption value at 532 nm compared to the one at 355 nm. However, data from Table 2.4 indicates only GTAT 3 follows this trend while GTAT 1 has comparable values at both wavelengths. A possible explanation for this might be that the Ti^{3+} impurity concentration is relatively low in these other samples. Compared to previously reported sapphire absorption coefficients at 1064 nm, both GTAT 1 and 2 indicate that a low loss level (as low as 10^{-5} cm^{-1}) is achievable with the current HEM growth method. In the case of KO 1 at 1064 nm, the high absorption loss is likely due to an impurity related defect band that occurs in the region between 700 nm to 1000 nm. Previous studies have shown that transitions between Ti^{3+} and Ti^{4+} (near 800 nm) as well as Fe^{3+} to Fe^{2+} (near 900 nm) are likely in the as-grown sapphire [86]–[88]. Again, detailed discussion will be presented in Chapter 5 with the impurity concentrations in different sapphire samples obtained using ICP-MS.

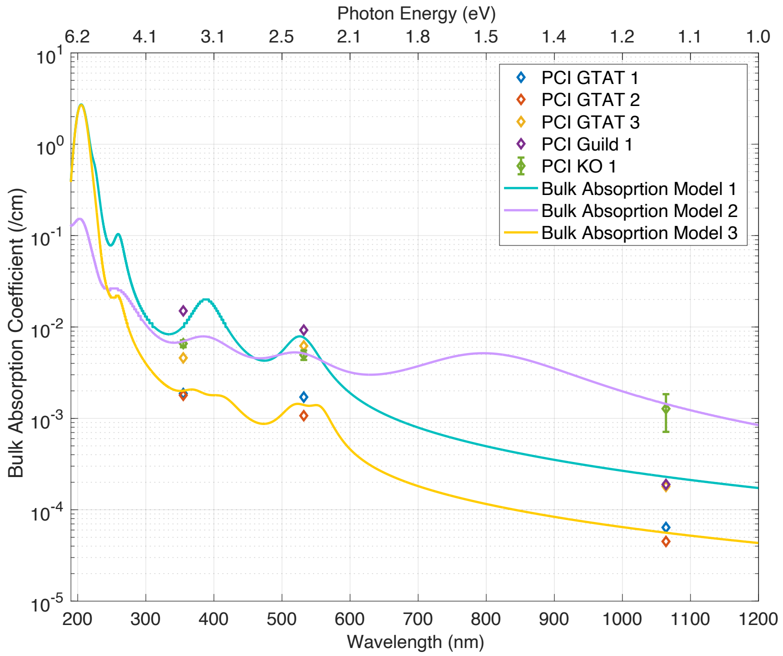

Figure 2.5. PCI results (at 355 nm, 532 nm, and 1064 nm) for GTAT 1-3, KO 1, and Guild 1 are shown using blue, red, yellow, green, and purple diamonds, respectively. The teal, light purple, and yellow solid lines represent the bulk absorption models with different defect concentrations.

The wavelength range between 600 and 1200 nm is generally known as the transparent region for sapphire where no absorption should occur [6], [81]. However, according to the absorption model shown in Fig. 2.5, there is weak absorption in this region that has a form related to Eq. (2.4) . Even though the only PCI measurement in this region was made at 1064 nm, the model shown in Fig. 6 was developed by fitting laser calorimetry data reported previously [6], [23]. This weak absorption tail has been described for amorphous materials and semiconductors and is related to states in the bandgap generated by lattice disorder, impurities, and other defects [13], [89]–[91]. Charged dislocations and dangling bonds were found to be primarily responsible for weak absorption in semiconductors and fibers [13], [92]–[94]. In these materials, defects can generate energy states with discrete levels within the bandgap and these have been associated with an exponential variation for the absorption loss. For ionic insulators, Seitz suggested that edge-type dislocations could be responsible for enhancements of absorption in the transparent region due to lattice distortion that accompanies these types of defects [95]. Since dislocation cores contain rows of atoms with broken bonds, these atoms are likely to trap electrons or provide unpaired electrons to other centers thus generating localized electric field effects [95]. The two most common causes for dislocation creation during sapphire growth are dislocation inheritance from the seed crystal and thermoelastic stress-induced plastic deformation [16]. A general estimate of the density of dislocations caused by these two mechanisms is in the range of 10^4 to 10^6 cm/cm^3 [16]. Furthermore, it is also likely that the presence of jogs on edge dislocations in ionic crystals promotes the absorption loss in the transparent region since these can contribute additional energy states to the system [81]. The results presented here suggest that lattice distortions may give a rise to long wavelength absorption in crystalline materials that is analogous to the observed behaviors in amorphous and glassy materials [81], [95]. On the other hand, previous DFT calculations have shown that cationic vacancy-type defects in sapphire could also generate a weak absorption loss in the near-IR region [96]. Additionally, impurity elements such as Ti^{4+} and Fe^{2+} along with some of the vacancy-impurity complex clusters have also been considered as the origin of the observed residual absorption [48], [86]. Therefore, it is possible that grown-in dislocations along with decoration by vacancies and impurity elements in synthetic single crystal sapphire produce a relatively weak absorption loss in the transparent region.

Surface absorbance PCI results obtained for different sapphire samples are shown in Table 2.5. Compared to the bulk absorption coefficient of each sample at each measured wavelength, the surface absorption loss is relatively small. Impurity elements such as C, Si, and Cl were likely to be introduced to the sample surface during the chemical-mechanical polishing process [97].

Furthermore, vacancies and dislocations generated during the grinding and polishing processes could also contribute to the surface absorption loss [98], [99].

Table 2.5. Surface Absorbance Values Obtained of GTAT 1-3 and Guild 1 from PCI Measurements

Sample	Surface Absorbance (ppm) at Wavelength		
	355 nm	532 nm	1064 nm
GTAT 1	284	131	7.8
GTAT 2	208	81.1	4.8
GTAT 3	940	426	20.5
Guild 1	N/A	1460	6.45

(PCI data of GTAT samples were provided by Kurt Schmid from GTAT[62])

2.3.2 Spinel

In this section, we discuss the UV-VIS transmittance measurements of different spinel samples. Following a similar procedure as described for the sapphire samples, the bulk absorption coefficients were calculated for CN Disk 1, CN SQ 2, and JHUAPL Disk in the wavelength region between 200 nm to 650 nm to identify potential absorption band features. Results shown in Fig. 2.6 indicate that the absorption coefficients for all the three spinel samples are enhanced in bands centered at various wavelengths, but these bands are relatively broad compared to those of sapphire suggesting overlaps between multiple defect bands. In the wavelength region between 200 nm (6.2 eV) and 250 nm (4.95 eV), all three spinel samples show an absorption band that is associated with F centers [40], [41]. In CN Disk1 and JHUAPL Disk, the F center-associated band centered around 230 nm further extends to the shorter wavelength region, indicating another adjacent defect band such as Fe^{3+} [41]. CN SQ 2 and CN Disk 1 have a broad band feature that extends to the longer wavelength, which is caused by additional vacancies and impurities. For example, F^+ centers, Fe^{3+}, and Mn^{2+} impurities have been reported to cause absorption bands at 261 nm (4.75 eV), 258 nm (4.8 eV), and 275 nm (4.5 eV), respectively [40], [41]. Furthermore, the absorption band of CN Disk 1 observed near 280 nm further broadens into the shorter 300 nm region indicating the existence of V centers (holes trapped by an oxygen ion near a cationic vacancy) in this sample.

Ibarra *et al.* have previously reported broad absorption bands due to V centers at 317 nm (3.9 eV), 344 nm (3.6 eV), 399 nm (3.1 eV), and 442 nm (2.8 eV) [47]. Additionally, Cr^{3+} has been identified as another defect that is responsible for the optical losses at ~365 nm, ~390 nm, and ~540 nm. Similarly, V^{3+} has also been reported to be responsible for the absorption loss in the region between 365 nm and 400 nm in spinel [40], [41]. Moving further to the region between 400 nm and 500 nm, although no apparent absorption bands are observed in three spinel samples shown in Fig.2.6, a broad background still exists in that region in all samples that could be related to a few defect types. Indeed, Cr^{3+}, V^{3+}, and F center have been reported to cause a broad absorption band near 480 nm [41]. Moreover, Ti^{3+} is also linked to a broad band at 490 nm that extends into the 500 nm region [100]. Lastly, absorption loss due to Mn^{2+} at 515 nm is also possible in all samples [40].

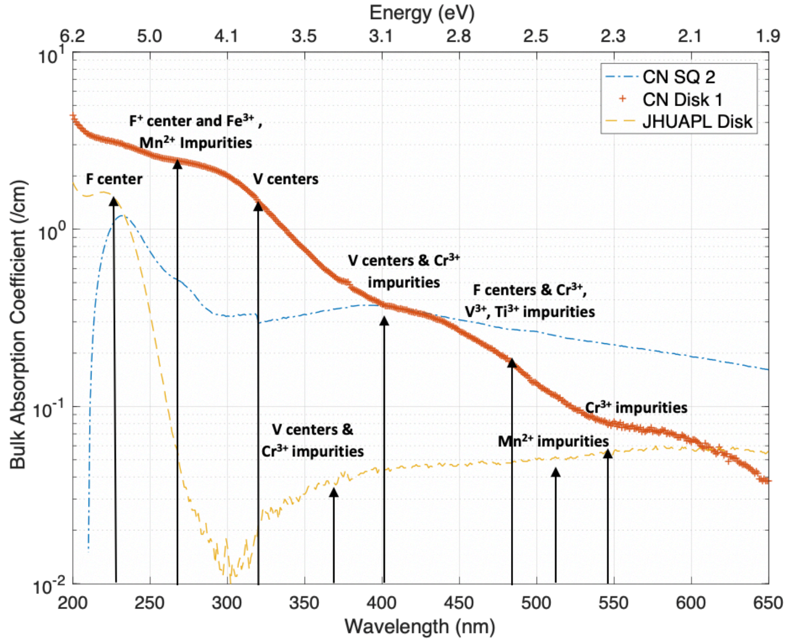

Figure 2.6. Absorption coefficients for CN SQ 2, CN Disk 1, and JHUAPL 1 as a function of wavelength shown in broken blue lines, orange asterisks, and yellow broken lines, respectively. The associated impurity bands were identified and labeled.

Table 2.6 summarizes the bulk absorption coefficients and surface absorbance for different spinel samples at three wavelengths. Compared to the sapphire samples, these samples show more variations in the PCI results due to bulk and surface inhomogeneities such as grain boundaries and variable stoichiometries. Overall, at 355 nm and 532 nm, the PCI-measured absolute bulk absorption coefficients of all three spinel samples (Table 2.6) are in a good agreement with the calculated absorption values shown in Fig 2.6. For CN SQ and JHUAPL Disk samples, PCI-based absorption coefficients at different wavelengths can differ by a factor of two to three depending the locations within the sample. These large differences indicate a higher level of inhomogeneity in spinel which is primarily due to impurities trapped at the grain boundaries [31]. Furthermore, stoichiometry variations related to the presence of MgO in local regions of a spinel can also result in wide-ranging absorption loss [101], [102]. Therefore, values acquired from both types of measurements (UV-VIS and PCI) can be used to provide a range for the absorption loss in different samples at the measured wavelengths.

Table 2.6. Absorption and Surface Absorbance Value of Spinel Samples Obtained from PCI Measurements

Sample	Surface Absorbance (ppm) and Bulk Absorption Coefficient (ppm/cm) at Wavelength					
	355 nm		532 nm		1064 nm	
	Surface	Bulk	Surface	Bulk	Surface	Bulk
CN Disk 1	N/A	2700000	N/A	43000	3 to 3.5	200
CN SQ 1	N/A	200000 to 700000	1640	65500	129	5730
CN SQ 2	N/A	200000 to 700000	1100 to 1500	50000 to 100000	140 to 170	5000 to 10000
JHUAPL Disk	800	45500*	303	20100*	239	12600±7620

*Higher bulk loss values by a factor of two to three has been observed in some locations

The bulk absorption coefficients of CN Disk1, CN SQ 1, and JHUAPL Disk from Table 2.6 were plotted with two bulk absorption models and the comparison is shown in Fig. 2.7. The bulk absorption model 4 in Fig. 2.7 represents a model fit to the PCI-based bulk absorption coefficients of CN SQ 1, while the bulk absorption model 5 displays another model fitting to the absorption coefficients of JHUAPL Disk (using its lower loss values). For the JHUAPL Disk, the small decrease of the absorption loss between 532 nm and 1064 nm suggests the possibility of a Ti-associated impurity band in the 780 nm wavelength region related to a transition between Ti^{3+} and Ti^{4+} [103]. For CN Disk 1, the model fitting does not apply because the absorption shows a very high loss in the visible and a super low loss in the near-infrared, deviating from other "traditional" spinel samples. Special treatments such as secondary annealing and irradiation or different sintering parameters could account for the observed absorption behavior in CN Disk 1 [104].

The mechanisms behind the optical absorption in spinel are more complicated compared to those in sapphire. Similar to sapphire, both impurities and lattice defects play a role in the absorption loss [40], [41], [59]. The common impurity species found in sapphire also exist in spinel with a different valence state to accommodate Mg^{2+}. For example, Mn was found to exist in sapphire with a 2+ state while its 3+ state has been found to be prevalent in spinel [40]. Furthermore, both anionic and cationic vacancies are commonly found in synthetic spinel but their formation mechanisms are different from those of sapphire. Because spinel is a solid solution of MgO and Al_2O_3 and the solubility of Al_2O_3 is relatively large (i.e. $MgO \cdot nAl_2O_3$, $1 \leq n \leq 7$), the stoichiometry plays an important role in the resulting spinel physical properties [40]. Previous studies have shown that when $n>1$, additional cationic vacancies must be formed to compensate the excess positive charges due to Al, whereas when $n<1$, anionic vacancies are more likely to present [40]. Both vacancy types form color centers that are responsible for different absorption bands observed in the UV and visible wavelength regions. Interestingly, Dericioglu et al. has reported that with $n=2$, the transmittance of spinel increased in the near-IR wavelength region along with an enhanced fracture toughness compared to spinel samples with stoichiometries of $n= 1$ and 1.5 [102]. Additionally, antisite defects such as $\mathrm{Mg}_{\mathrm{Al}}^{-}$ and $\mathrm{Al}_{\mathrm{Mg}}^{+}$ have been found to be inevitable in synthetic spinel which results in additional defect bands [40] . Moreover, these lattice defects can be further impacted by the calcination and sintering processes since both time and temperature used in these heat treatments can alter the kinetics of defects formation and their spatial distribution [40]. Similar to sapphire, these vacancy defects often couple with different impurity elements to form defect complexes that result in optical absorption loss in the near-IR region in spinel [105]. With these statements in mind, the results in Fig. 2.7 indicate that the JHUAPL Disk should have a relatively low-level concentration of different impurity species and color centers compared to the CN samples. The CN samples were produced without using sintering aids, and a relatively high concentration of impurities is expected since sintering aids typically reduce the impurity levels in spinel [31], [106]. However, while JHUAPL Disk shows reduced absorption band in the UV-Vis region, it has a high absorption loss in the near-IR region possibly due to $\mathrm{Ti}^{3+}/\mathrm{Ti}^{4+}$ and $\mathrm{Fe}^{2+}/\mathrm{Fe}^{3+}$ associated transitions [103], [107]. Although all CN spinel samples were made from the same starting powder according to the manufacturer, the large differences in absorption at different wavelengths (Fig. 2.6) suggest that different heat treatments were used in the production of these samples. Previous findings by other researchers have indicated that different sintering and annealing parameters can shift absorption bands toward different regions to obtain desired optical properties [40]. For CN Disk 1, a trade-off between absorption in the UV-Visible region and near-IR region might have resulted from special heat treatment processes or using different sintering parameters.

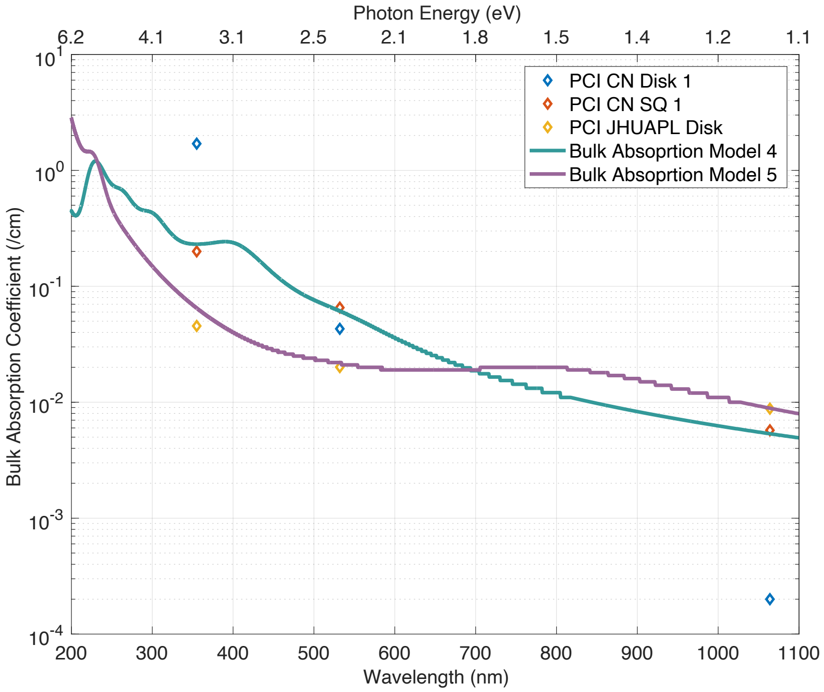

Figure 2.7. PCI results (at 355 nm, 532 nm, and 1064 nm) for CN Disk 1, CN SQ 1, and JHUAPL Disk are shown using blue, orange, and yellow diamonds, respectively. Both dark teal and dark purple solid lines represent the bulk absorption models with different defect concentrations.

2.3.3 Photothermal heating of spinel

In test run #1, the JHUAPL Disk was heated by a 150-W CW laser for about 50 seconds and images were taken using the long-wave infrared camera (Fig. 2.8). Figure 2.8 (a)-(d) represents different stages of the JHUAPL Disk during the laser heating. When the laser was off initially, no light emission at 0 second and when the laser was turned on, as heating time progressed, a thermal blooming event was observed and it is presented in Figs.2.8 (b)-(d). As shown in these figures, the laser beam traveled through the center region of the sample and the same center region became heated quickly. As time elapsed, thermal diffusion toward the edge of the sample was observed. Since photothermal heating in an optical window is likely to induce beam distortion, a subsequent test run was performed using two lasers with one transmitted through the sample hitting a ceramic plate in the back and the other traveled directly to the same plate. Using a camera operating at the visible wavelength, the two laser beam spots being reflected off the plate were recorded and the difference was detected. According to Figs.2.9 (a) and (b), at early times, the two beam spots (left beam traveled through the sample) reflected from the ceramic plate were nearly identical; however, after being turned on for approximately two minutes, the left beam experienced a distortion that was likely caused by thermal lensing as the spot shape became smaller and focused shown in Fig. 2.9(b).

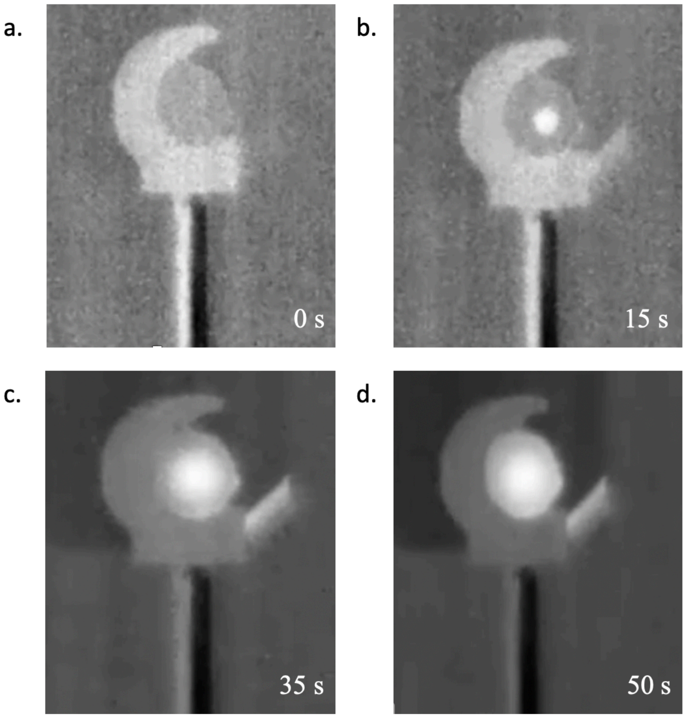

Figure 2.8. A series of images taken during the photothermal heating experiment using a long-wave infrared camera showing the thermal blooming phenomenon in JHUAPL Disk at (a). 0 second; (b). 15 seconds;(c) 35 seconds; (d) 50 seconds.

Frame data were extracted from Fig. 2.8 to obtain a temperature rise profile in the center region of the sample where the laser beam traveled through. The temperature rise in this region should be the highest throughout the entire experiment since the thermal diffusion effect there was negligible under the continuous heating. Figure 2.10 shows such temperature rise profile along with simulation results generated using COMSOL for the same region. For the COMSOL

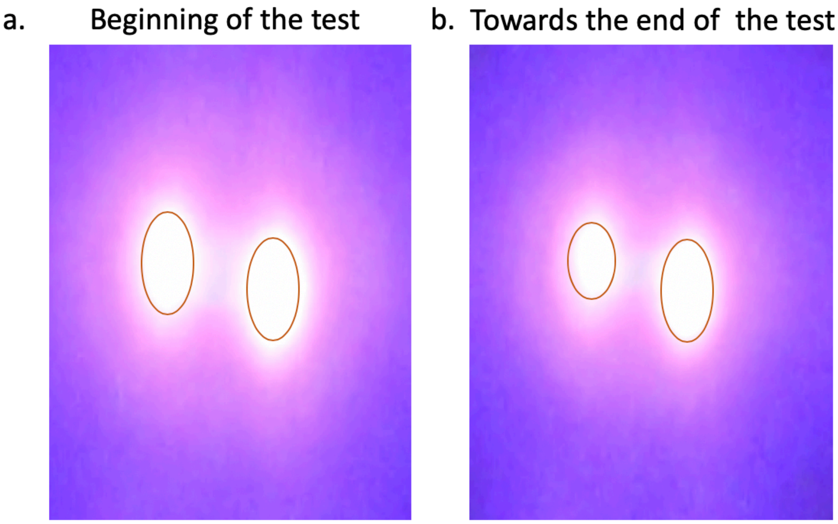

Figure 2.9. Beam distortion observed during the HEL heating;(a) Scattered beam patterns at the beginning of the test without heating up the window;(b) Scattered beam patterns at the end of the test with one beam passed through the heated spinel window.

simulation, the heat source was modeled as a Gaussian beam with a form that has been used previously by other investigators [108]. The mesh of the sample was created based on the sample's physical dimensions and an optical absorption coefficient of 0.015 cm^{-1} (based on the PCI measurements) was used. Additionally, a convective air-cooling boundary condition was applied using a heat transfer coefficient of 5 W/m^2K. However, it was observed that the convective cooling had a negligible effect on the temperature profile during heating and only became important in the cooling process. A closer examination of Fig. 2.10 suggests that both the heating rate and peak temperature from simulation are slightly lower than the experimental results. The measured temperatures are 2 to 3 °C higher than that from simulation after 15 seconds of heating. Possible causes for the observed deviations are probably related to camera calibration as well as stray infrared being collected by the camera at different wavelengths. Nevertheless, the purpose of the comparison is to show the level of the absorption measured in JHUAPL Disk could induce a large temperature rise that leads to beam distortion effect. A more accurate temperature rise profile can be acquired using a well calibrated thermal camera with the measured spectral response function and different optical filters.

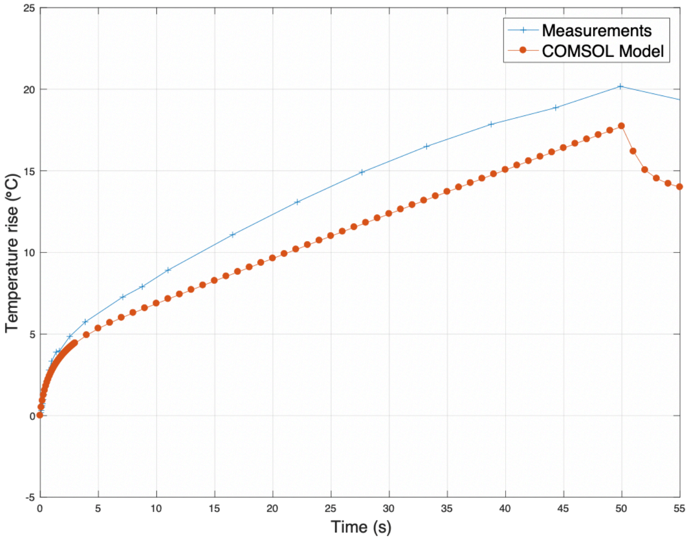

Figure 2.10. Temperature rise profiles obtained from the photothermal heating measurements and a COMSOL laser heating simulation of JHUAPL Disk surface shown in blue and orange connected lines, respectively.

2.3.4 Conclusion

In this Chapter, we showed that the bulk absorption coefficients of different sapphire samples are in the range of 10^{-5} to 10^{-2} cm^{-1} for wavelengths of 355 to 1064 nm while those for spinel lie in the range of 10^{-4} to 10^{0} cm^{-1}. The surface absorbance values for all samples at the measured wavelengths are at the level of 1 to 1000 ppm. The absorption loss is most likely due to the charged lattice defects and impurities in these materials. Based on an empirically derived model, these defects could introduce extra discrete energy states within the band gap that lead to a weak absorption tail in the transparent region of the material. The presence of grain boundaries and issues with stoichiometry in polycrystalline spinel even contributed more to its absorption loss. Lastly, as indicated by the photothermal experiments, an absorption level at 0.01 cm^{-1} of JHUAPL Disk could lead to a temperature rise of 20 °C when being heated with a 150W cw laser at 1 μm.

The photothermal heating also led to a thermal blooming effect which degraded the laser beam quality.

Chapter 3. Optical Scattering Measurements

3.1 Introduction

Both bulk defects and surface structures can result in different levels of optical scattering in sapphire and spinel. According to previous studies, the scattering loss of both sapphire and spinel have been reported to be at levels ranging between 10^{-3} to 10^{-1}/cm in the near-infrared region [62], [109]. The scattering level is relatively high in these materials compared to their absorption losses owing to elevated defect concentrations near/at the surface due to grinding and polishing processes (main case for sapphire) along with grain boundaries and pores in the bulk (main case for spinel). However, only limited scattering experimental data from previous studies are available for these materials and a detailed investigation is needed to understand the scattering mechanisms to further reduce the loss in both sapphire and spinel, as required for HEL window materials.

Two common metrics for quantifying optical scatter are the bidirectional scatter distribution function (BSDF) and the total integrated scatter (TIS). The BSDF is used to quantify the angular distribution of scattered light from an interface [25]. Formally, the BSDF is defined as the surface radiance divided by the incident surface irradiance, where the surface irradiance is the light flux incident on the surface per illuminated surface area. The scattered surface radiance then becomes the light scattered through the solid angle Ω per unit illuminated surface area per unit projected solid angle and is given by the following:

$$\mathrm{BSDF} \cong \frac{\mathrm{P_s}/\Omega}{\mathrm{P_i}\cos\theta_s} \tag{3.1}$$

where P_i and P_s are the incident and radiated light power (in Watts) and the $\cos\theta_s$ term can be viewed as a correction factor for adjusting the illuminated area to its apparent size when viewed from the scattering direction [25]. However, for the actual experimental measurements, the cosine term is often dropped because the illuminated surface area concept does not hold when both surface and bulk scatter are present and the traditional BSDF becomes the cosine-corrected BSDF [25]. The BSDF value depends on both incident direction and scatter direction, hence the name bidirectional. The typical BSDF value can exceed 10^6/sr in the specular direction in the case of small solid angles and deviating from the specular peak, while the value can be as low as 10^{-9}/sr when scattering loss becomes minimal and all signals are noise due to the surrounding air molecules [25]. Therefore, the light scattered from a sample into any solid angle can be found by multiplying the cosine-corrected BSDF by the incident light flux and the solid angle of interest [25]. Typically, the instrument used to measure the TIS collects nearly all the scattered light using a reflective hemisphere equipped with a single photodetector. The measured scattered light is then normalized by the total reflected power to yield the TIS value [25]. It can also be obtained by integrating the BSDF function over the hemisphere of interest.

In this work, a bidirectional scatterance probability distribution function (BSPDF) instrument was used to quantify scatterance in sapphire and spinel. Sapphire samples with different polishing conditions were used to examine the impact of surface polish on the scattering loss. Scatterance data of selected sapphire samples were interpreted using a simple, single-scatter model to understand the defect size distribution responsible for this type of loss since single-scatter mainly contributes to the scatterance in sapphire. For spinel samples, coated sphere anomalous diffraction (ADA) and spherical ADA models were used to deduce the scatter sources in the polycrystalline samples. A Kubelka-Munk wavelength dependent scatter coefficient model that was developed using the ADA models was applied to the measured diffuse scatterance losses in selected spinel samples.

3.2 Materials and Methods

3.2.1 Materials

In addition to the samples presented in Table 2.2, thin samples of both sapphire and spinel were used to evaluate the relative contributions of surface and bulk scattering losses to overall loss in samples from each manufacturer. Information about the additional samples is given in Table 3.1.

Table 3.1. Specifications and Synthesis Methods of Additional Sapphire and Spinel Samples Used in Scattering Measurements

Sample	Thickness (mm)	Scratch/Dig	Synthesis Method
GTAT 4	1.14	<40/20	HEM
Guild 2	1.03	<40/20	HEM
KO 2	1.09	<60/40	Kyropoulos
CN Disk 2	0.55	<60/20	Conventional sintering with subsequent HIP

3.2.2 Optical and Electron Microscopy

Optical micrographs using a Zeiss Axio Zoom stereo microscope (with a magnification ranges between 10x to 55x) and a Zeiss LSM 700 laser scanning confocal microscope (with both 10x and 20x objective lenses) were captured on selected sapphire and spinel samples to reveal surface irregularities (i.e. scratches and digs). Backscattered electron (BSE) images were acquired using Thermo Scientific Helios G4 UC to gather spinel grain size information.

3.2.3 AFM

The root-mean-square (RMS) surface roughness of different sapphire samples was obtained using a Bruker Dimension 3100 atomic force microscope using tapping mode. The sampling area was chosen as 100 μm × 100 μm on the center of each sample with a spatial resolution of 256 scans/μm. Other sampling areas such as 80 μm × 80 μm and 40 μm × 40 μm were also used on selected samples. A silicon tip with no coating that has a force constant of 40 N/m and a tip radius less than 10 nm was used. The AFM maps of surface topography provide more complete information about the surface condition than do scratch and dig numbers and can be used to assess the importance of surface topography to scattering.

For different spinel samples, the AFM measurements were performed by MSE Supplies LLC under tapping mode. The sampling area was chosen as 50 μm × 50 μm on the center of each sample with a spatial resolution of 256 scans/μm. An aluminum coated silicon tip that has a force constant of 0.4 N/m and a tip radius of 2 nm was used.

3.2.4 BSPDF

A BSPDF instrument, shown schematically in Fig. 3.1, was used to perform scattering measurements at laser wavelengths of 405, 532, 633, 1064 and 1550 nm. Continuous wave lasers with different wavelengths were used and each laser was modulated with a mechanical chopper to allow for coherent detection. A switchable, amplified photodetector (Si or Ge based, depending on the detection wavelength) was used to detect the scattered light. The photodetector was rotated about the sample through an arc of 360° at a step size of 1° to capture the scatterance at each in-plane angle. The detector output was measured by a lock-in amplifier allowing the acquisition of low-level signals. In addition, a reference photodetector was used to monitor the background drift in the laser power to improve the accuracy of the measurement. To measure the specular reflectance, an incident angle of 10° was chosen for all measurements to prevent the blocking of the incident beam by the detector that occurs if a normally-incident beam were used. A Labsphere NIST-calibrated Spectralon sample with 99.9% diffuse reflectance was used as a reference and also to establish the correct distance between the sample and the detector. A LabVIEW program was used to control motion stages for both the sample and the detector as well as to monitor the entire measurement process.

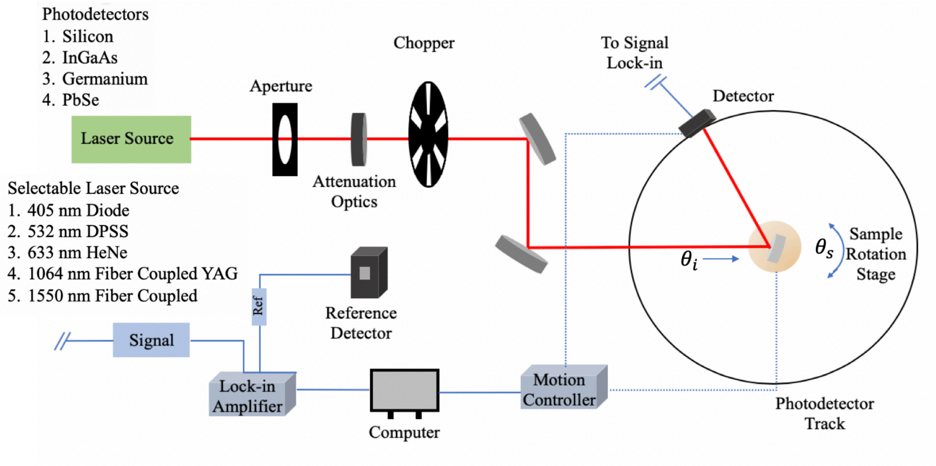

Figure 3.1. Schematic illustration of the BSPDF instrument. The laser beam travels through a series of focusing optics to the sample. The detector rotates around the sample (in-plane with the incident beam) while acquiring the angularly-resolved scatterance. The data acquisition is automated and controlled by a LabVIEW program.

For a BSPDF measurement from a flat surface, the measured hemispherical incremental scatterance flux, $\Delta\Phi_s(\theta_s, \theta_i)$, per incremental steradian, is proportional to the phase function, $P(\theta_s, \theta_i)$, as follows:

$$\frac{\Delta\Phi_s(\theta_s, \theta_i)}{\Phi_i \Delta\Omega_s} = \alpha_{hem}(\theta_s, \theta_i) = \alpha_{hem}(\theta_i) P(\theta_s, \theta_i) \tag{3.2}$$

where Φ_i is the incident flux, Ω_s is the incremental solid angle in steradians, $\alpha_{hem}(\theta_s, \theta_i)$ is hemispherical the BSPDF, $\alpha_{hem}(\theta_i)$ is the hemispherical total integrated scatterance (TIS) for each phase function, θ_s is the incremental scattering angle, and θ_i is the incident beam angle. The left part of the equation is obtained experimentally using measured fluxes. The incremental solid angle is approximated using the photodetector area divided by the distance between the sample and the detector. The right part of the equation is obtained using models based on scattering theory. The phase functions for specular components, near-specular components, diffuse components, and Lambertian components of both transmitted and reflected beams are used to fit the measured BSPDF [110]. The combination of these phase functions serves as an angularly-resolved scatterance model which is called the bidirectional scatterance probability distribution function. The BSPDF is often separated into bidirectional reflectance probability distribution function (BRPDF) and bidirectional transmittance probability distribution function (BTPDF). The functional forms of the BRPDF and the BSPDF can be expressed as follows:

$$\mathrm{BRPDF}(\theta_s, \theta_i) = \rho_{in} P_{in}(\theta_s, \theta_i) + \rho_{ns} P_{ns}(\theta_s, \theta_i) + \rho_{diff} P_{diff}(\theta_s, \theta_i, m, \alpha) + \rho_L P_L(\theta_s) \tag{3.3}$$

$$\mathrm{BTPDF}(\theta_s, \theta_i) = \tau_{in} P_{in}(\theta_s, \theta_i) + \tau_{ns} P_{ns}(\theta_s, \theta_i) + \tau_{diff} P_{diff}(\theta_s, \theta_i, m, \alpha) + \tau_L P_L(\theta_s) \tag{3.4}$$

where ρ and τ are the total integrated reflectance (TIR) and the total integrated transmittance (TIT), and the subscripts in, ns, diff, and L refer to the specular, near-specular, diffuse and Lambertian scattering components, respectively. Additionally, α is the half-angle of the reflected beam while m is an exponent that is selected to fit the data. Detailed derivations of each phase function were previously reported by Springer *et al.*[110]. Two major assumptions were made when using the phase functions to fit the experimental data in this work: 1. Neither azimuthal angle dependence nor polarization effects were considered and 2. For all sapphire samples, no preferred surface height variations or crystallographic orientation were considered. The first assumption likely holds since all samples were illuminated with near-normal incidence so that any polarization effects were minimized [111], [112]. The second assumption relates primarily to the surface height statistics. Since all samples were prepared with the c-axis normal to the sample flats (which were parallel) and were optically polished, stationary surface statistics could be assumed.

All measurements were calibrated using an instrumental phase function. This function was obtained by first measuring the specular transmittance in the absence of the sample at each wavelength of interest. Next, the measured data were fit using the corresponding instrument phase function as is shown in Fig. 3.2. The instrumental phase function contains two parts, the specular phase function and the diffuse phase function; the former represents the unscattered, transmitted light (dominant) and the latter characterizes weak scattering. The specular phase function includes a 2D convolution of the Gaussian profile of the incident laser beam with the detector's cylindrical function and has the following form:

$$P_{\mathrm{in}}(\theta_{\mathrm{s}},\theta_{\mathrm{i}}) = \mathrm{N}_{\mathrm{in}}(\theta_{\mathrm{i}},w)\left[\mathrm{erf}\left(\frac{\frac{(\cos\theta_{\mathrm{r}}+\sin\theta_{\mathrm{i}})}{\cos\theta_{\mathrm{i}}}+\frac{w}{2}}{c}\right)+\mathrm{erf}\left(\frac{\frac{-(\cos\theta_{\mathrm{r}}+\sin\theta_{\mathrm{i}})}{\cos\theta_{\mathrm{i}}}+\frac{w}{2}}{c}\right)\right] \tag{3.5}$$

where N_{in} is the normalization constant, w is related to the detector width, and c is related to the laser beam width [110]. The diffuse phase function accounts for the partially coherent scatter and has a Lorentzian form given by the following:

$$P_{\mathrm{diff}}(\theta_{\mathrm{s}},\theta_{\mathrm{i}},m,\alpha) = N_{\mathrm{diff}}(\theta_{\mathrm{i}},m,\alpha)\frac{(\alpha\cos\theta_{\mathrm{i}})^{m-1}}{|\sin\theta_{\mathrm{s}}+\sin\theta_{\mathrm{i}}|^{m}+(\alpha\cos\theta_{\mathrm{i}})^{m}}\cos\theta_{\mathrm{s}} \tag{3.6}$$

where α is the half angle of the reflected beam, m is exponent chosen to fit the data, and N_{diff} is the normalization constant [110]. In some cases, an instrument function may also contain a near-specular component which was derived based on the generalized Van Cittert-Zernike theorem and follows a Gaussian form given as follows:

$$P_{\mathrm{ns}}(\theta_{\mathrm{s}},\theta_{\mathrm{i}},C) = N_{\mathrm{ns}}(\theta_{\mathrm{i}},C)\mathrm{e}^{\left\{-\frac{(\sin\theta_{\mathrm{s}}+\sin\theta_{\mathrm{i}})^{2}}{(C\cos\theta_{\mathrm{i}})^{2}}\right\}}\cos\theta_{\mathrm{s}} \tag{3.7}$$

where C is a constant that is empirically chosen based on the BSDF measurement and N_{ns} is the normalization constant. With optimized fitting parameters, the instrument function could be

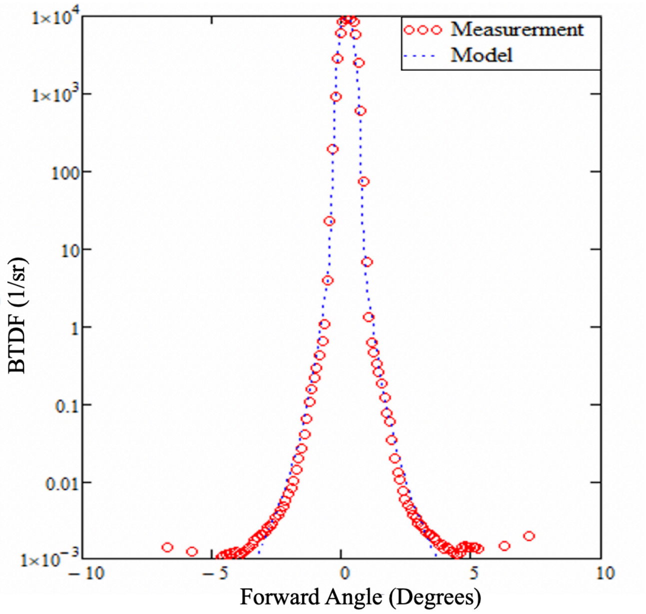

Figure 3.2. The instrument function used for BSPDF measurements at 532 nm. The data were taken at the angle for normal incidence without a sample in place. The model uses both instrument and diffuse phase functions.

integrated to yield a transmittance of unity which is the expected value for a properly-calibrated, specular transmittance measurement in the absence of a sample.

3.2.5 Secondary Surface Polishing

Three sapphire samples, GTAT 1, KO 1, and KO 2 were sent to Coastline Optics to be further polished using a proprietary pitch polishing technique. The resulting scratch/dig specifications of these samples became <5/10. Additional polishing was also performed on CN SQ 2 which had initial as-received scratch/dig were <80/50. After the additional surface polishing by Guild Optical Associates, INC., the resulting scratch/dig numbers became <40/20. Surface evaluations using optical microscopes and AFM as well as scatterance measurements using BSPDF were performed on these extra-polished samples.

3.3 Results

3.3.1 As-Received Sapphire Samples

3.3.1.1 Surface Evaluation by AFM

Extrinsic optical scattering mainly arises from three possible features of a window material: surface topography, sub-surface damage, and bulk defects[16]. AFM can help assess surface characteristics associated with polishing that may result in scattering loss. In this work, a pair of sapphire samples from each manufacturer were used for AFM characterization in their as-received conditions. All samples were ultrasonicated in an ethanol bath for 1 hour and subsequently ultrasonicated in an acetone bath for another 30 minutes before making AFM measurements. As shown in Fig. 3.3, both KO and GTAT samples have different levels of residual striations from polishing along with minor scratches; similarly, the Guild samples have a small number of digs and uniformly distributed impurity particles. Generally, it is assumed that samples with lower scratch/dig numbers should have higher quality surfaces compared to samples with higher numbers, but the AFM results presented here provide additional information that is important for assessing optical loss associated with scattering. For example, the KO 1 and GTAT 1 have the same 60/40 scratch/dig but the AFM image shows that the GTAT 1 sample appears to have a much smoother surface. This is somewhat understandable since the scratch/dig standard is subjective and is based on a visual comparison under specific darkfield lighting conditions which can be misleading in many cases [113]–[115]. Given the obvious discrepancies between the AFM images and scratch/dig assessments, other meaningful surface specifications should be considered when assessing optical scatter from surfaces.

Kienzle *et al.* derived an expression that relates the total front surface scattering loss, S, with the RMS surface roughness, σ_{rms}, assuming normal incidence:

$$S = R_{12}(\frac{4\pi}{\lambda}\sigma_{rms})^2 \tag{3.8}$$

where R_{12} is the Fresnel reflectance of the air-material interface and λ is the incident light wavelength[116]. Equation (3.8) indicates that the total surface scattering loss is proportional to the squared RMS surface roughness. However, the model assumes a reflective front surface with Gaussian surface height statistics and only considers the scattering due to this roughness. Surface imperfections such as scratches and digs, particulate, and streaks due to polishing were not included in the model and they could have a different relationship with the scattering loss [25], [117]. As the roughness measured for a surface is often decorated by those artifacts, Eq. (3.8) should be taken as a criterion for the minimum scattering loss due to roughness [25].

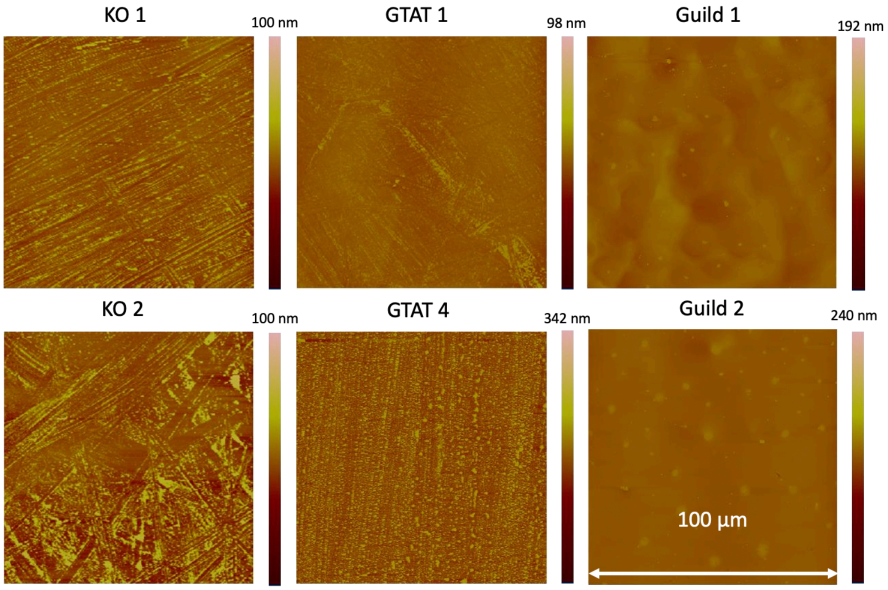

Figure 3.3. Two-dimensional surface topography images generated by AFM of three pairs of sapphire samples from each manufacturer. Note that vertical scales are different but each image has the same size of 100 µm x 100 µm. Various levels of striations and impurity particles are shown in different samples.

To estimate S for the sapphire samples, a two-dimensional power spectral density (PSD) analysis over a spatial frequency range from 0.5 to 1.2 μm^{-1} was performed on each AFM image shown in Fig. 3.3. A particular spatial frequency range was chosen to match with the main wavelength of interest, 1.064 μm. The PSD values were then converted to the equivalent RMS roughness values and they are listed in Table 3.2. Using these roughness values along with the Fresnel reflectance of sapphire, the computed surface scattering loss for each sample was obtained and the results are shown in Table 3.2. For most samples, the loss fraction is at the level of 0.001% to 0.1% which is relatively small suggesting that scatter associated with surface roughness is weak. However, Fig. 3.3 shows that GTAT 4 has a much rougher surface with many high frequency irregularities in the vertical direction possibly caused by the polishing. The AFM results indicate non-Gaussian surface height statistics for GTAT 4 while other samples appear to have well-conditioned statistics. Apparently, the surface of GTAT 4 does not follow the underlying assumptions for Eq. (3.8) such that its scattering loss due to the surface should differ from the predicted value. Note that the RMS values shown in Table 3.2 could be overestimated as the height contrast present in Fig. 3.3 might be partially due to the interactions between the AFM tip and potential energies associated with surface irregularities rather than the actual surface topography. Scatterance measurements were performed to assess whether or not surface scatter due to roughness was actually significant for the samples included in this study.

Table 3.2. RMS Roughness and Predicted Surface Scatterance of Sapphire Samples at 1064 nm

Sample	PSD Equivalent RMS Roughness (nm)	Total Scattering Loss for Single Surface
GTAT 1	2.76	0.00797%
GTAT 4	15.3	0.244%
Guild 1	2.17	0.00492%
Guild 2	2.75	0.00791%
KO 1	5.42	0.0307%
KO 2	6.99	0.0511%

3.3.1.2 BSPDF Results

BSPDF was used to measure optical scatterance of each thick and thin pair of samples which enabled a comparison between surface/sub-surface related and bulk related scattering losses. Figure 3.4 shows representative BSPDF results along with modeled fits for KO 1. The BSPDF values are plotted against the measurement angle (beam blockage by the detector occurs between -210° and -180°). Data collected within this range serve as a noise floor of the measurement and indicate that the measurement has a dynamic range of approximately eight orders of magnitude for the KO 1 sample. Measurements of other samples also indicated similar ranges. The data near -270°, -90° and 80° are influenced by scattering from the ground edge of the sample and are not indicative of material-related scatter. Based on photodetector specifications and laser power fluctuations, the maximum experimental uncertainty for measurements at other angles was less than 5%.

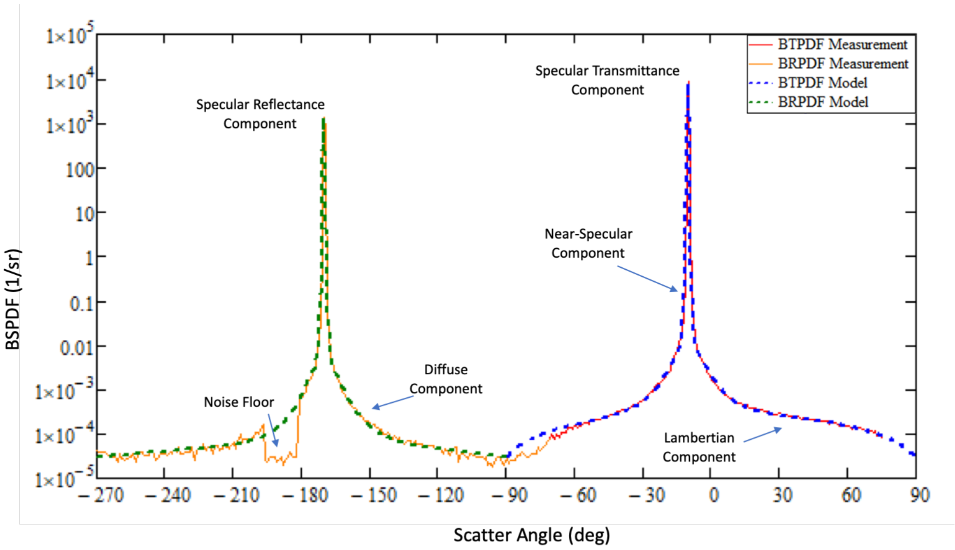

Figure 3.4. The BSPDF data of the KO 1 measured at 532 nm with a 10-degree incident angle. Both BTPDF and BRPDF models include all four components of the phase function and these are labeled in the illustration.

The phase function models for both BRPDF and BTPDF are indicated by the dashed line in Fig. 3.4 with different components of sample reflectance (ρ) and transmittance (τ) being labeled in different regions. The near-specular component mostly accounts for scattering due to surface roughness and sub-surface damage and does not scale with path length. The diffuse component is primarily related to the defects in the bulk and subsurface and has a stronger path length dependence. Defects, such as impurities, bubbles, and cracks, etc. could cause a local index of refraction change that leads to scattering losses at angles that are larger than the near-specular angles shown in Fig. 3.4. It is also responsible for scattering loss due to surface irregularities other than roughness. Moreover, the Lambertian component often relates to a random, weak diffuse scatterance due to trapped light caused by bulk defects with internal ray angles greater than the critical angle [111], [118]. The propagation path length of the light can become long in this case and this leads to multiple scattering along with a weak path length dependence. All three components from the phase models were used to calculate the final total scatterance α_{sca} for each sample. The sum of the total integrated reflectance ρ_{in} and transmittance τ_{in}, along with the total absorbance and scatterance, α_{abs} and α_{sca}, of each sample must be equal to one to satisfy the total power law equation:[110]

$$\rho_{\mathrm{in}} + \tau_{\mathrm{in}} + \alpha_{\mathrm{abs}} + \alpha_{\mathrm{sca}} = 1 \tag{3.9}$$

where

$$\alpha_{sca} = \rho_{\mathrm{ns}} + \tau_{\mathrm{ns}} + \rho_{\mathrm{L}} + \tau_{\mathrm{L}} + \rho_{\mathrm{diff}} + \tau_{\mathrm{diff}} \tag{3.10}$$

A summary of the scatterance results and the total power law check for the different samples is given in Table 3.3. For all bulk samples, the total powers were equal to or slightly less than unity indicating that the power law was satisfied. Similar checks were not available for the thin samples since the absorption of these samples was not measured. A Lambertian background which was measured to be $5\text{x}10^{-4}$ at all measured wavelengths could possibly exist in all measurements due to a reflected incident beam spot on the chamber wall, causing a small overestimation of the scatterance results in Table 3.3. Overall, all samples show a decreasing trend in scatterance as wavelength increases. In the region between 532 nm and 1064 nm, the scatterance loss in all samples is in the range of 0.1% to 0.6%. The scatterance can be as high as 1.2% at 405 nm and as low as 0.065% at 1550 nm for some samples. By examining the scatterances of each thick-and-thin pair from different manufacturers, the results imply that scatterance of KO 1 and Guild 1 are mainly related to the surface. For the GTAT samples, a useful conclusion regarding bulk versus surface scatter could not be made. However, by considering the scatterance level in other thin samples (i.e. KO 2 and Guild 2), it is possible that scatterances of both GTAT 1 and 3 are dominated by the bulk or surface irregularities (mostly due to diffuse scatterance) at 405 nm and 532 nm while GTAT 2 has loss that depends more on surface scatter at all wavelengths besides 405 nm. For the case of GTAT 4, although it has a relatively lower scatterance at all measured wavelengths among all thin samples, the analysis of its surface topography suggests the possibility that out-of-plane scatterance contributed to the results but this was not quantified in this study.

Comparisons of measured near-specular, scattering loss at different wavelengths between GTAT 1 and KO 1 indicate the relative contribution of surface roughness-related scatter. The latter sample has a slightly lower scattering loss (except at 405 nm) but has a rougher surface. GTAT 1 has relatively weak contributions from surface topography-related scattering loss compared to the total loss at all wavelengths while the surface-related scatterance appears stronger in KO 1. To put aspects of these results into context, Benabid *et al.* estimated that the theoretical intrinsic scattering loss of sapphire due to spatial fluctuations of permittivity should be 1.6 ppm/cm and 0.21 ppm/cm at 633 nm and 1064 nm respectively [82]. These values are much lower than the measured results reported in Table 3.3, and it is reasonable to believe that the scattering loss in the samples studied here are related to other extrinsic effects. For the samples in this study, scatterers related to sub-surface damage (including those observed surface irregularities which extended below the surface) and bulk defects must play an important role since both the near-specular and diffuse scatterance components are relatively large when compared to estimates of intrinsic scatter in these materials.

Table 3.3. Total Integrated Scatterance and Scatterance Components of As-Received Sapphire Samples

GTAT 1	**Near-Specular Scatterance**	**Total Lambertian and Diffuse Scatterance ($\alpha_{diff\ sca}$)**	**Total Scatterance (α_{sca})**	**Total Power Law Satisfaction**
Wavelength	$\rho_{ns} + \tau_{ns}$	$\rho_l+\tau_l+\rho_d+\tau_d$	$\rho_l+\tau_l+\rho_d+\tau_d + \rho_{ns} + \tau_{ns}$	$(\rho_{in} + \tau_{in} + \alpha_{abs} + \alpha_{sca})$
405 nm	0.0025	0.0091	0.012	0.9986
532 nm	0.0016	0.0045	0.0061	0.9998
633 nm	0.001	0.0027	0.0037	0.9999
1064nm	0.001	0.0020	0.0030	1.000
1550 nm	0.0006	0.0013	0.0019	0.9999
GTAT 2				
Wavelength	$\rho_{ns} + \tau_{ns}$	$\rho_l+\tau_l+\rho_d+\tau_d$	$\rho_l+\tau_l+\rho_d+\tau_d + \rho_{ns} + \tau_{ns}$	$(\rho_{in} + \tau_{in} + \alpha_{abs} + \alpha_{sca})$
405 nm	0.0014	0.0088	0.010	1.000
532 nm	0.0009	0.0025	0.0034	0.9999
633 nm	0.0006	0.0022	0.0028	0.9998
1064nm	0.0006	0.0013	0.0019	1.000
1550 nm	0.0005	0.0012	0.0017	1.000
GTAT 3				
Wavelength	$\rho_{ns} + \tau_{ns}$	$\rho_l+\tau_l+\rho_d+\tau_d$	$\rho_l+\tau_l+\rho_d+\tau_d + \rho_{ns} + \tau_{ns}$	$(\rho_{in} + \tau_{in} + \alpha_{abs} + \alpha_{sca})$
405 nm	0.003	0.0093	0.012	1.000
532 nm	0.0015	0.0046	0.0061	0.9992
633 nm	0.0011	0.0036	0.0047	0.9998
1064nm	0.001	0.0021	0.0031	1.000
1550 nm	0.0006	0.002	0.0026	1.000
GTAT 4				
Wavelength	$\rho_{ns} + \tau_{ns}$	$\rho_l+\tau_l+\rho_d+\tau_d$	$\rho_l+\tau_l+\rho_d+\tau_d + \rho_{ns} + \tau_{ns}$	$(\rho_{in} + \tau_{in} + \alpha_{abs} + \alpha_{sca})$
405 nm	0.0015	0.0014	0.0029	N/A
532 nm	0.0012	0.00093	0.0021	N/A
633 nm	0.0008	0.00091	0.0017	N/A
1064nm	0.0006	0.00081	0.0014	N/A
1550 nm	0.0000	0.00083	0.00083	N/A
KO 1				
Wavelength	$\rho_{ns} + \tau_{ns}$	$\rho_l+\tau_l+\rho_d+\tau_d$	$\rho_l+\tau_l+\rho_d+\tau_d + \rho_{ns} + \tau_{ns}$	$(\rho_{in} + \tau_{in} + \alpha_{abs} + \alpha_{sca})$

405 nm	0.004	0.0035	0.0075	0.9995
532 nm	0.001	0.0030	0.004	0.9999
633 nm	0.0009	0.0017	0.0026	0.9998
1064nm	0.0009	0.0016	0.0024	0.9997
1550 nm	0.0008	0.0013	0.0021	1.000
KO 2				
Wavelength	$\rho_{ns} + \tau_{ns}$	$\rho_l+\tau_l+\rho_d+\tau_d$	$\rho_l+\tau_l+\rho_d+\tau_d + \rho_{ns} + \tau_{ns}$	$(\rho_{in} + \tau_{in} + \alpha_{abs} + \alpha_{sca})$
405 nm	0.0018	0.0032	0.0049	N/A
532 nm	0.001	0.0014	0.0024	N/A
633 nm	0.0006	0.0013	0.0019	N/A
1064nm	0.0006	0.0012	0.0018	N/A
1550 nm	0.0005	0.0011	0.0016	N/A
Guild 1				
Wavelength	$\rho_{ns} + \tau_{ns}$	$\rho_l+\tau_l+\rho_d+\tau_d$	$\rho_l+\tau_l+\rho_d+\tau_d + \rho_{ns} + \tau_{ns}$	$(\rho_{in} + \tau_{in} + \alpha_{abs} + \alpha_{sca})$
405 nm	0.0023	0.0028	0.0051	0.9991
532 nm	0.0019	0.0019	0.0038	0.9990
633 nm	0.0009	0.0019	0.0028	0.9999
1064nm	0.0009	0.0014	0.0023	1.000
1550 nm	0.0007	0.001	0.0017	1.000
Guild 2				
Wavelength	$\rho_{ns} + \tau_{ns}$	$\rho_l+\tau_l+\rho_d+\tau_d$	$\rho_l+\tau_l+\rho_d+\tau_d + \rho_{ns} + \tau_{ns}$	$(\rho_{in} + \tau_{in} + \alpha_{abs} + \alpha_{sca})$
405 nm	0.0018	0.0016	0.0034	N/A
532 nm	0.0009	0.0016	0.0025	N/A
633 nm	0.0006	0.0015	0.0021	N/A
1064nm	0.0006	0.0012	0.0018	N/A
1550 nm	0.0004	0.0010	0.0014	N/A

From the entire crystal boule to each individual window disk, sapphire samples typically experience post-growth processing such as grinding, lapping and polishing that disturb both the surface and the sub-surface of the material. Among these mechanical treatments, polishing is known as the most important step since it is the last process that removes microcracks induced during lapping and is meant to produce a near-perfect surface. All samples used in this work were polished using a combination of chemical and mechanical methods that require application of mechanical force in the presence of chemical solutions to achieve material removal. Even though a damaged layer associated with lapping is removed during polishing, polishing itself can produce a near-surface layer containing an elevated concentration of dislocations, point defects, impurities, and residual stresses that is typically referred to as the Beilby layer [16], [97], [119], [120]. Finch reported the discovery of a crystalline Beilby layer in sapphire in the late 1930s and its layer thickness is typically from a few nanometers to a micrometer [121]. Later, Dobrovinskaya *et al.* also confirmed the existence of the surface layer in sapphire using electron diffraction analyses[16].

According to different studies on mechanically-treated sapphire, the Beilby layer in sapphire can extend to 2 mm below the surface [16],[98]. However, the Beilby layer itself is highly heterogenous and can be divided into several zones. For example, within the depth of 1 to 10 nanometers below the surface, the layer can be either polycrystalline or amorphous. Impurity particles from the polishing slurry have been found to reside in this zone in polished fused silica [97]. At a depth about 1.5 to 2 μm, the layer can be textured polycrystalline or single crystal with block disorientation angles of a few degrees. Further from the surface, at about 50 μm, the layer is single crystal with increased concentrations of vacancies and dislocations. Finally, between 1 mm to 2 mm below the surface, residual stresses are present and serve to alter the physical properties relative to the bulk [16]. Index mismatch resulting from all of these contribute to optical scattering [16],[82] and must be taken into account. By changing polishing parameters such as abrasive size, applied force, and rotation speed, the Beilby layer can be altered [16], [122]. In recent years, a process known as superpolishing has been introduced for preparation of sapphire surfaces, and this process can achieve a surface RMS roughness of less than 1 nm with the complete elimination of surface cracks and scratches to a depth about 5 nm below the sample surface [123], [124]. While superpolished sapphire samples have a nearly defect-free surface, the character of deeper regions in the Beilby layer remains relatively unknown. It is important to know if this type of polishing technique is able to minimize the Beilby layer thickness and reduce sub-surface-related scatterance.

Additional investigation into the relationship between surface treatments and sub-surface related optical scatterance is needed to better understand the efficacy of different polishing procedures.

3.3.1.3 Single Scatter Analysis

In all sapphire samples used in this work, single scattering events dominate since the total scatterance of each sapphire is less than 0.1[11]. Single scattering occurs when the incident light is scattered by a single particle or a particle-like defect, whereas multiple scattering happens when the light interacts with multiple particles. For the purposes of this work, both types of scattering can be taken into account using the following expression for the total integrated scatterance, $\alpha_{scatterance}^{TIS}$, as a function of thickness, d: [118]

$$\alpha_{scatterance}^{TIS}(d) = \beta_{single\ scatterance} \cdot d + \alpha_{surface} + \alpha_{diffuse} \tag{3.11}$$

where $\beta_{single\ scatterance}$ is the bulk single-scatter coefficient, $\alpha_{surface}$ is the surface scatterance, and $\alpha_{\ diffuse}$ is the diffuse scatterance that has weak (or no) path length dependence. The diffuse scatterance is mainly caused by multiple scattering centers and has been observed to vary slowly with the thickness. Its value is typically low (on the order of 10^{-4} or less) based on previous works and it can be assumed to be thickness independent in this work [110], [118]. The $\beta_{single\ scatterance}$ term describes scattering by bulk defects and is evaluated per unit length. Therefore, the total scatterance of each sapphire sample was hypothesized to be related to bulk and surface single-scatterers.

A simple, frequency-dependent model based on Mie theory can be used to compute the total scatterance and bulk single-scatter coefficient as well as provide insight into the effects of particle size distributions. Mie scattering describes a general solution to Maxwell's equations for spherical particles of arbitrary size and refractive index[11]. However, this model is often applied to nonspherical particles because they are often randomly oriented in the material and, as a result, can display scattering properties that are similar to those for spherical particles [11]. Using Mie theory, a general formula for the scattering coefficient as a function of wavelength can be expressed as follows: [11]

$$\beta_{single\ sca}(k') = \int_0^{\infty} \pi r^2 Q_{sca}(k'r)\rho_p(r)dr \tag{3.12}$$

where β_{sca} is the single-scatter scattering coefficient, $k' = \frac{2\pi n}{\lambda}$ depends on the wavelength, λ, and the refractive index of the scattering particle, n, r is the scattering particle radius, Q_{sca} is the scattering efficiency coefficient, and ρ_p is the particle size distribution function. By splitting the integral in Eq. (3.12) into two parts – one related to small particles and the other to large particles – a simple, approximate expression for the scattering coefficient can be obtained. This approach employs the following form for Q_{sca}:

$$Q_{sca}(k'r) = \begin{cases} A'k'^4r^4 & k'r \ll 1 \\ 2 & k'r > 1 \end{cases} \tag{3.13}$$

where *A'* is a constant. When the value of $k'r$ is very small, the scattering coefficient corresponds to the Rayleigh limit and displays a λ^{-4} functional dependence. When the particle radius becomes larger than the wavelength, the scattering efficiency fluctuates about and ultimately approaches a mean value of 2 [11]. Using these different Q_{sca} with Eq. (3.13), the scattering coefficient for these two regimes can be expressed as follows:

$$\beta_{single\ sca\ 1}(k') = \int_0^{r_0} \pi r^2 A'k'^4r^4\rho_p(r)dr \qquad k'r \ll 1 \tag{3.14}$$

and

$$\beta_{single\ sca\ 2}(k') = \int_{\frac{1}{k'}}^{\infty} \pi r^2 2B'r^{-m}dr \qquad k'r \gg 1 \tag{3.15}$$

where $r_0 << \frac{1}{k'}$, *B'* and *m* are constants. According to Eq. (3.13), when the particle radius is smaller than the wavelength, the scattering coefficient has a strong particle size dependence. As the particle becomes much larger than the wavelength, the scattering coefficient basically depends on the cross-sectional area of the particle and has a weaker particle size dependence that occurs in the Rayleigh regime. This concept is illustrated in Fig. 3.5. where Q_{sca} of a chromium-related impurity in sapphire is plotted against the diffraction parameter x ($x=\frac{2\pi r}{\lambda}$). Even if the form of $\rho_p(r)$ is not known, the wavelength dependence of the scattering coefficient in Eq. (3.12) can be expressed as follows using Eq. (14):

$$\beta_{single\ sca\ 1}(k') = Ak'^4 \tag{3.16}$$

Similarly, Eq. (3.17) can provide a wavelength dependence for larger scatterers that has the following form:

$$\beta_{single\ sca\ 2}(k') = Bk'^p \tag{3.17}$$

where p is a constant. Since k' is directly proportional to the frequency, ν, the total single-scatter coefficient $\beta_{sca}\ (\nu)$ can be approximated using the following:

$$\beta_{\mathrm{single\ sca}}\ (\nu) = \mathrm{A}\nu^4 + \mathrm{B}\nu^{\mathrm{p}} \tag{3.18}$$

Equation (3.18) serves as a simple model for predicting the single-scatter coefficient where the fitting parameters A and B are related to the concentrations of particles in the two scattering regimes and the constant p is related to the size distribution of larger particles. This approach provides a relatively simple expression that can be used to interpret aspects of scattering in the medium.

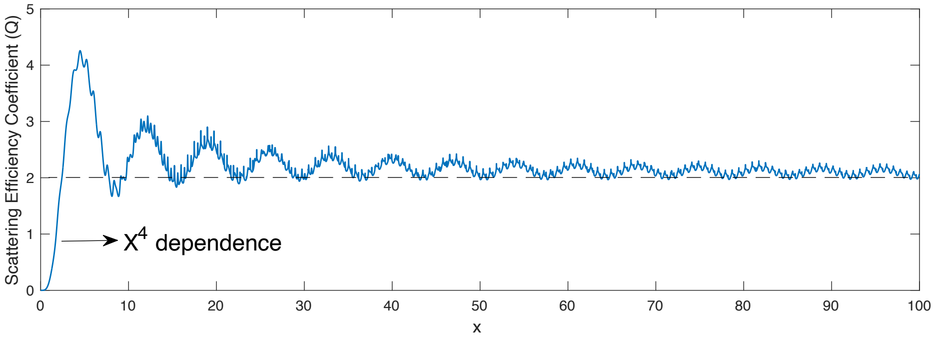

Figure 3.5. Scattering efficiency coefficient, Q_{sca}, as a function of the diffraction parameter, $x=\frac{2\pi r}{\lambda}$, at 1064 nm for a chromium-related impurity in sapphire. As x approaches large values, the large oscillation of Q_{sca} damps to a finite value and the particle size dependence becomes weaker.

The single-scatter model was fit to the total scatterance of GTAT 1, KO 1, and Guild 1 (using the thickness of each sample) from Table 3.3 and the results are shown in Fig. 3.6. Trends present in the data can be explained fairly well with this model and some indication of the relative scatterer size distributions among the samples can be obtained by considering the fitting parameters that are provided in Table 3.4. As Table 3.4 shows, the concentration of larger particles in KO 1 is higher compared to those in GTAT 1 and Guild 1. Furthermore, a small p-value for KO sapphire indicates that particle size distribution for the larger particles is relatively broad. Guild 1 had an overall low concentration of scatterers with different sizes among all three samples.

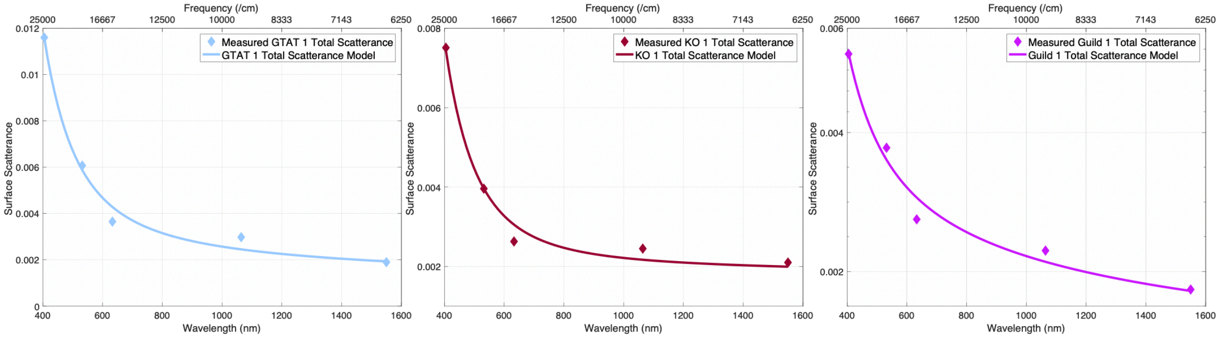

Figure 3.6. Total scatterance of GTAT 1, KO 1 and Guild 1 are shown in blue, brown and pink diamonds, respectively. The single-scatter model (Eq. 19) of each type are displayed as blue, brown, and pink solid lines, correspondingly. Model parameters are listed in Table 3.4.

Table 3.4. Fitting Coefficients for the Single-Scatter Model (Total Scatterance Case)

Sample	A (cm^3)	B (cm^{1-p})	p
GTAT 1	2.11×10^{-20}	2.36×10^{-5}	0.5
KO 1	1.38×10^{-20}	6.87×10^{-4}	0.12
Guild 1	4.19×10^{-21}	1.37×10^{-5}	0.55

On the other hand, using the TIS values for each pair of thick and thin samples from KO and Guild with Eq. (3.11), the bulk single-scatter coefficient along with the surface and the diffuse scatterance were determined. Results are given in Table 3.5. For both KO and Guild samples, results show that the surface-related scatterance was important. Note that the bulk scattering estimated using this method only provided an estimate as the scattering behavior could vary locally depending on the surface conditions. Similarly, the single-scatter model shown from Eq. (3.18) could also be used to fit the calculated bulk single-scatter coefficients from Table 3.5. and the results are exhibited in Fig. 3.7. Additionally, the fitting parameters are shown in Table 3.6 and the results indicate that the concentrations of both smaller and larger particles in bulk KO sapphire are higher compared to those in bulk Guild sapphire.

Table 3.5. Bulk, Single-Scatter Coefficients, Surface Scatterance and Diffuse Scatterance

	$\beta_{\text{single sca}}$ (cm^{-1})		$\alpha_{\text{surface sca}} + \alpha_{\text{diffuse sca}}$	
Wavelength	KO	Guild	KO	Guild
405 nm	0.0030	0.0019	0.0046	0.0032
532 nm	0.0018	0.0014	0.0022	0.0024
633 nm	0.00085	0.00076	0.0018	0.0020
1064 nm	0.00075	0.00051	0.0017	0.0018
1550 nm	0.00052	0.00034	0.0015	0.0014

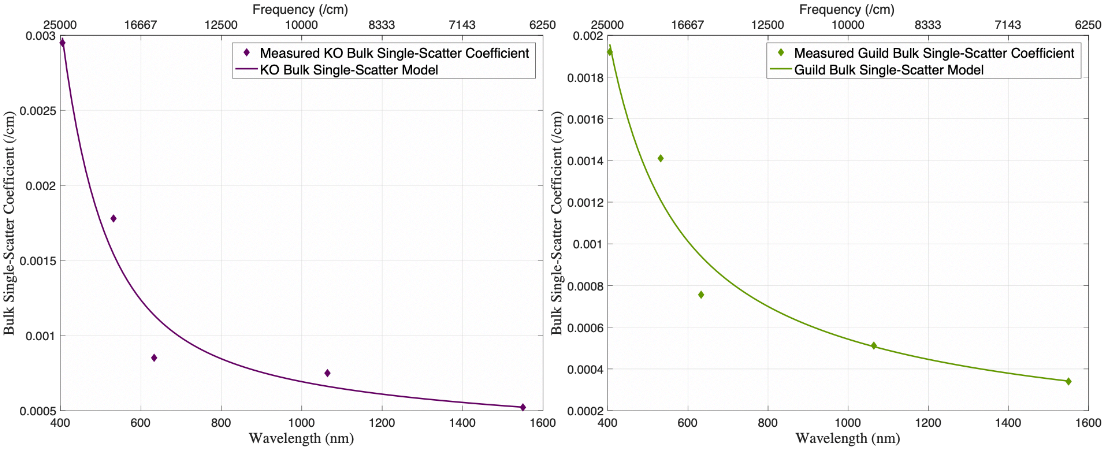

Figure 3.7. Calculated bulk single-scatter coefficients of KO sapphire and Guild Sapphire are shown in blue asterisks, purple diamonds, and green stars, respectively. The bulk single-scatter model (Eq. 19) of each type are displayed as blue, purple, and green solid lines, correspondingly. Model parameters are listed in Table 3.6.

Table 3.6. Fitting Coefficients for the Bulk Single-Scatter Model

Sample	A (cm^3)	B (cm^{1-p})	p
KO Sapphire	5.32 x 10^{-21}	6.40 x10^{-6}	0.5
Guild Sapphire	1.78 x 10^{-21}	5.25 x10^{-8}	1

3.3.2 Polished Sapphire Samples

3.3.2.1 Surface Evaluation by Optical Microscopy and AFM

Representative optical micrographs of super-polished GTAT 1 and KO 2 are shown in Fig.3.8 to reveal any surface artifacts from the polishing process. Polishing streaks as well as embedded impurity particles and digs have been observed from samples' surfaces. According to Fig. 3.8, the size of these defect features extends from sub micrometers to a few micrometers. Similarly, the AFM scans of three extra-polished samples also reveal their surface characteristics as can be seen Figure 3.9 a, d and g are AFM images of each sample in the as-received condition while the remaining images were obtained after the extra polishing process. The equivalent RMS roughnesses converted from the two-dimensional PSD analysis (over a spatial frequency range from 0.5 to 1.2 μm^{-1}) are also shown on the upper right corner in each figure. According to

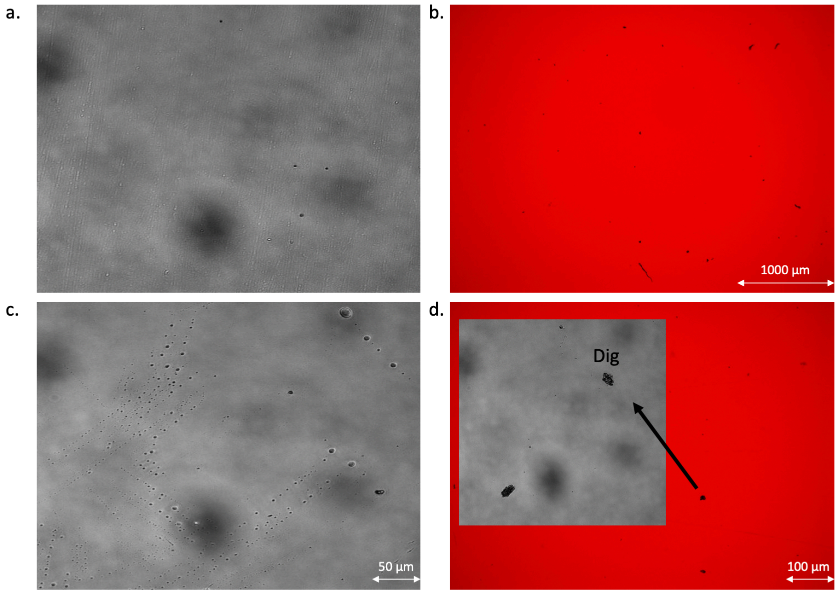

Figure 3.8. Confocal micrographs of further polished GTAT 1 and KO 2 are shown in (a) and (c) while stereo micrographs of the two samples are shown in (b) and (d). In (d), a zoomed confocal micrograph of a dig feature on KO 2 is presented.

Fig. 3.9, extra-polished samples show fewer residual striations, minor scratches, and surface impurities. The RMS roughness values of extra-polished samples are also reduced except for GTAT 1 that had roughness that was slightly increased after an extra polish. This increased roughness is believed to be associated with the morphology change of polishing-induced surface artifacts that are inhomogeneously distributed across the sample surface. Indeed, as is indicated by images in Fig. 3.9 for samples after they were super-polished, a small degree of surface inhomogeneity was observed on all samples. Some areas show a perfectly smooth topography whereas other areas are decorated with polishing artifacts. Similar inhomogeneity was also observed from the optical micrographs which were taken at a much larger scale. We will show shortly that localized inhomogeneity may result in different BSPDF values measured from different locations.

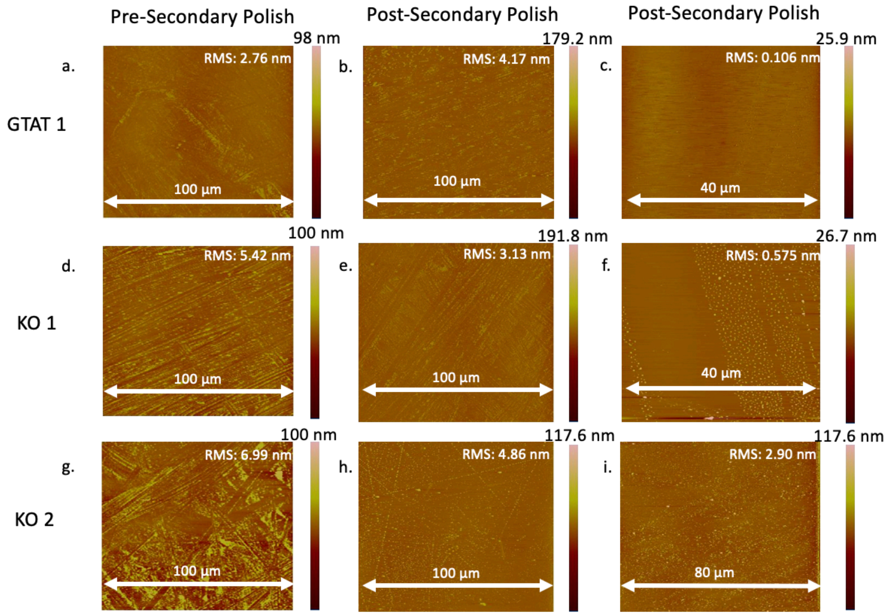

Figure 3.9. Two-dimensional surface topography images generated by AFM with a scan size of 100 µm x 100 µm of as-received GTAT1, KO1, and KO2 are shown in (a),(d),(g). AFM images of extra-polished GTAT 1, KO 1, and KO 2 taken at 100 µm x 100 µm are shown in (b), (e), (h) and those scanned at 40 µm x 40 µm and 80 µm x 80 µm are shown in (c), (f), (i). The RMS roughness associated with each image is labeled.

3.3.2.3 BSPDF Results

The BSPDF measurements were performed on three extra-polished samples following the same procedure as in Section 3.3.1.2 (at 532 nm, 633 nm, 1064 nm, and 1550 nm). For GTAT 1 and KO 2, five to seven measurements were taken from different locations and orientations on each sample to obtain a statistical representation of the scattering loss. Representative images of BRPDF and BTPDF of all as-received samples and extra-polished samples are shown in Fig. 3.10. The top obtained from the same samples after being extra-polished. Overall, all three samples showed a reduced scatterance in both forward and backward directions with the diffuse component being decreased the most. Since the diffuse scattering is partially due to sample surface conditions, the reduction is likely to be related with the decreased surface defects resulted from the extra polishing. A summary of the scatterance results is shown in Table 3.7. Overall, all samples had a scatterance level of 10^{-4} at 1064 nm. Compared to the pre-polished total scatterance of each sample in Table 3.3, the total scatterance of each sample after the secondary polishing process shows a reduction, suggesting an improved scratch/dig specification and a locally reduced number of surface imperfections. However, for GTAT 1 and KO 2, the standard deviation of the measured scatterance at each wavelength was large because some regions on the sample surface scattered more compared to others. This is also demonstrated in the previous AFM images and optical micrographs of all samples as some surface regions show a higher number of defects compared to others. Although multiple measurements of KO 1 could not be done, it is possible that the sample has similar scatterance statistics to those of GTAT 1 and KO 2.

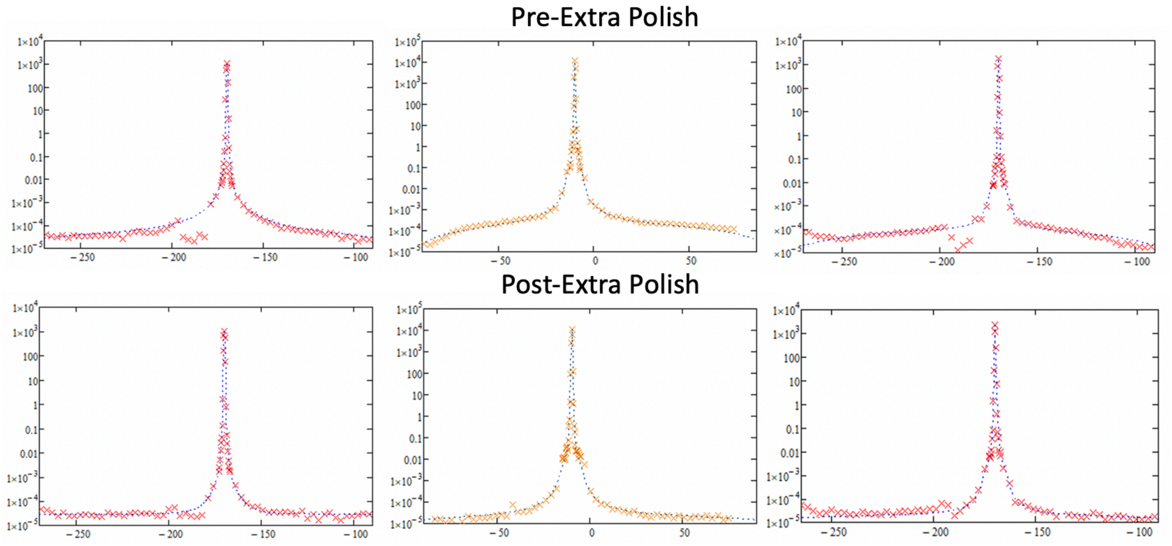

KO Thick @ 532 nm GTAT 1064 @ 1064 nm KO Thin @ 1064 nm

Figure 3.10. BSPDF and BTPDF obtained from KO 1, GTAT 1, and KO 2 under as received and further polished conditions at different wavelengths are shown in the upper row and lower row, respectively.

Results also indicate that the thin sample (KO 2) scatterance is comparable to that of the thick samples (GTAT 1 and KO 2) suggesting the scattering loss is mainly dominated by the surface. Subtracting thin sample scatterance from the thick samples' reveals that the scatterance contributed from the bulk was 10^{-4} to 10^{-3} at 532 nm and 633 nm, and 10^{-5} to 10^{-4} at 1064 nm and 1550 nm. Benabid *et al.* have developed a formula to calculate the scattering coefficient due to individual point defects:

$$\beta_{\mathrm{sca}}(\lambda) = \sigma_{\mathrm{sca}} n_{\mathrm{def}} \left(\frac{633\ \mathrm{nm}}{\lambda}\right)^4 \tag{3.19}$$

where σ_{sca} is the scattering cross section in cm^{-2} and take a value between 10^{-27} and $10^{-26}/\mathrm{cm}^2$ at the wavelength of 633 nm depending on the defect nature, n_{def} represents the point defect concentration, and λ is the incident wavelength [82]. Laser window grade sapphire typically has a total point defect concentration (impurity plus vacancy) at a level of 100 ppm which is equivalent to a number density defect concentration of $\sim 10^{19}\ /\mathrm{cm}^3$. Applying this value to Eq. (3.19), the estimated scattering loss due to point defects is about 0.01 to 0.1 ppm/cm. Note that Eq. (3.19) only provides an estimate as the accurate prediction requires a known scattering cross section of a specific defect, which is often difficult to obtain. If point defects in the bulk produce only scattering losses of 10^{-7} to 10^{-6}, then other structural defects must be responsible for the remaining loss. Indeed, in Section 3.3.1.2, dislocations, residual stress, block misorientations, and planar defects were discussed since these are commonly found near the surface of polished sapphire samples [98]. Furthermore, these defects could also extend into the bulk because they arise during crystal growth and subsequent mechanical treatments, thus producing scattering loss from the bulk.

Table 3.7. Total Integrated Scatterance and Scatterance Components of Further Polished Sapphire Samples

GTAT 1	**Near-Specular Scatterance**	**Total Lambertian and Diffuse Scatterance ($\alpha_{diff\ sca}$)**	**Total Scatterance (α_{sca})**	**Transmittance + Reflectance**
Wavelength	$\rho_{ns} + \tau_{ns}$	$\rho_l+\tau_l+\rho_d+\tau_d$	$\rho_l+\tau_l+\rho_d+\tau_d + \rho_{ns} + \tau_{ns}$	$\rho_{in} + \tau_{in}$
532 nm	0.00028±0.00042	0.0007±0.00037	0.00098±0.00072	0.996±0.0019
633 nm	0.00017±0.00033	0.00055±0.00045	0.00072±0.00069	0.997±0.0015
1064nm	0.00015±0.00015	0.00035±0.00015	0.00049±0.000055	0.997±0.00069
1550 nm	0.000029±0.000045	0.00021±0.000092	0.00024±0.000088	0.998±0.0013
KO 1				
Wavelength	$\rho_{ns} + \tau_{ns}$	$\rho_l+\tau_l+\rho_d+\tau_d$	$\rho_l+\tau_l+\rho_d+\tau_d + \rho_{ns} + \tau_{ns}$	$\rho_{in} + \tau_{in}$
532 nm	0.000/0.0002	0.00055/0.00041	0.00055/0.00061	0.992/0.993
633 nm	0.00005	0.00045	0.0005	0.997
1064nm	0.0001	0.00035	0.00045	0.997
1550 nm	0.000	0.0002	0.0002	0.998
KO 2				
Wavelength	$\rho_{ns} + \tau_{ns}$	$\rho_l+\tau_l+\rho_d+\tau_d$	$\rho_l+\tau_l+\rho_d+\tau_d + \rho_{ns} + \tau_{ns}$	$\rho_{in} + \tau_{in}$
532 nm	0.0001±0.00015	0.0004±0.00013	0.0005±0.00023	0.993±0.0065
633 nm	0.00011±0.000088	0.00037±0.00024	0.00048±0.00026	0.994±0.0029
1064nm	0.00013±0.00013	0.00026±0.00015	0.00039±0.00022	0.998±0.00083
1550 nm	0.000042±0.000073	0.00015±0.000071	0.00019±0.00014	0.998±0.0019

The single-scatter model from Eq. 3.18 was applied to fit the total scatterance of each extra-polished sample in Table 3.7 and the results are shown in Fig. 3.11. The fitting parameters are shown in Table 3.8 to provide some indication of the relative scatterer size distributions in these samples. The thickness of KO 2 was treated as a unity as its scatterance at each wavelength was comparable to that of thick samples. For both GTAT 1 and KO 1, parameters A and B decreased which corresponds to a reduced number density of both small and large scatterers after polishing. Furthermore, a larger p value for both samples indicated a narrower particle size distribution for large particles.

Although a secondary polishing improved samples' surfaces by reducing the number and size of scratches and digs as well as polishing artifacts, the process could not completely eliminate defects at and below the surface. As seen from both optical micrographs and AFM images, the surfaces

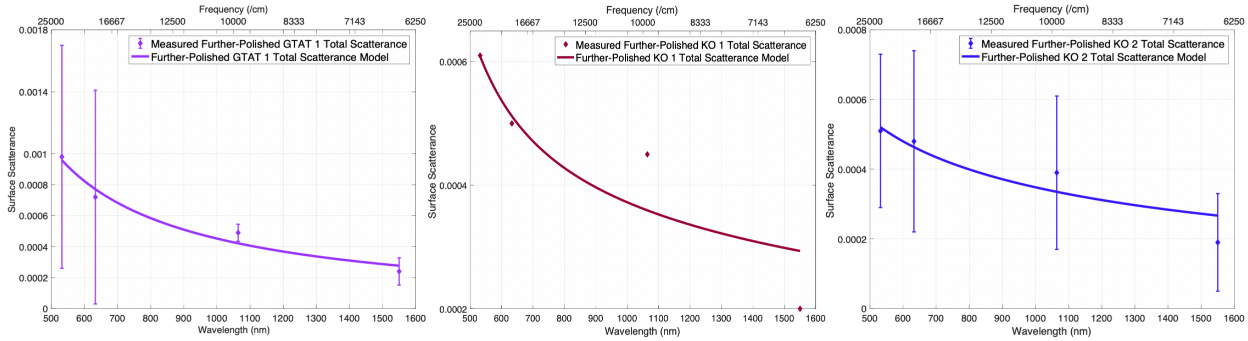

Figure 3.11. Total scatterance of extra- polished GTAT 1, KO 1 and KO 2 are shown in purple, brown and blue diamonds, respectively. The single-scatter model (Eq. 3.18) of each type are displayed as purple, brown, and blue solid lines, correspondingly. Model parameters are listed in Table 3.8.

Table 3.8. Fitting Coefficients for the Single-Scatter Model for the Measured Total Scatterance of Extra-Polished Sapphire Samples

Sample	*A* (cm^3)	*B* (cm^{1-p})	P
GTAT 1 (polished)	5.03 x 10^{-22}	1.79 x10^{-8}	1.1
KO 1 (polished)	8.81 x 10^{-22}	3.63 x10^{-6}	0.5
KO 2 (polished)	1.12 x 10^{-22}	1.38 x10^{-6}	0.65

still had different types of polishing artifacts with various sizes. The measured scatterance at each wavelength of each sample suggested that the extrinsic scattering losses still exist at a reduced level. Large scale structural defects (i.e. planar defects, dislocations, residual stress) are believed to mainly cause the bulk scattering because point defects have a relatively small scattering cross section. Along with these types of defects, polishing induced striations, impurities, and minor scratches together contributed to the surface scatterance, and the total scattering loss of these sapphire samples was dominated by surface defects. To improve the finish of sapphire window materials, surface treatments and growth parameters should be further investigated to reduce the levels of defects identified in this work.

3.3.3 Spinel Samples

3.3.3.1 Surface Evaluation by Optical Microscopy and AFM

Micrographs of the spinel sample surfaces were obtained using both stereo and confocal microscopy to examine surface defects at various scales, see Fig. 3.12. Similar to sapphire samples, scratches, digs, impurities, and polishing striations were observed on different spinel surfaces. The AFM images were acquired on selected spinel samples and the results are shown in Fig 3.13. In Fig. 3.13, the grain structure of each sample is clear, and impurity particles along with thin scratches are also on the sample surfaces. Note that although the color contrast in the AFM images appears to be associated with the height, this is unlikely since the surface topography probably does not follow grain structure. Previous works suggested that the step height should not exceed 2 to 3 nm [53]. Therefore, the contrast could originate from the interactions between the AFM tip and the potential energies associated with different grains and their chemistries. For samples obtained from Cera Nova, the roughness was measured to be in the range of 3 to 5 nm using a Zygo surface profilometer.

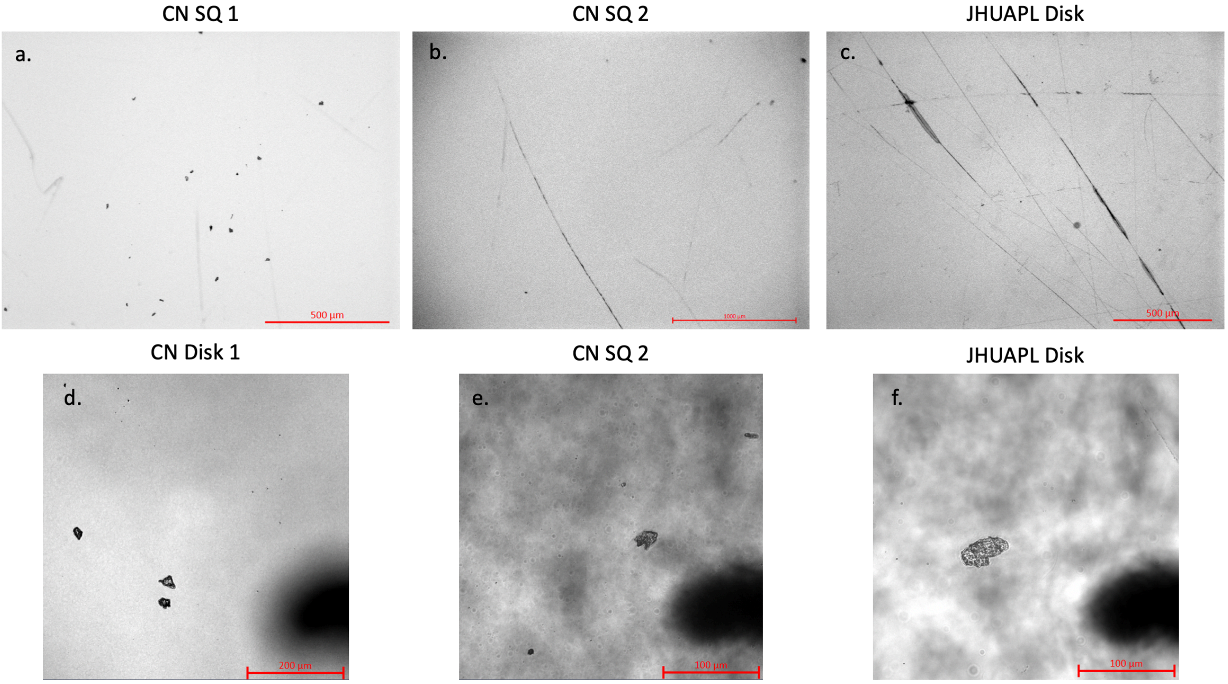
CN SQ 1
CN SQ 2
JHUAPL Disk
CN Disk 1
CN SQ 2
JHUAPL Disk

Figure 3.12. Stereo micrographs of surfaces of CN SQ 1, CN SQ 2, and JHUAPL Disk are shown in (a)-(c) and confocal micrographs of surfaces of CN Disk 1, CN SQ 2, and JHUAPL Disk are shown in (d)-(f)

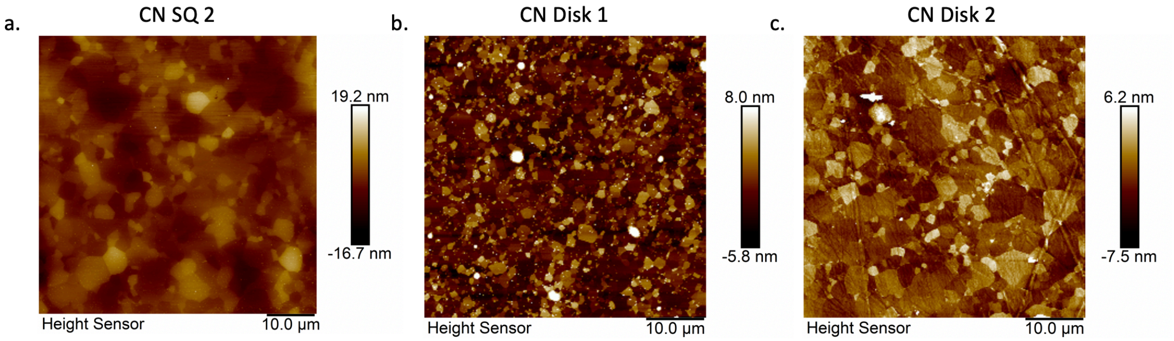

Figure 3.13. Two-dimensional surface topography images generated by AFM of CN SQ 2, CN Disk 1, and CN Disk 2 using a scanning size of 50 µm x 50 µm. Individual grains along with Various levels of striations and impurity particles are shown in different samples.

The spinel samples studied in this work are polycrystalline, and it is important to examine the grain size of each sample since the associated grain boundaries play an important role in scattering. The grain structure was imaged using a scanning electron microscope (SEM) with a BSE detector. The mean grain sizes of CN Disk 1, CN SQ 2, and JHUAPL Disk are reported in Table 3.9 and representative images are shown in Fig. 3.14. The grain size difference between CN Disk 1 and CN SQ 2 suggested that different sintering parameters and annealing treatments were used. Note that CN SQ 1 and 2 should have a comparable grain sizes because both samples were manufactured at the same time.

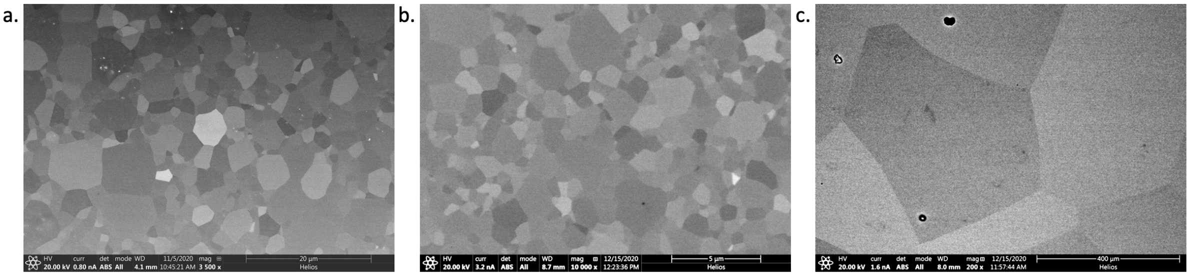

Figure 3.14 Representative SEM micrographs of CN SQ 2, CN Disk 1, and JHUAPL Disk shown in the left, middle, and right, respectively. These images were used to extract the grain size information.

Table 3.9. Average Grain Size of Selected Spinel Samples

Sample	Grain Size (μm)
CN Disk 1	0.922±0.425
CN SQ 2	2.66±1.48
JHUAPL Disk	429±171

3.3.3.2 Spinel BSPDF

The BSPDF measurements were performed on all spinel samples following the same procedure used in Section 3.3.1.2 at 532 nm, 633 nm, 1064 nm, and 1550 nm. Two measurements were performed on most samples at 532 nm, 1064 nm, and 1550 nm with the second measurement taken on the sample that was rotated by 90° about the surface normal axis relative to its original position. Figure 3.15 shows representative BSPDF results in solid lines along with modeled fits in dotted lines for CN Disk 1 at 532 nm. These results show that the CN Disk 1 has a much higher diffuse and Lambertian scatterance compared to those of different sapphire samples measured at the same wavelength. A summary of the scatterance results for different spinel samples is given in Table 3.10. The diffuse scattering coefficient was calculated using the total diffuse scatterance (diffuse + Lambertian components) divided by the sample thickness. Results in Table 3.10 indicate that the scattering loss of CN spinel samples is dominated by the bulk and that the scatterance of CN Disk 2 is five to ten times less than the other thick samples. Furthermore, CN Disk 2 had a scattering loss at 532 nm that was higher than at 1064 nm by a factor of 15, signifying a large number of small particles (i.e. sizes comparable to the visible wavelength) present in the sample. The reduction of the scattering loss of JHUAPL Disk moving from the visible to near-IR wavelength region was small compared to other CN samples, indicating more large features contributing to the loss of the sample. In addition, while CN Disk 1 has a relatively smaller grain size compared to these of CN SQ 1 and 2, it also scatters more at 532 nm and 633 nm based on the diffuse scatter coefficient, which corresponds to an increase of number of scatterers per unit volume. When moving to longer wavelengths, the total scatterance of CN Disk 1 is lower than those of CN SQ 1 and CN SQ 2 suggesting more of the scatterers in CN Disk 1 are under 1 μm in size. Overall, JHUAPL Disk has the lowest scatterance

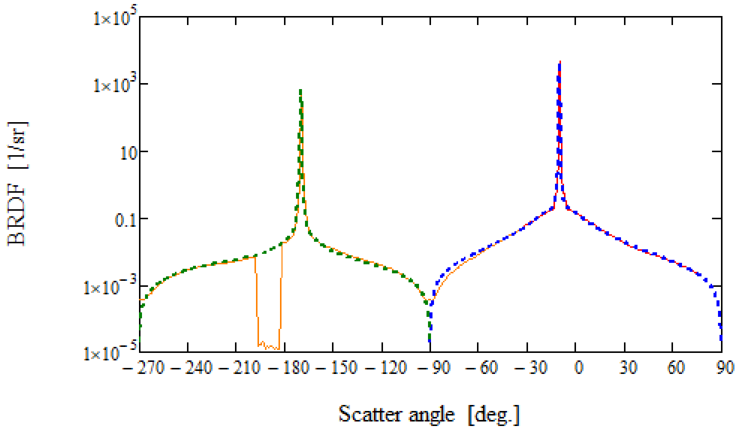

Figure 3.15. The BSPDF data of CN Disk 1 measured at 532 nm with a 10-degree incident angle.

at each wavelength owning to its much larger grain size which leads to fewer boundaries per unit length along propagation paths. Finally, CN SQ 2 has a scatterance that is small compared to that of CN SQ 1 at all wavelengths due to a secondary polishing treatment but the difference was trivial. Also, the fact that CN SQ 2 has a larger near-specular component while CN SQ 1 has a larger diffuse component indicates the secondary polish introduced some modifications to the surface. Indeed, one possible modification could be the particle-like features observed on CN SQ 2 surface as shown in Fig. 3.16. They were not observed on the CN SQ 1 surface. Figure 3.16 shows that these features have sizes from submicron to a few microns and are likely from the polishing solution. Raman spectroscopy was used to study the chemistry associated with these features and the results will be presented in Chapter 4.

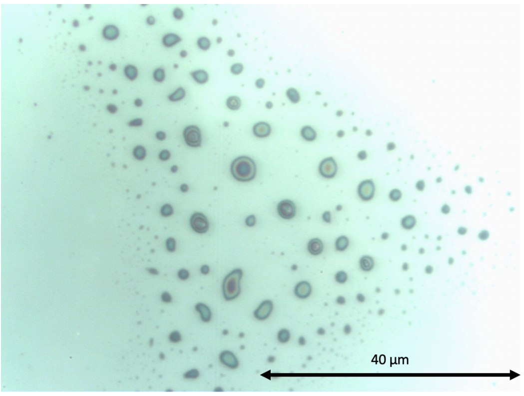

Figure 3.16. A confocal micrograph of CN SQ 2 surface showing impurity particles introduced by a secondary polishing process.

In polycrystalline transparent window materials, optical scattering occurs due to grain to grain index variations, pores, and residual impurities trapped at the grain boundaries [53], [59], [102], [104], [110]. Especially for spinel materials, stoichiometry has been found difficult to maintain near the grain boundaries due to excess raw starting compounds (primarily MgO and Al_2O_3) in addition to the problems caused by excessive impurities and point defects in the same region [40], [52], [53], [125]. Therefore, sintering aids such as LiF has been commonly used to produce fully dense transparent spinel as well as to clean the grain boundaries by reacting with certain impurities [51], [106]. According to Rothman et al., spinel samples fabricated without the addition of LiF tend to display a milky discoloration and the degree of such discoloration also depends on the fraction of grain boundaries that contribute to scattering [51]. Indeed, samples received from Cera Nova in this study were produced without any sintering agents and they possessed a milky discoloration as can be seen in Fig. 3.18. Furthermore, previous studies by Kim et al. showed that the typical spinel commercial powder contains 100 ppm levels of trace impurities such as S, Ca, and Si [32], [126]. They also demonstrated that spinel grown with lightly contaminated powder appeared to be hazy and milky. By using a small amount of LiF in the starting material, a lower absorption loss can be achieved since LiF react with the impurity elements during the stirring/evaporation process; the resulting spinel had a clear appearance. Therefore, according to

Fig. 3.18, JHUAPL Disk exhibits no discoloration suggesting that in addition to its large grain size, sintering aids could have been used during growth. Thus, the large diffuse scattering observed in CN samples might relate to grain boundaries coated with impurities that acted as scattering centers.

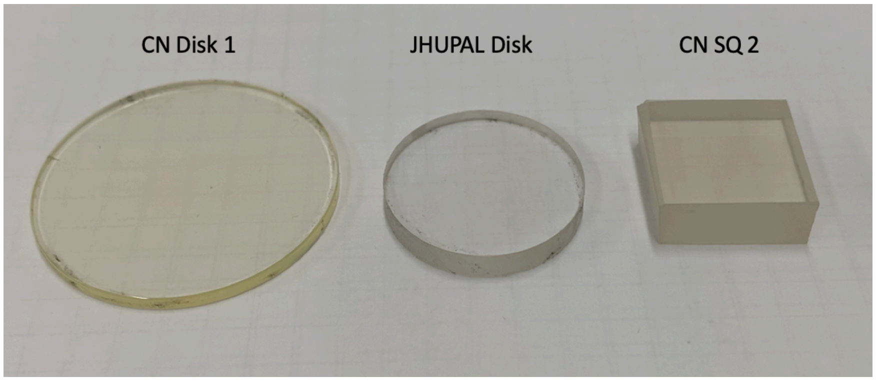

Figure 3.18. A picture of three spinel samples used in this study, showing a variation in the physical appearance among samples that were manufactured with or without a sintering aid.

Table 3.10. Total Integrated Scatterance and Scatterance Components of Spinel Samples

CN Disk 1	**Near-Specular Scatterance**	**Total Lambertian and Diffuse Scatterance** ($\alpha_{diff\ sca}$)	**Total Scatterance** (α_{sca})	**Reflectance + Transmittance**	**Diffuse Scattering Coefficient** ($\beta_{diff\ sca}$) **1/cm**
Wavelength	$\rho_{ns}+\tau_{ns}$	$\rho_l+\tau_l+\rho_d+\tau_d$	$\rho_l+\tau_l+\rho_d+\tau_d+\rho_{ns}+\tau_{ns}$	$\rho_{in}+\tau_{in}$	$\frac{\alpha_{diff\ sca}}{t}$
532 nm	0.0005/0.0004	0.059/0.056	0.06/0.056	0.92/0.935	0.273
633 nm	0.0006	0.0369	0.038	0.961	0.181
1064nm	0.0009/0.001	0.0099/0.0092	0.01/0.01	0.989/0.99	0.049
1550 nm	0.0003/0.0003	0.003/0.0028	0.0033/0.0031	0.996/0.997	0.015
CN Disk 2					
Wavelength	$\rho_{ns}+\tau_{ns}$	$\rho_l+\tau_l+\rho_d+\tau_d$	$\rho_l+\tau_l+\rho_d+\tau_d+\rho_{ns}+\tau_{ns}$	$\rho_{in}+\tau_{in}$	**Diffuse Scattering Coefficient** ($\beta_{diff\ sca}$) **1/cm**
532 nm	0.001/0.0015	0.010/0.011	0.011/0.013	0.968/0.976	N/A
633 nm	0.001	0.0055	0.007	0.988	N/A
1064nm	0.0005	0.0017	0.0022	0.998	N/A
1550 nm	0.0000	0.00075	0.00075	0.999	N/A
CN SQ 1					
Wavelength	$\rho_{ns}+\tau_{ns}$	$\rho_l+\tau_l+\rho_d+\tau_d$	$\rho_l+\tau_l+\rho_d+\tau_d+\rho_{ns}+\tau_{ns}$	$\rho_{in}+\tau_{in}$	**Diffuse Scattering Coefficient**

					($\beta_{diff\ sca}$) 1/cm
532 nm	0.0028/0.0035	0.153/0.153	0.156/0.157	0.702/0.696	0.211
633 nm	0.003	0.12	0.12	0.803	0.16
1064nm	0.0007	0.041	0.042	0.958	0.056
1550 nm	0.000	0.014	0.014	0.98	0.019
CN SQ 2					
Wavelength	$\rho_{ns} + \tau_{ns}$	$\rho_l+\tau_l+\rho_d+\tau_d$	$\rho_l+\tau_l+\rho_d+\tau_d + \rho_{ns} + \tau_{ns}$	$\rho_{in} + \tau_{in}$	**Diffuse Scattering Coefficient ($\beta_{diff\ sca}$) 1/cm**
532 nm	0.015/0.016	0.13/0.13	0.15/0.15	0.714/0.736	0.175
633 nm	0.01	0.088	0.098	0.824	0.121
1064nm	0.0033/0.003	0.034/0.04	0.037/0.043	0.957/0.95	0.055
1550 nm	0.0025/0.0025	0.012/0.011	0.015/0.014	0.98/0.978	0.016
JHUAPL Disk					
Wavelength	$\rho_{ns} + \tau_{ns}$	$\rho_l+\tau_l+\rho_d+\tau_d$	$\rho_l+\tau_l+\rho_d+\tau_d + \rho_{ns} + \tau_{ns}$	$\rho_{in} + \tau_{in}$	**Diffuse Scattering Coefficient ($\beta_{diff\ sca}$) 1/cm**
532 nm	0.0015/0.0014	0.011/0.011	0.013/0.012	0.98/0.982	0.027
633 nm	0.0007	0.0088	0.0095	0.981	0.022
1064nm	0.0005/0.0008	0.0082/0.0085	0.0087/0.0093	0.985/0.979	0.021
1550 nm	0.000/0.000	0.0061/0.0056	0.0061/0.0056	0.988/0.991	0.015

3.3.3.3 Diffuse Scatterance Model

A set of diffuse scatter models has been developed previously to fit measured scattering data for polycrystalline YAG and these can be applied to the case of spinel [110]. These models provide an accurate estimate of diffuse scatterance of spinel at wavelengths where experimental data is not available. In different spinel samples, we speculate the scatter is dominated by an index mismatch between spinel grains and impurity modified grain boundaries. Although no sintering aid has been used to produce CN spinel samples, results from LA-ICP-MS (which will be shown in Chapter 4) show a large amount of Ca in these samples. Indeed, different studies have shown that CaO has been found at spinel grain boundaries, creating a layer with a thickness of a few atoms[125], [127]. Even though no apparent pores or inclusions were observed in these spinel samples using SEM and AFM, numerous studies have suggested the possibilities of nano-sized pores in different transparent ceramic materials even without being optically detected [128], [129]. However, due to their small sizes (typically in the nanometer range or less), it is likely they do not contribute much to the scattering in the case of spinel.

In this study, to model the porosity in spinel, a spherical Anomalous Diffraction Approximation was used to model the Mie regime. A more complicated, coated sphere ADA was applied to represent the index mismatch between spinel and CaO. A Sellmeier model was developed for CaO based on the experientially measured refractive index values at different wavelengths obtained from the literature [130]. The coating thickness was chosen as 2 nm according to previous studies [125]. From both ADA models, the extinction efficiency associated with each scatter type was obtained to obtain the scattering coefficients. These scattering coefficients were then used with a Kubelka Munk model to fit the total diffuse scatterance of selected spinel samples. The resulting expression for Kubelka Munk model of diffuse reflectance used in this work is given as follows:

$$\mathrm{\rho_L}(\alpha_L, \beta_{sca}, d) = \frac{\mathrm{b_-} - \mathrm{b_+}\dfrac{\mathrm{b_-} - \mathrm{\rho_{Lsub}}}{\mathrm{b_+} - \mathrm{\rho_{Lsub}}}\mathrm{e}^{-2\sqrt{\frac{1}{\mathrm{\alpha_L^2}}-1}\beta_{sca}d}}{1 - \dfrac{\mathrm{b_-} - \mathrm{\rho_{Lsub}}}{\mathrm{b_+} - \mathrm{\rho_{Lsub}}}\mathrm{e}^{-2\sqrt{\frac{1}{\mathrm{\alpha_L^2}}-1}\beta_{sca}d}} \tag{3.20}$$

$$\mathrm{b}\pm = \frac{1}{\mathrm{\alpha_L}} \pm \sqrt{\frac{1}{\mathrm{\alpha_L}^2} - 1} \tag{3.21}$$

$$\mathrm{\alpha_L} = \frac{0.5\mathrm{\beta_{sca}}}{\mathrm{\beta_{abs}} + 0.5\mathrm{\beta_{sca}}} \tag{3.22}$$

$$\beta_{\mathrm{sca}}(r) = \mathrm{Q}_{\mathrm{sca}}\mathrm{A}(r)\rho_d \tag{3.23}$$

where ρ_L is the random diffuse reflectance, d is the propagation length, ρ_{Lsub} is the Lambertian total integrated reflection of a substrate (zero in this case), Q_{sca} is the scattering efficiency obtained from ADA models, $\mathrm{A}(r)$ and ρ_d represent the cross sectional area and the number density of scatterers as a function of the particle radius, respectively. A detailed procedure along with the model forms can be found in the work by Springer *et.al* [110]. Representative data fits for CN Disk 1 and CN SQ 2 are shown in Fig. 3.19 with the data fitting parameters listed in Table 3.11. Overall, the model represents a good fit of the data for both samples.

Table 3.11. Summary of Fitting Coefficients Used in the Kubelka Munk Model.

	r_{CaO} (μm)	$\rho_{d_{CaO}}$ (/cm^3)	r_{pore} (μm)	$\rho_{d_{pore}}$ (/cm^3)
CN Disk 1	0.46	$1.2\mathrm{x}10^{11}$	0.01	$2\mathrm{x}10^{14}$
CN SQ 2	1.33	$1.1\mathrm{x}10^{10}$	0.01	$1\mathrm{x}10^{14}$

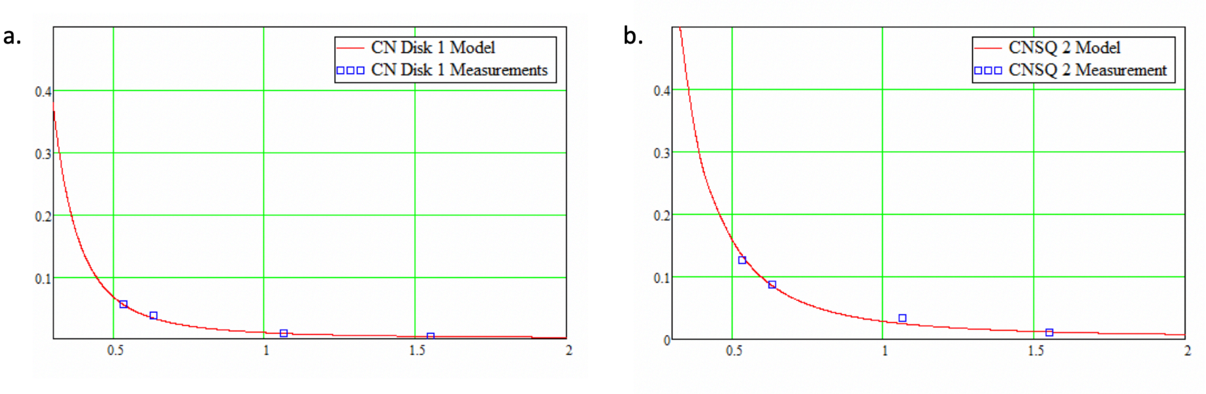

Figure 3.19. The Kubelka Munk model, show in red lines, using spherical ADA and coated spherical ADA for (a) CN Disk 1 and (b) CN SQ2. Measured total diffuse scatterance values from Table. 3.10 are shown in blue squares.

3.4 Conclusion

Scattering measurements at different wavelengths (405 nm, 532nm, 633 nm, 1064 nm, and 1550 nm) show that the total scatterance of as-received sapphire samples is in the range of 10^{-4} to 10^{-2}, while for extra-polished sapphire samples, the range lies between 10^{-5} and 10^{-3}. For spinel samples, the scatterance range is between 10^{-3} and 10^{-1}. Contributions to the scattering from surface roughness has been found to be insignificant compared to scattering losses from defects in the bulk and from the sub-surface and other surface artifacts. According to previous works, material defects including interstitial impurity atoms, dislocations and residual stress could alter the refractive index in certain regions and lead to scattering. These defects can be induced during the crystal growth and post-growth processing including surface polishing. The scatterance can be related to either the bulk or to the near-surface regions and the prevailing scatterer size can vary considerably depending on the actual methods used to produce the sapphire. A bulk single scatter model has been developed to fit the total and bulk scatterance of sapphire at different wavelengths. For spinel, a Kubelka-Munk wavelength-dependent scatter model along with spherical ADA models were used to fit the diffuse scatterance of selected samples.

Chapter 4. Materials Characterization

4.1. Introduction

As mentioned in Chapter 1, absorption and scattering in sapphire and spinel are related to materials defects such as lattice disorder, impurities, and point defects that originate from growth and post-growth treatment processes. Results in Chapters 2 and 3 show that at 1064 nm, the absorption coefficient in these materials ranges from 10^{-5} to 10^{-3} cm^{-1} while the scatterance level lies between 10^{-4} to 10^{-2}. These loss levels are higher than the desired level (i.e. $<10^{-6}$) so it is important to investigate the underlying sources of the optical losses. The defects associated with the observed losses are highly likely to be extrinsic which could be reduced or eliminated if improved manufacturing processes and post-growth treatments become available.

Point defects in crystalline materials, including anionic and cationic vacancies in different charge states as well as trace element impurities, are inevitably introduced during crystal growth and post-growth treatment [16]. They are known for causing both bulk and surface absorption losses at different wavelengths in crystalline semiconductors and insulators through electron/hole trapping, and interactions with impurities and dislocations [2,7]. In the cases of sapphire and spinel, both anionic and cationic vacancy-induced color centers are known to cause absorption bands in the UV and visible wavelength regions. However, no previous experimental studies have investigated how vacancy-type defects contribute to the optical losses in sapphire or spinel observed in the region near 1 μm. Furthermore, it is important to investigate different trace impurity elements present in both materials as some of them, for example, Ti and Fe ions, have been reported to be responsible for the weak absorption loss observed in the near-infrared wavelength region [48], [103].

Results in Chapter 3 showed that polished sapphire and spinel samples have different surface defects including impurity particles, scratches, digs, and polishing striations. These defects may possess special chemistries that can affect their scattering and absorption characteristics. Additionally, subsurface damage with a larger scale were also present and contributed to the observed scattering loss.

In this part of the overall study, different materials characterization techniques were used to investigate different types of defects existing in the bulk and at the surface of both sapphire and spinel. PALS measurements were carried out on three sapphire surfaces to identify cationic vacancy-related defect content. A two-component lifetime model was used to fit the PALS data and model parameters were extracted to perform a subsequent defect concentration analysis. Using the results from PALS and optical absorption measurements, correlations between sapphire vacancy-type defect concentrations and surface optical loss were established. LA-ICP-MS measurements were made on three sapphire and three spinel samples to study the potential trace element impurities. The results were used to interpret the absorption measurements performed earlier on different samples. SIMS was used to study the surface impurity content of extra-polished KO 2 and Raman spectroscopy analysis was performed on selected sapphire and spinel samples to investigate the chemistry associated with the observed surface defects. Finally, SEM-CL and TEM imaging analysis were conducted to investigate and visualize sub-surface damage in selected samples.

4.2. Methods

4.2.1 PALS

PALS measurements were performed at the Oak Ridge National Laboratory on the polished surfaces of three sapphire samples, GTAT 2, GTAT 3, and GTAT 5. Note that GTAT 5 was another disk sapphire sample obtained from GTAT with the same physical characteristics as those of GTAT 2 and 3. A conventional sample-source-sample geometry was prepared by directly evaporating a 20 μL $Na^{22}Cl$ solution (~3.7×10^5 Bq) onto the surface of one of the two disk samples, and then covering that disk with the other disk sample after the water evaporated. This 'sandwich' was then wrapped into 10 μm thick aluminum foil [131]. The PALS system operates in a double-stop mode and has a calculated system time resolution of ~160 ps. Each recorded lifetime spectrum contained a total of 1 million counts and was analyzed by fitting the exponential decay (after deconvolution of the resolution function) using two lifetime components.

4.2.2 LA-ICP-MS

An Agilent 8900 quadrupole ICP-MS was coupled to a Teledyne-Cetac Analyte G2 193 nm laser via SQUID tubing. The carrier gas was 0.75 l/min He, with an Ar nebulizing gas of 0.85 l/min in the ICP-MS. Data were processed using the trace element reduction scheme of Iolite (v4), using standard reference glass NIST 612 as the primary standard. An identical second standard was used to assess reproducibility. Line scans were used to minimize the effect of potential sample heterogeneity and minimizes downhole elemental fractionation during ablation. Each line scan had a length of approximately 1.5 cm and 40 seconds of gas background were run between line scans. For all line scans, analysis was done with a laser fluence of 5 J/cm^3, a repetition rate of 40 Hz, a 145x145 μm square spot size, and a scan translation speed of 20 μm/second. The laser ablation process was able to remove tens of microns of sapphire from the surface to expose the underlying clean material.

4.2.3 SIMS

The SIMS measurements were performed by EAG Laboratories using an ADEPT-1010 SIMS instrument from Physical Electronics. The sample was cut, mounted, and introduced to the UHV chamber. Subsequently, it was analyzed using a Cs primary ion beam and the ions were collected and detected. A reference material was also analyzed for quantification and the depth was measured with a stylus profilometer.

4.2.4 Raman Spectroscopy

A series of Raman spectra were acquired using a Horiba LabRAM HR evolution system using a 532-nm laser at the power of 5 mW. A 1800-lines/mm grating with spectral resolution of 0.5 cm^{-1} and a laser spot size of ~2 μm were used. The wavenumber range analyzed was chosen as 50 to 2000 cm^{-1} with a total acquisition time of 300 seconds.

4.2.5 SEM and TEM

SEM-CL images were acquired using Thermo Scientific Helios G4 UC coupled with a cathodoluminescence detector. The collection wavelength range was in the visible region. Sample cross sections were done by using a focused ion beam produced from a liquid Ga source. Subsequent TEM imaging analysis was performed using a Thermo Scientific TF30 300 kV TEM.

4.3. Results and Discussion

4.3.1 PALS Results

To better present the connection between the PALS results and optical absorption of each sapphire sample, some absorption results presented in Chapter 2 will be used and discussed again along with optical measurement results for GTAT 5. The measured UV-VIS transmittance and the calculated Fresnel reflectance for each sapphire sample were used to calculate extinction coefficients at each wavelength. A frequency-dependent scattering model was then applied to remove the scattering component from the total loss to isolate the absorption coefficient. The detailed procedure was described previously in Chapter 2. The results are shown in Fig. 4.1 where the absorption coefficients are plotted on a logarithmic scale as a function of the wavelength. Various absorption bands centered at different wavelengths appear in all three samples and are labeled to indicate the species associated with absorption. Among these bands, the one at 206 nm (6.1 eV) has been reported to be related to F centers associated with the neutral oxygen vacancies, V_O^0 [16], [37]. The bands at 225 nm (5.5 eV) and 255 nm (4.8 eV) are likely related to F^+ centers that are linked to V_O^{+1}[4,9]. In GTAT 2, the band at 225 nm does not appear and the adjacent band at 206 nm is narrower compared to that of GTAT 3, suggesting a reduced overall V_O^0 content. GTAT 5 also has a missing band at 225 nm, but its band at 206 nm is relatively broad. This indicates a small V_O^{+1} content but a moderately large V_O^0 concentration compared to GTAT 3. As discussed in Chapter 2, both types of F centers indicate oxygen deficiency during the growth process, and this is consistent with the growth conditions for the sapphire since all samples were produced in reducing environments. Furthermore, both the reducing growth condition and subsequent cooling process could result in a non-equilibrium vacancy concentration which could be much higher than the thermodynamic equilibrium state [16]. Additionally, previous experimental studies have shown that a cationic vacancy in sapphire may form V^{-2} and V^{-1} centers that cause absorption near 3 eV [11,12]. According to Fig. 4.1, GTAT 3 exhibits a wide absorption band near 3.1 eV and a partial absorption loss could be attributed to charged V_{Al}-induced color centers in addition to the well-known impurity band caused by Cr^{+3}. However, these centers were less noticeable in either GTAT 2 or 5 indicating a reduced defect concentration of charged V_{Al}.

Based on Eq. 2.6 from Chapter 2, the total concentration of V_o associated with the F centers can be estimated using the optical absorption coefficients. The calculated concentrations of V_O defects of each type are shown in Table 4.1. These results suggest that the concentrations of V_O^0 are at similar levels in GTAT 2 and 3 while GTAT 5 has a relatively higher V_O^0 content, but all have concentrations at levels of approximately 0.1 ppm. For V_O^{+1} content, calculations for GTAT 2 and 6 were based only on the absorption band at 255 nm since the band at 225 nm was not present. GTAT 3 appears to have the largest concentration of V_O^{+1} among all samples. At all other wavelengths, where no defect and impurity-related absorption bands are present, GTAT 3 shows a higher absorption loss than either GTAT 2 or 5 suggesting that charged V_O and V_{Al} defects and impurities may form additional defect states in the material. Previous computational studies have reported the formation energy of intrinsic V_O^0 to be in the range of 2 to 5 eV at 0 K [4,13,14]. Using these formation energy values, an equilibrium concentration of V_O^0 under the room temperature conditions was estimated to be in the range 10^{-60} to 10^{-30}/cm^3, which was much lower than the experimentally observed values. The higher concentrations of V_O^0 indicate a non-equilibrium point defect concentration in these sapphire samples due to their growth and post-growth treatments. It should be noted that V_O^{+2} was not considered in Smakula's equation but likely exists in the form of Schottky pairs in sapphire [13,15] and has been reported to cause small optical attenuation around the 200 nm wavelength region [96].

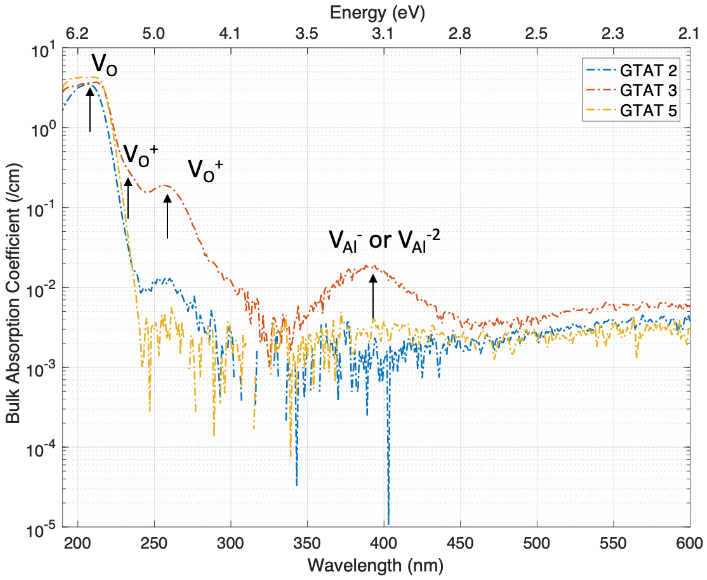

Figure 4.1. Bulk absorption in GTAT 2, 3, and 5 as a function of wavelength (blue, orange, and yellow broken lines respectively). Absorption bands are labeled with associated vacancy defects.

Table 4.1. Concentrations of Anionic Vacancy Defects in Sapphire

Sample	$C_{V_O^0}$ (ppm)	$C_{V_O^{+1}}$(ppm)
GTAT 2	0.57	0.00016
GTAT 3	0.59	0.012
GTAT 5	0.69	0.000066

PCI results of all samples obtained at three wavelengths are shown in Table 4.2. At 355 nm and 532 nm, bulk absorption values measured by PCI are in good agreement with the calculated values based on the UV-VIS measurements shown in Fig. 4.1. The bulk absorption losses for GTAT 3 and 5 at 355 nm and 532 nm from Table 4.2 indicate the existence of Ti^{3+} and Ti^{4+} impurities in these samples [135]. While Ti^{3+} is an isovalent impurity, Ti^{4+} appears as a heterovalent impurity that likely causes the formation of cationic vacancies and hole trapping centers to compensate for the higher valence charge state [16]. It is likely that a relatively higher concentration of cationic vacancies exists in both GTAT 3 and 5. At 1064 nm, GTAT 3 has a bulk absorption that is 4 times greater than absorption in GTAT 2 and is over 7 times higher than in GTAT 5.

Table 4.2. Optical absorption coefficients obtained from PCI measurements

Bulk Absorption Coefficient (ppm/cm) and Surface Absorbance (ppm)

Sample	355 nm		532 nm		1064 nm	
	Bulk	Surface	Bulk	Surface	Bulk	Surface
GTAT 2	1790	208	1070	81.1	45	4.8
GTAT 3	4950	940	6210	426	180	20.5
GTAT 5	903	301	1140	158	24	16

As discussed in Chapter 2, in the region between 600 and 1200 nm, previous studies on sapphire have indicated an exponentially decreasing bulk absorption known as the weak absorption tail that is likely related to states in the bandgap caused by lattice disorder and impurities [13], [90]. Defects such as vacancies, dislocations, and impurities are the main contributors to the optical absorption loss in this region and can trap holes or electrons generating localized changes to the optical properties [7]. Previous density-functional theory (DFT)-based computational studies have shown that both neutral and negatively charged V_{Al} result in optical attenuation in the near-infrared wavelength region at room and elevated temperatures [96].

In contrast to the bulk measurements, surface absorbance measured using PCI yields a different story that is indicated by Table 4.2. Although GTAT 5 has a lower bulk absorption loss at all three wavelengths compared to GTAT 2, its surface absorbance becomes approximately two to three times larger than that of GTAT 2 at both 532 nm and 1064 nm. Furthermore, at 1064 nm, bulk and surface absorption losses for GTAT 5 are at the same level indicating a relatively large population of absorbing species near the surface. Similar to the bulk absorption loss, GTAT 3 has the largest surface absorption loss at all the measured wavelengths. Since the formation energies of different types of intrinsic defects are lower for material near the surface, the defect population density in these regions should be higher than in the bulk. Moreover, defect populations in the near surface region also include a range of extrinsic defects as sapphire used for optical components undergoes post-growth processing steps such as grinding and polishing [22- 24].

Results from the PALS measurements provided positron lifetime spectra, shown in Fig. 4.2, that were analyzed using a two-component lifetime model. The fitting parameters used in this model include: τ_1, the bulk sapphire positron annihilation lifetime; τ_2, the defect-related lifetime; and I_i , the intensity associated with each lifetime component [131]. In this study, τ_1 was fixed at 140 ps because this is the positron lifetime that is reported for bulk sapphire having no defects (including vacancy-type defects) [26-29]. The mean lifetime <τ>, represents the geometric mean of the measured lifetime components and is calculated from $\langle\tau\rangle = \tau_1 I_1 + \tau_2 I_2$, where $I_1 + I_2 = 1$ [131]. The list of all parameters along with the calculated mean positron lifetime for each sample can be found in Table 4.3. Note that the fitting error associated with τ_2 is approximately 5%.

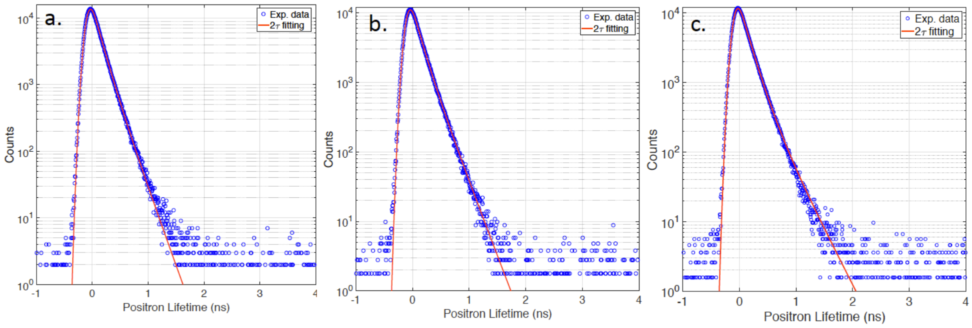

Figure 4.2. Positron lifetime spectra for single crystal sapphire samples used in this study. Data points indicate measured counts while the solid curves represent fits to the data using a two-component lifetime model (a) GTAT 2, (b) GTAT 3, (c) GTAT 5.

Table 4.3. PALS analysis results of the studied samples

Sample	Bulk Lifetime τ_1	Defect-Related Lifetime τ_2	Bulk Intensity I_1	Defect-Related Intensity I_2	Mean Lifetime <τ>
GTAT 2	140 ps	189 ps	84%	16%	147.9 ps
GTAT 3	140 ps	247 ps	79%	21%	162.5 ps
GTAT 5	140 ps	272 ps	79.6%	20.4%	166.9 ps

Results in Table 4.3 indicate that GTAT 5 has a longer τ_2 component as well as an increased intensity associated with it contributing to an overall longer mean positron lifetime. Longer average lifetimes are associated with a larger average defect size (associated with τ_2) and/or a higher average defect concentration (associated with I_2) [131]. Among different vacancy-type defects, positively charged defects do not interact strongly with positrons due to repulsive Coulombic interactions between the positron and the local charge density. For sapphire, this suggests that aluminum vacancy-type defects are more likely to be measured by PALS compared to oxygen-related vacancies [25], [30,31]. Furthermore, previous studies reported the positron annihilation lifetime of a single Al vacancy was 165 ps [36]. Since τ_2 of all samples are larger than 165 ps, all samples are likely to have divacancy or small vacancy clusters. Indeed, divacancy-related defects have been shown to have a lifetime in the range of 194 ps to 220 ps in Al_2O_3 thin films [36]. Results obtained from PALS indicate that GTAT 5 has a comparable cationic vacancy-type defect concentration to that of GTAT 3 while also having a larger average defect size. Since PALS measurements were performed on the polished surfaces of each sample and the positron penetration depths can be hundreds of micrometers, the measured results should most closely relate to the defect states in the near-surface region. Indeed, PCI results show that GTAT 3 and 5 have a relatively large surface absorbance at all wavelengths. Although loss in GTAT 5 appeared to be lower than that of GTAT 3, the UV-VIS measurements indicated a relatively larger V_O^0 concentration in GTAT 5. In an ionic crystal, the creation of an anionic vacancy is typically accompanied by the creation of a cationic vacancy to achieve the overall charge conservation. At 1064 nm where GTAT 5's surface absorption loss is comparable to its bulk loss, a larger quantity of cationic vacancies could correlate with such optical attenuation [142].

Previous work has suggested that Schottky defects (aluminum and oxygen vacancies generated in a stoichiometric ratio) are more likely to form compared to Frenkel defects (aluminum or oxygen vacancy/interstitial pairs) under the equilibrium condition since the former have smaller formation energies [13,15]. Additionally, Schottky defects are known to form near the surface where they could arise from elevated dislocation concentrations that result from grinding and polishing [16]. Furthermore, a recent computational study suggested there are two more types of Schottky defect that could form in sapphire under the oxygen-deficient growth environments, $(2V_O^{+1}:V_{Al}^{-2})$ and $(3V_O^{+1}:V_{Al}^{-3})$, owing to their lowered formation energies [43]. Also, other cationic vacancy-associated clusters, including $(V_O^{+2}:V_{Al}^{-3})^{-1}$, $(2V_O^{+2}:2V_{Al}^{-3})^{-2}$, $(3Ti_{Al}^{+1}:V_{Al}^{-3})$, $(2Ti_{Al}^{+1}:V_{Al}^{-3})^{-1}$, and $(Ti_{Al}^{+1}:V_{Al}^{-3})^{-2}$ could also be found in sapphire [38]. Since PALS results for all samples indicated large defect sizes that were likely associated with vacancy clusters, the neutral and negatively-charged vacancy-related defect structures noted here were likely among the positron trapping centers in the sapphire samples studied in this work.

The vacancy defect concentration can be estimated using a two-state trapping model that takes into account positron trapping both in the bulk and at defect sites [25,33]. In this model, the net positron trapping rate for defects, κ, can be found by using I_1, I_2, and τ_2 along with the following expression:

$$\kappa = \frac{I_2}{I_1}(\tau_B^{-1} - \tau_2^{-1}) \tag{4.1}$$

where τ_B is the positron lifetime in the bulk [131]. The trapping rate is directly proportional to the concentration of defects, *C*, through

$$\kappa = \mu C \tag{4.2}$$

where μ is the trapping coefficient associated with a specific defect type [25,33]. At room temperature, this coefficient typically is in the range of 5 x 10^{14} to 5 x 10^{15} s^{-1} for semiconductors [25,28]. Unfortunately, no available information has been reported experimentally or theoretically for Al-related trapping coefficients in sapphire. Based on the studies of different semiconductors, the trapping coefficients of neutral, singly negative, and doubly negative V_{Al}-associated defects could be estimated as 6 x 10^{14}, 2.5 x 10^{15}, and 5 x 10^{15} s^{-1}, respectively [139]. Additionally, similar data were also reported on V_{Al}-associated defects for aluminum alloys at room temperature [34]. For a small vacancy cluster with *n* vacancies, Hu *et al.* have proposed a specific trapping coefficient as $\mu_{V_n} = (\frac{r_{vn}}{r_v})^2 \mu_v$, where $r_{v_n}$is the radius of the defect cluster containing *n* vacancies, r_v is the trapping radius of a single vacancy-type defect, and μ_v is the trapping coefficient as $\mu_{V_n} = (\frac{r_{vn}}{r_v})^2 \mu_v$, where $r_{v_n}$is the radius of the defect cluster containing *n* vacancies, r_v is the trapping radius of a single vacancy-type defect, and μ_v is the trapping coefficient associated with a specific defect type (neutral or charged)[131]. The trapping rate of each sample was calculated based on the PALS result using Eq. (4.1) and the values are 3.53 x 10^8 s^{-1}, 8.23 x 10^8 s^{-1}, and 8.88 x 10^8 s^{-1}, for GTAT 2, 3, and 5, respectively. These values were used to obtain an estimate of the cationic vacancy-type defect concentrations.

It is difficult to identify which V_{Al}-related defect clusters dominate in the sapphire samples but simple estimations are possible using information extracted from the optical measurements presented here along with results from computational studies in the literature. Only three types of V_{Al}-related clusters (neutral, singly, and doubly negative charged) that were previously mentioned are considered because aluminum-related point defects such as interstitials and antisites are less likely to trap positrons. Therefore, all three types of V_{Al} -associated small vacancy clusters (i.e. $(2\,V_O^{+1}\!: V_{Al}^{-2})$, $(3\,V_O^{+1}\!: V_{Al}^{-3})$, $(3\,V_O^{+2}\!: 2V_{Al}^{-3})$, $(V_O^{+2}\!: V_{Al}^{-3})^{-1}$, $(2V_O^{+2}\!: 2V_{Al}^{-3})^{-2}$, $(3\,Ti_{Al}^{+1}\!: V_{Al}^{-3})$, $(2Ti_{Al}^{+1}\!: V_{Al}^{-3})^{-1}$, $(Ti_{Al}^{+1}\!: V_{Al}^{-3})^{-2}$) could contribute to the defect-related lifetime component, τ_2. Assuming they share a similar positron lifetime, Eq. (4.2) could be expressed as follows:

$$\kappa = \mu_{V_{Al}} C_{V_{Al}} + \mu_{V_{Al}^{-}} C_{V_{Al}^{-}} + \mu_{V_{Al}^{-2}} C_{V_{Al}^{-2}} \tag{4.3}$$

Using the concentration of V_O^{+1} from UV-VIS data (10^{-5} to 10^{-2} ppm level), concentrations of $(2V_O^{+1}: V_{Al}^{-2})$ and $(3V_O^{+1}: V_{Al}^{-3})$ could be estimated. Given the concentration level of $\mathrm{V}_\mathrm{O}^{+1}$ was at the 10^{-10} and 10^{-11} for GTAT 2 and 5 respectively, the maximum concentration level of $(2V_O^{+1}: V_{Al}^{-2})$ and $(3V_O^{+1}: V_{Al}^{-3})$ in GTAT 2 and 5 would also be at ~10^{-11} to 10^{-10} as $\mathrm{V}_\mathrm{O}^{+1}$ acts as the limiting factor. In GTAT 3, the maximum concentration level of both clusters would be around 10^{-8}. The trapping coefficient of both clusters was estimated to be at the level of 10^{15} s^{-1} based on the defect cluster volume approximated using Voronoi tessellation. By combining the defect concentration and trapping coefficient for each sample, the contribution from both types of vacancy clusters (10^5 s^{-1} and 10^4 s^{-1} for GTAT 2 and 5 and 10^7 s^{-1} for GTAT 3) to the trapping rate, κ, could be estimated and was very small, suggesting other V_{Al} -related vacancy clusters may contribute more to the longer positron lifetime. The remaining possible vacancy clusters include $(3\,V_O^{+2}: 2V_{Al}^{-3})$, $(V_O^{+2}: V_{Al}^{-3})^{-1}$, $(2V_O^{+2}: 2V_{Al}^{-3})^{-2}$, $(3Ti_{Al}^{+1}: V_{Al}^{-3})$, $(2Ti_{Al}^{+1}: V_{Al}^{-3})^{-1}$, $(Ti_{Al}^{+1}: V_{Al}^{-3})^{-2}$. Since GTAT 2 did not exhibit a noticeable optical attenuation due to Ti^{4+} compared to the other two samples, it is reasonable to exclude Ti-related vacancy clusters. Among three vacancy clusters of $(3V_O^{+2}: 2V_{Al}^{-3})$, $(V_O^{+2}: V_{Al}^{-3})^{-1}$, $(2V_O^{+2}: 2V_{Al}^{-3})^{-2}$, the specific trapping coefficient associated with each was calculated to be $2.0\text{x}10^{15}$ s^{-1}, $4.4\text{x}10^{15}$ s^{-1}, and $1.4\text{x}10^{16}$ s^{-1}. The minimum and maximum coefficient values can be used to estimate the upper and lower bounds of V_{Al} -related defect cluster concentration. For GTAT 3 and 5, Ti-associated vacancy clusters need to be considered. However, it is difficult to obtain the atomic volume associated with the substitutional defect Ti_{Al}^{+1} so it was treated as having the same volume of an Al atom in sapphire. The real volume associated with a Ti atom sitting at an Al site should be slightly larger compared to that of an Al atom due to the larger atomic radius of Ti. For GTAT 3 and 5, the minimum and maximum trapping coefficients from all possible V$_{Al}$-related vacancy clusters were estimated to be 1.5x10^{15} s^{-1} (from $(3Ti_{Al}^{+1}: V_{Al}^{-3})$) and 1.4 x10^{16} s^{-1} (from $(2V_{O}^{+2}: 2V_{Al}^{-3})^{-2}$).

Using values for the trapping coefficients, the V$_{Al}$-related defect cluster concentration in each sample could be estimated along with the upper and lower limits depending on the defect type, and the results are shown in Table 4.4. Since the calculated trapping coefficients were based on the estimated values for different V$_{Al}$-related defects (which could differ considerably from actual values), a large uncertainty exists in the estimated defect concentrations (factor of two to three) [131]. One observation from the estimated defect concentrations shown in Table 4.4 is that charged vacancy clusters tend to have a smaller concentration due to a relatively higher trapping coefficient value, which is reasonable since the locally-unbalanced charge is not favored by the overall system. The results in Table 4 indicate that the positron trapping rates of GTAT 3 and 5 are twice that of GTAT 2 since both have larger τ_2 and I_2 values. Similarly, based on the specific trapping coefficient value associated with V$_{Al}$ -related divacancy defect, the V$_{Al}$-related defect cluster concentrations are higher in GTAT 3 and 5 by a factor of two or three compared to GTAT 2. Note that other vacancy-impurity complexes or negatively charged dislocations, which could potentially contribute to positron trapping in sapphire, were not considered. Additionally, V_O^0 could possibly be present in any of the vacancy clusters due to its neutral charge state and this would produce a larger defect size.

Table 4.4. Estimated Vacancy Defect Concentrations in Sapphire

Sample	Total Trapping Rate, κ (10^{8} s^{-1})	Calculated Trapping Coefficients, $\mu_{di-V_{Al}}$ (10^{15} s^{-1})	Estimated Total V$_{Al}$ - Related Defects Concentration (ppm)
GTAT 2	3.53	2-14	0.025-0.18
GTAT 3	8.23	1.5-14	0.059-0.55
GTAT 5	8.88		0.064-0.59

The results in this section for vacancy-related defect concentrations in sapphire were obtained using techniques that are complementary in many ways. PALS is sensitive to defect structures that carry a negative or a neutral charge while many features in the optical absorption spectrum in the visible and near infrared are associated with defects that are either neutral or positively charged. PALS is likely more sensitive to defects near the surface owing to the finite penetration depth of positrons into the sample surface. Total concentrations for V_{Al} (based on PALS) and V_O (based on optical absorption) were found to be in the 0.01 to 1 ppm range with the concentration of defects in GTAT 3 and 5 being higher than in GTAT 2. Different V_O defects along with different trace impurities are optically active in the UV and visible wavelength regions, while both neutral and charged V_{Al}-related defects are more influential in the near-infrared and infrared regions [96].

Since PALS measurements were done on the polished surfaces of all samples and the typical penetration depth of the positron is on the order of hundreds of micrometers, the measured lifetime results should provide better information of defects (i.e. size and concentration) residing near the sapphire surface compared to those in the bulk. GTAT 2 and 5 had a similar, low-level bulk absorption across all wavelengths, and UV-VIS results indicated that these samples had fewer impurities and charged color centers. However, the surface absorption losses proved to be significantly different owing to defect structures likely introduced during grinding and polishing. PALS results for GTAT 5 included larger τ_2 and I_2 values compared to those of GTAT 2, suggesting a higher cationic vacancy-related defect concentration as well as larger defect sizes near the surface. Moreover, GTAT 5 had a longer defect-related lifetime (about 26 ps higher) than that of GTAT 2. Surface absorbance measurements at 355 nm and 532 nm differed by a factor of

1.5 to 2 whereas at 1064 nm this factor increases to 3 (see Table 4.2). Note that the smaller difference at 355 nm could be caused by a higher concentration of F^+ centers in GTAT 2 which would contribute less when moving to the longer wavelength regions. At longer wavelengths, cationic vacancy defects likely play a more important role. The positron lifetimes measured by PALS indicated that the near-surface, cationic vacancy-related defect concentrations in GTAT 3 and 5 are at a similar level while defect sizes are likely larger in GTAT 5. This is supported by the somewhat higher defect-related mean lifetime component in GTAT 5 and the comparable I_2 values for GTAT 3 and 5 which only differed by 0.6% (within the 5% fitting uncertainty). The larger defect size could result either from larger vacancy clusters or vacancy-decorated dislocations that could be introduced by grinding and polishing processes [4,24]. It is useful to note that increased cationic defect concentrations resulting from polishing-generated dislocations have been detected by PALS in both ZnO and GaN [35-37]. In these materials, both cationic vacancy-related clusters as well as vacancy-dislocation complexes acted as the positron trapping centers. In the case of sapphire, even though no previous studies have measured the positron lifetimes associated with dislocations, values have been reported for single-crystal aluminum that are in the range of 210 to 240 ps, comparable to the measured defect lifetimes of GTAT 3 and 5 [147]. When examining the surface absorbance of these samples at 355 nm and 532 nm from Fig. 4.3, loss is higher in GTAT 3 by factors of 3 and 2.5, respectively. These differences could be due to higher populations of point defects in GTAT 3 beyond the V_{Al}-related ones (i.e. single anionic vacancies, positively charged vacancy clusters, and additional impurities). Interestingly, at 1064 nm, the surface absorbance of both samples was very close. Since the average concentrations of V_{Al}-related clusters measured by PALS were comparable and these defects tend to be more optically active in sapphire in the near-infrared wavelength region, the higher surface absorbances recorded at 1064 nm indicate higher cationic vacancy-related defect concentrations in these samples.

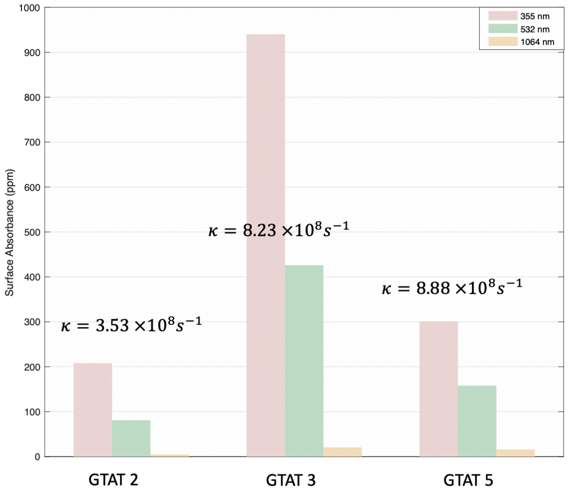

Figure 4.3. A Bar plot shows the total surface absorbance of each sample at each wavelength. The positron trapping rate is labeled for each sample.

4.3.2

The LA-ICP-MS line scan measurements were performed on three sapphire samples (GTAT 1, Guild 1, and KO 1) and three spinel samples (CN Disk 1, JHUAPL Disk, and CN SQ). Results from the three sapphire samples are shown in Table 4.5 and indicate that various trace element impurities are present in all three sapphire samples and their concentration levels range from 0.001 to 100 ppm. These results are comparable to previously reported values in the literature [34], [48], [122]. Concentrations of both Si and Ca appear to be relatively high compared to the presence of other elements in all samples and both elements tend to be optically inactive as neither is associated with the absorption bands observed in Fig. 2.3. A further comparison between the results shown in Table 4.5 and Fig. 2.3 confirms several absorption band identifications discussed in Chapter 2. For instance, the concentration of V is the highest in Guild 1 that possibly causes a broadened absorption peak near 6 eV. Similarly, the concentration of Ti appears to be the highest in Guild 1 and lowest in GTAT 1, which corresponds to the level of absorption observed near 532 nm in each sample seen in Fig. 2.3. Furthermore, the large Cr^{3+} associated absorption band near 400 nm in Guild 1 is likely related to a higher Cr^{3+} concentration since the other two samples have a relatively lower concentration of Cr and their Cr-related absorption bands are smaller. Finally, the broad absorption band features near 255 nm and 360 nm seen in Guild 1 are also linked to a higher Fe concentration.

Table 4.5. Concentrations Different Trace Impurities Present in GTAT 1, Guild 1, and KO 1

Concentration (ppm)	GTAT 1	Guild 1	KO 1
Mg	0.0905	0.0705	0.284
Si	7.50	78.4	18.9
P	0.203	0.456	0.472
Ca	185	177	237
Ti	0.0058	0.0308	0.0137
V	0.0091	0.0502	0.0024
Cr	0.0888	0.282	0.193
Fe	1.58	5.45	1.85
Cu	0.00255	0.00779	0.0688
Mo	0.0413	0.0156	0.0256
Sn	0.0035	0.0256	0.0102
Zn	0.0310	0.165	0.0762
Mn	N/A	0.00315	0.00128
Ni	0.00522	N/A	0.00659
Co	0.000417	0.00240	0.000656

According to numerous studies, both Ti and Fe impurities are not only responsible for causing absorption losses in the UV-Visible region in sapphire but also in the near-infrared where HEL operate [38], [45], [86]. Each type of impurity exists in two oxidation states such as Ti^{+3}/Ti^{+4} and Fe^{+2}/Fe^{+3}. In the case of sapphire, the most stable form of Ti and Fe are Ti^{+3} and Fe^{+3} as they serve as isovalent substitutes for Al^{3+}. The heterovalence impurities such as Ti^{+4} and Fe^{+2} are present at a relatively lower concentration in sapphire due to their defect formation mechanisms which can be described as follows [86]:

$$3\mathrm{TiO_2} + 4\mathrm{Al}_{\mathrm{Al}}^{\mathrm{x}} \rightarrow 3\mathrm{Ti}_{\mathrm{Al}}^{\cdot} + \mathrm{V}_{\mathrm{Al}}^{\prime\prime\prime} + 2\mathrm{Al_2O_3} \tag{4.5}$$

$$2\mathrm{TiO_2} + 2\mathrm{Al}_{\mathrm{Al}}^{\mathrm{x}} \rightarrow 2\mathrm{Ti}_{\mathrm{Al}}^{\cdot} + \mathrm{O}_{\mathrm{i}}^{\prime\prime} + \mathrm{Al_2O_3} \tag{4.6}$$

$$2\mathrm{FeO} + 2\mathrm{Al}_{\mathrm{Al}}^{\mathrm{x}} \rightarrow 2\mathrm{Fe}_{\mathrm{Al}}^{\prime} + \mathrm{V}_{\mathrm{o}}^{\cdot\cdot} + \mathrm{Al_2O_3} \tag{4.7}$$

$$3\mathrm{FeO} + 2\mathrm{Al}_{\mathrm{Al}}^{\mathrm{x}} \rightarrow 3\mathrm{Fe}_{\mathrm{Al}}^{\prime} + \mathrm{Al}_{\mathrm{i}}^{\cdot\cdot\cdot} + \mathrm{Al_2O_3} \tag{4.8}$$

Previous work has shown that the Ti^{3+}/Ti^{4+} transition (through intervalence transfer) occurs at ~800 nm while the Fe^{2+}/Fe^{3+} transition occurs at ~900 nm and 1100 nm (through intervalence transfer or d-d transition), with both transitions leading to a wide absorption band at the corresponding wavelength [86], [148]. Moreover, different studies have reported cross sections associated with Ti^{4+} and Fe^{2+} are in the range of 10^{-19} to 10^{-17} cm^2 so that a 1 ppb level concentration of either impurity could induce an absorption loss of 10 to 1000 ppm cm^{-1} at 1064 nm [48]. In addition to these homonuclear transitions, charge transfers in a complex cluster containing Ti^{4+}, Fe^{2+}, and aluminum/oxygen vacancies at 700 nm may also contribute to the absorption loss. Similarly, absorption bands at 790 nm and 878 nm have been found to be related to the $\mathrm{Fe}^{2+} + \mathrm{Ti}^{4+} \rightarrow \mathrm{Fe}^{3+} + \mathrm{Ti}^{3+}$ intervalence charge transfer. With this information, examining the Ti and Fe concentrations in GTAT 1 and Guild 1 from Table 4.5 and their absorption losses shown in Fig. 2.3 and Fig. 2.4, it can be concluded that a higher concentration of Ti and Fe is linked to a higher absorption loss in the near-IR for HEM grown sapphire. The average concentrations of Ti and Fe in Guild 1 are higher compared to those in GTAT 1 by factors of six and three respectively, while Guild 1 also has a larger bulk absorption loss than that of GTAT 1 at 1064 nm by a factor of three. As seen from Section 4.3.1, different types of cationic and anionic vacancies also occurred in similar sapphire samples at comparable concentration levels. It is possible that more Ti^{3+}/Ti^{4+} and Fe^{2+}/Fe^{3+} transitions occurred with the assistance of vacancies in Guild 1, resulting in a higher residual absorption loss at 1064 nm. However, it is important to realize the probability of intervalence charge transfer transitions between the neighboring impurity atoms is extremely low (owing to the low impurity concentration in this case) if assuming impurities are randomly distributed inside sapphire. In sapphire grown with different growth methods, both microstriations (mainly due to the temperature gradient formed at the crystallization front and impurity transport phenomena near that region) and blocks (primarily due to dislocation motions) have been commonly observed due to non-perfect growth processes [16]. Impurities are often found to be segregated along these defects thus increasing the probability of charge transfers between different impurity atoms and the formation of defect clusters [16].

By comparison, KO 1 had a much higher average bulk absorption coefficient with a large standard deviation at 1064 nm compared to the other two samples. Note that KO 1 was manufactured with the Kyropoulos method under an oxidizing environment. Table 4.5 shows KO 1 has a comparable level of concentration of each impurity with respect to the other samples except for Cu. A difference by a factor of 10 has been observed for Cu concentration in KO 1 compared to the other two samples but it should be noted that the overall concentration level is small (i.e. ~0.001 to 0.01 ppm). Previous studies have shown the possible optical absorption loss is associated with Cu^{2+} near 1 μm, but it is unlikely to be the sole cause for the high loss seen in KO 1 owning to its small concentration [149]. According to Fig. 2.3, the oxygen vacancy concentration of KO 1 is much lower compared to other HEM-grown sapphire samples. While an oxidizing growth environment could mitigate the absorption loss due to color centers in the visible wavelength region, it also leads to different oxidation states of the impurity elements in sapphire. For example, annealing treatments under an oxidizing environment of sapphire could lead to an increased concentration of Ti^{4+} [48]. According to Eq. (4.6), the accompanying compensation mechanism for this extra positive ion is the interstitial oxygen from an oxygen-rich environment. Since Ti^{+4} has been reported to have a relatively large cross section (~10^{-17} cm^2), a small increase in its concentration could result in a large absorption loss in the near-IR wavelength region. Similarly, Cr^{4+}, which has been known to cause absorption in YAG at 1 μm, can also form under a similar condition [150]. Finally, other impurities such as Ni and Co also present in KO 1 at the small levels shown in Table 4.5. For the sake of charge neutrality in sapphire, they typically exist in the forms of Ni^{3+} and Co^{3+} with a small amount being Ni^{2+} and Co^{2+}, which are known for causing absorption near the 1 μm region in glass [149]. With more oxygen atoms introduced from the growth environment, these impurities atoms might undergo an oxidation process which then contributed to the optical absorption. Therefore, an oxidizing sapphire growth environment or annealing treatment could mitigate the absorption losses due to color centers in the UV-Visible wavelength region. However, such an environment may also produce changes in oxidation states of different impurity elements that ultimately result in higher absorptions at longer wavelengths. Additionally, in a recent work done by Marchio *et al*, the inhomogeneity of the absorption loss within a Kyropoulos-grown sapphire has been reported to be caused by striations due to a poorly controlled growth process [151]. A high level of striation density is associated with non-uniform temperature at the crystallization front and impurities are likely to be trapped at the striation sites [16], [151].

The LA-ICP-MS measurements were also performed on CN Disk 1, CN SQ 2, and JHUAPL Disk and the results are presented in Table 4.6. Overall, most impurities in spinel have a concentration level range between 1 to 1000 ppm, which is much higher than in sapphire. Similar to sapphire samples, all three spinel samples have relatively large concentrations of Si and Ca that are not known to be optically active in the near-infrared region [149], [152], [153]. Additionally, the CN samples were found to have additional trace impurities such as K and Na that were not detected in the JHUAPL Disk. Also, the impurity concentrations in CN samples are relatively higher compared to those in JHUAPL Disk suggesting more impurities existed in the spinel powder used to grow CN samples.

According to Table 2.6 in section 2.3.2, the JHUAPL Disk has an absorption coefficient of 10^{-2} cm^{-1} at 1064 nm which is higher than those of CN SQ 2 and CN Disk by a factor of 2 and 50, respectively. A closer examination of Table 4.6 suggests only Ti and Co are likely to cause a large optical loss in JHUAPL Disk since concentrations of both elements are higher in JHUAPL Disk than those in CN SQ 2 and CN Disk 1 by a factor of 10. Although Co^{2+} has been reported to be associated with absorption bands observed in glass in the near-infrared wavelength region, it mainly causes optical losses in the visible region (near 600 nm) in spinel [149], [154]. Therefore, compared to Ti, Co should have a relatively smaller contribution to the absorption at 1064 nm of the JHUAPL Disk. Similar to the Ti^{3+}/Ti^{4+} transition that occurs at ~800 nm in sapphire, Ti-doped spinel has also been found to have an absorption band at 780 nm [103]. Furthermore, studies have shown a broad absorption band at 790 nm in spinel that is associated with the intervalence charge transfer between Fe^{2+} and Ti^{4+} when both ions are in an edge sharing condition, similar to that reported in sapphire [100], [103]. Additionally, Fe has been found as a common impurity in spinel that replaces Mg and Al atoms at the tetrahedral and octahedral sites [107], [154]. Broad absorption bands observed in spinel at 690 nm and 1050 nm have been prevalently found to be associated with an electronic transition of Fe^{2+} -Fe^{3+} intervalence charge transfer and that of Fe^{2+} -Fe^{3+} exchange-coupled pairs at the octahedral sites, respectively [107], [155]. Moreover, studies also indicate that the amount of and the distribution of Fe^{2+} and Fe^{3+} heavily depend on the purity of the starting powder, the cooling rate used during spinel growth and annealing, as well as the stoichiometry [155]. With this information, one interesting finding for CN SQ 2 and the JHUAPL Disk is that their measured Fe concentrations show some deviations according to Table. 4.6. Additional Fe concentration results measured from a different location on each sample are reported in the table for all three spinels since large differences were observed in CN SQ 2 and the JHUAPL Disk. No such differences were noticed for concentrations of other impurity elements. Recall the PCI measured absorption coefficients of spinel samples in Table. 2.6 where the optical absorption losses at 532 nm and 1064 nm in both CN SQ 2 and JHUAPL Disk are spatially inhomogeneous because some regions in these samples have a higher loss compared to other locations. By comparison, absorption losses in CN Disk 1 appeared to be spatially homogenous and it also has a consistent Fe concentration according to Table 4.6. Given the fact that the Fe (in both Fe^{2+} and Fe^{3+} states) distributions are not uniform in CN SQ 2 and in the JHUAPL Disk based on the LA-ICP-MS results, the absorption losses seen in these samples should also vary spatially across these samples. This is somewhat similar to the absorption behavior observed in KO 1 as the oxidizing growth environment produced different valence states of numerous impurities in the sample leading to the localized absorption differences. It appears that the near-infrared absorption loss being slightly higher in the JHUAPL Disk compared to that of CN SQ 2 indicates that Ti should be mainly responsible for the loss in the JHUAPL Disk due to its high concentration while Fe contributes more to the loss in CN SQ 2. The intervalence charge transfer between Fe^{2+} and Ti^{4+} could further add to the losses in both samples depending on their distributions within the samples.

A surprising finding is related to the impurity concentrations measured in CN Disk 1. According to Table 2.6, at 1064 nm, CN Disk 1 has an absorption loss level at 100 ppm/cm while CN SQ 2 has a level in the 1000 to 10000 ppm/cm range. One would expect CN Disk 1 to have lower concentrations of different impurity elements but the results in Table 4.6 do not support the assumption. Indeed, trace impurity elements such as Cu, Ni, Co are known to cause absorption losses in the near-infrared; however, the fact that their concentrations are comparable in both samples and some are slightly higher in CN Disk 1. This implies these impurities do not contribute much to the large discrepancy in the measured absorption losses. Next, the concentration of Ti is comparable in both samples which means the homonuclear transition between Ti^{3+} and Ti^{4+} is not the main cause of the absorption discrepancy either. Thus, the concentration difference of Fe in the two samples should be closely linked to the observed absorption difference. There are two possible absorption loss mechanisms associated with Fe in this case. One is the transition through Fe^{2+}-Fe^{3+}exchange-coupled pairs that occurs at 1050 nm and the other one is through the intervalence charge transfer between Fe^{2+} and Ti^{4+} happening at 790 nm [107], [154], [155]. The later mechanism should not be the dominant contributor because both CN Disk 1 and SQ 2 have a similar Ti concentrations so the most probable cause is the homonuclear transition of Fe. In spinel, to compensate the negative charge due to a Fe^{2+} ion substituting an Al^{3+} ion, oxygen vacancies such as V^{2+} and V^{1+} and an antisite defect of Al_{Mg}^{1+} must be created to maintain the charge neutrality [155]. To weaken the absorption due to Fe^{2+} near 1000 nm, either the overall Fe concentration should be minimized or the presence of the compensating factors must be reduced. Indeed, CN Disk 1 has a relatively lower Fe concentration compared to that in CN SQ 2. More interestingly, CN Disk 1 also has many more F centers and V centers according to results in Fig.2.6. Therefore, it is likely that most of the positively-charged vacancies and antisite defects are balanced by the negatively charged vacancy-type defects in CN Disk 1, and fewer of them are available to compensate Fe^{2+}, thus lowering probability of the Fe^{2+}/Fe^{3+} transition.

In both sapphire and spinel samples, we have detected different trace impurity elements that were responsible for the absorption losses at different wavelengths. In particular, both Fe and Ti were found at a relatively high concentration in these samples and both elements were primarily responsible for the residual optical loss near the 1μm region according to different studies. The fall-off of the broad absorption bands linked with these impurities occurring near the 1μm region contributed to the observed weak absorption tail in both sapphire and spinel. Homonuclear intervalence charge transfer transitions of $Fe^{2+}/Fe^{3+}$and Ti^{3+}/Ti^{4+}, along with the intervalence charge transfer between the edge sharing Fe^{2+} and Ti^{4+}, represent the loss mechanisms associated with these impurities. Furthermore, these transitions are often accompanied by different vacancy-type defects and antisite disorder for reasons related to local charge neutrality. Annealing treatments under different environments with different heating/cooling rates could be used to control the level of point defects in sapphire and spinel which in turn influences the probability of the impurity-associated intervalence charge transitions. Moreover, in both materials, large concentrations of alkali metals and alkaline earth metals have been observed and it is unclear how they can form compounds and defect clusters with the matrix atoms that may possibly lead to the absorption losses in the near-infrared. Similarly, other transition metals such as Cu, Ni, and Co have been previously reported to cause optical absorptions in the near-infrared in glass and ceramic materials but their roles in the case of sapphire and spinel still need to be investigated. The overall conclusion to be drawn from the results presented in this section is that trace element impurity concentrations in the starting materials used to manufacture window-grade sapphire and spinel must be reduced to improve optical transmission in the near infrared.

Table 4.6. Concentrations Different Trace Impurities Present in Spinel Samples

Concentration (ppm)	CN Disk 1	CN SQ 2	JHUAPL Disk
Na	204	179	N/A
K	182	60.8	N/A
Si	828	585	474
P	42.4	30.4	17.0
Ca	6925	6308	4499
Ti	1.33	1.08	11.1
V	0.256	0.183	0.405
Cr	6.19	7.22	6.82
Fe	133/129	540/190	202/58.5
Cu	2.46	1.15	0.239
Mo	0.457	0.412	0.109
Sn	0.148	0.116	0.142
Zn	21.4	17.7	13.1
Mn	2.32	2.16	1.32
Ni	5.28	2.23	1.81
Co	0.0962	0.0713	0.855

4.3.3 SIMS Results

SIMS measurements were carried out on extra-polished KO 1 surface to detect depth-resolved impurity concentrations due to polishing and the results are shown in Fig. 4.4. Data from the first few nanometers is related to instrumental artifacts and both C and Si show a small number density variation with the depth within the first 20 nm. It is reasonable to expect that both C and Si have a higher concentration near the surface if they originate from polishing slurries. Although Cl has been identified as a common chemical element in different polishing slurries, the concentration of Cl appears to be low and does not change with depth suggesting its existence in the bulk rather than being introduced during polishing. It is useful to identify impurity elements that exist near the surface as later we will see from Raman spectroscopy and SEM imaging analysis that different surface defects are decorated with these impurities.

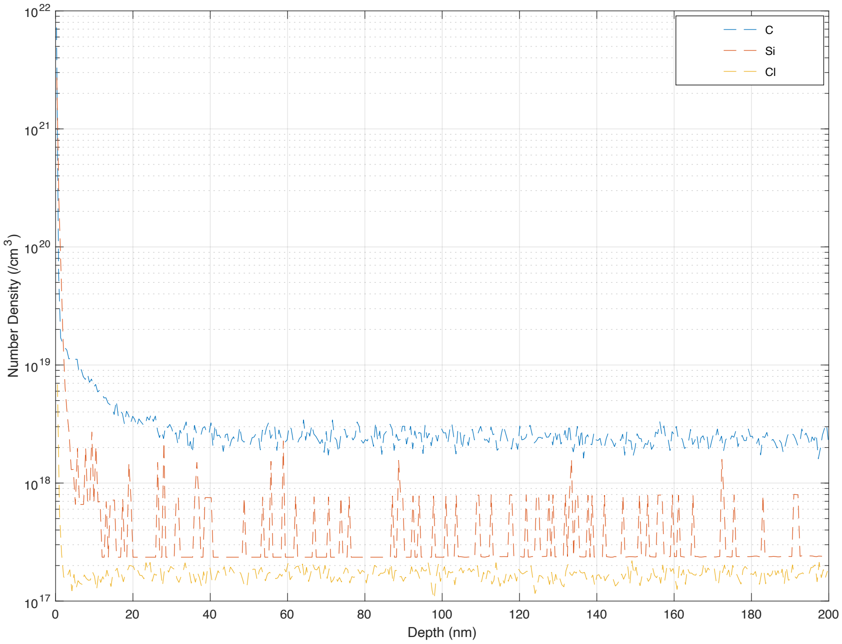

Figure 4.4. Number density of surface impurity elements C, Si, and Cl are plotted against the depth under the surface in blue, orange, and yellow broken lines, respectively.

4.3.4 Raman Spectroscopy Results

Raman spectroscopy was performed on different sapphire and spinel samples to identify surface defect morphology and chemistry. All samples were cleaned with acetone and ethanol solutions to ensure a clean surface without any artifacts introduced during materials handling. On sapphire samples, dark spots as well as agglomerates with sizes ranging from submicron to a few microns were observed, see Fig. 4.5. The Raman spectra of these sapphire samples indicate some special chemistries other than Al_2O_3. In addition to spectral peaks related to Al_2O_3 between 200 to 800 cm^{-1}, other small peaks were observed in the longer wavenumber region and were identified as being related to silica and graphite/diamond [156]–[158]. The origin of these impurities is believed to be the polishing solutions used during grinding and polishing processes where these materials are commonly found. Interestingly, after KO 1 had undergone a secondary polishing process, black agglomerates were detected on its surface and a relatively large background was observed in their associated Raman spectrum named "KO 1 Pre-heating" which is shown in Fig. 4.5b. It is possible that the agglomerates' origin was the polishing pitch used during the process as it contained organic compounds that may lead to a large background in the Raman spectrum. These organic compounds often have a low melting points (a few hundred degrees Celsius) so an annealing treatment at 300 °C in an oxidizing environment was used to "clean" the KO 1 surface. On the surface of the heat-treated KO 1, dark spots still remain while organic agglomerates appear to have disappeared, see Fig. 4.5b. The Raman spectrum of the surface indicates that these dark spots are associated with Si or C-related compounds though the peak intensities are weak.

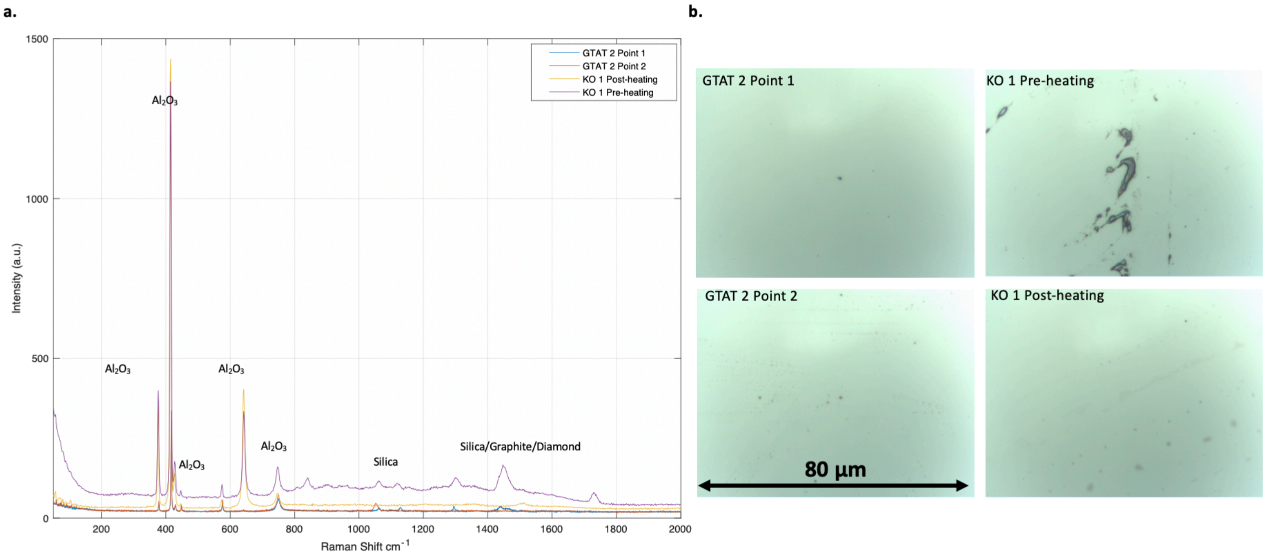

Figure 4.5. Raman spectrum of impurity features observed on different sapphire surfaces are shown in (a). Optical micrographs of impurity features associated with each Raman spectra are shown in (b).

Similar Raman spectra were collected from different spinel surfaces and the results are shown in Fig. 4.6. Similar to sapphire surfaces, impurity spots associated with Si and C were also found on spinel surfaces and these were likely related to polishing since similar chemical solutions are used for polishing sapphire and spinel. Raman spectra with large backgrounds were also noticed as some surface impurities were possibly related to organic compounds. As mentioned in Section 3.3.4, a secondary polishing of CN SQ 2 was performed and the newly polished surface exhibited groups of black dot features that were not observed on the CN SQ 1 surface. The Raman spectrum of this feature, shown in Fig. 4.6a under the name "CN SQ 2 Point 2," contains a strong peak near 1050 cm^{-1} which could be associated with silica since colloidal silica solutions are commonly used to grind and polish optical materials.

Based on the sapphire and spinel surfaces studied in this work, it would appear that surfaces of commercially-available optical windows materials are not as clean as they should be even though they appear to be flawless to human eyes under visible light. These particle-like features and aggregates have sizes extending from hundreds of nanometers to tens of microns which are comparable to the laser wavelengths used to study optical scattering. Additionally, these artifacts also have their own chemistries that lead to refractive index mismatches which ultimately result in scattering losses. Some organic compounds may also lead to surface absorbance in the near-IR wavelength region.

4.3.5 Optical and Electron Microscopies Results

In both Section 3.3.3 and Section 3.3.4, digs were observed on sapphire and spinel surfaces. When viewed using confocal microscopy using fluorescence mode, these digs fluoresced in the visible indicating they had special chemistries compared to the surrounding materials. Figure 4.7a includes a micrograph of a typical dig on a spinel surface. When illuminated by a laser operating at 488 nm, visible light emission in the range of 495 nm to 550 nm was detected and this is shown in Fig. 4.7b. No similar phenomenon was observed from other surface defects such as scratches and impurity particles but similar behavior has been found from digs on sapphire surfaces. Furthermore, the digs fluoresced even after sapphire samples were annealed at 1500 °C. One possible cause of the florescence might be related to impurity elements in the digs that are trapped during polishing. Both silica and nano diamonds that are commonly used in polishing solutions are known to fluoresce near 500 nm when excited at 488 nm [159]–[161]. While diamond decomposes at 763 °C, silica requires a temperature near 3000 °C. Therefore, the fact that the digs on the annealed sapphire surface fluoresced indicates a possibility of trapped silica at these sites.

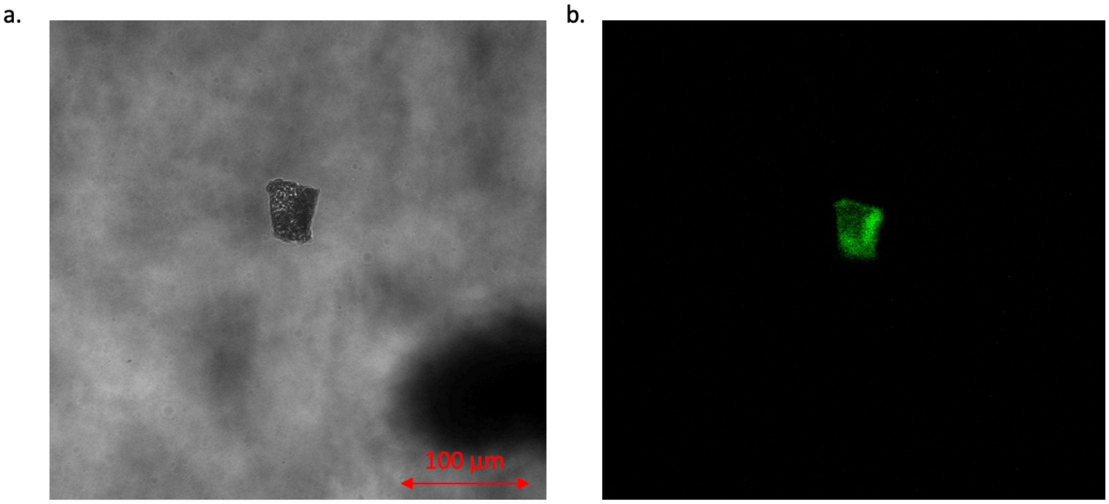

Figure 4.7. A confocal micrograph of a dig on JHUAPL disk under the transmission mode is shown in (a) and that under the fluorescence mode is shown in (b).

When a material is under high-energy electron bombardment from a source, electrons can be promoted from a lower-energy valence band to a higher-energy conduction band. When these electrons return back to the valence state, they can be trapped at the states introduced from both intrinsic and extrinsic defects. When this happens, energy is emitted at a specific wavelength from the falling of electrons to their ground state, resulting in luminescence. Using a CL detector in the SEM system, structural defects and impurities can be imaged. A set of SEM images using a secondary electron (SE) detector and a CL detector were collected from Guild 1*[1] and are shown in Fig. 4.8. Figures 4.8a and 4.8b show normal SEM images while Figs. 4.8c and 4.8d present the images collected from the same spots (corresponding to Fig. 4.8a and 4.8b respectively) using a CL detector and a 10-kV beam energy. In Fig. 4.8c and 4.8d, shallow scratches/striations and impurity particles exist on the sample surface that are not imaged using the regular SE detector. One possible explanation for this phenomenon is that these defects have special chemistries (i.e. Si or C) that emit photons at visible wavelengths and generate secondary electrons that have very

---

[1] This is another Guild sample with the same physical conditions as these of Guild 1.

low energies that are not readily detected. Furthermore, as seen in Fig. 4.8d, several thin scratches are crossed above a wide, scratch-like feature, suggesting these defects overlapped at different layers. Lastly, when the electron beam energy increased to 30 kV, some fuzzy, particle-like features appeared from the sub-surface and these are shown in Fig. 4.8e.

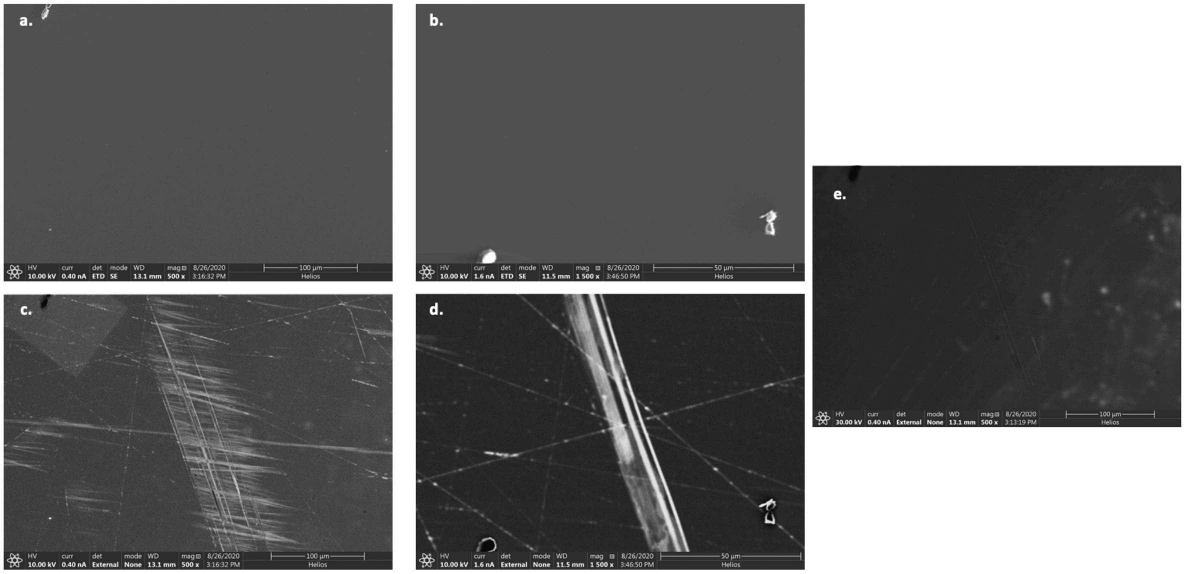

Figure 4.8. SEM micrographs taken on different locations on Guild 1 using a SE detector are shown in (a) and (b); images taken on the same locations using a CL detector are shown in (c) and (d); an image taken using a CL detector with a 30-kV beam energy is shown in (e).

Similar SEM-SE and SEM-CL images were acquired from extra-polished GTAT 1 and CN SQ 2*[2] and they are shown in Figs. 4.9 and 4.10. In Fig. 4.9, the extra-polished GTAT 1 had almost no scratch/striation features and had fewer impurity particles. However, using the CL detector, line features emerged under the surface as is shown in Fig 4.9b using a 10-kV beam energy and Fig. 4.9 c using a 30-kV beam energy. Owning to their large scales, these features were likely to be planar defects with impurities being segregated along them. For CN SQ 2*, not many features were observed on the surface beyond the embedded impurities shown in Figs. 4.10a and 4.10b.

---

[2] This is another CN SQ sample with the same physical conditions as these of CN SQ 2.

Similar impurity morphology was observed on the sample surface using the confocal microscope and the impurities are likely to be silica-related.

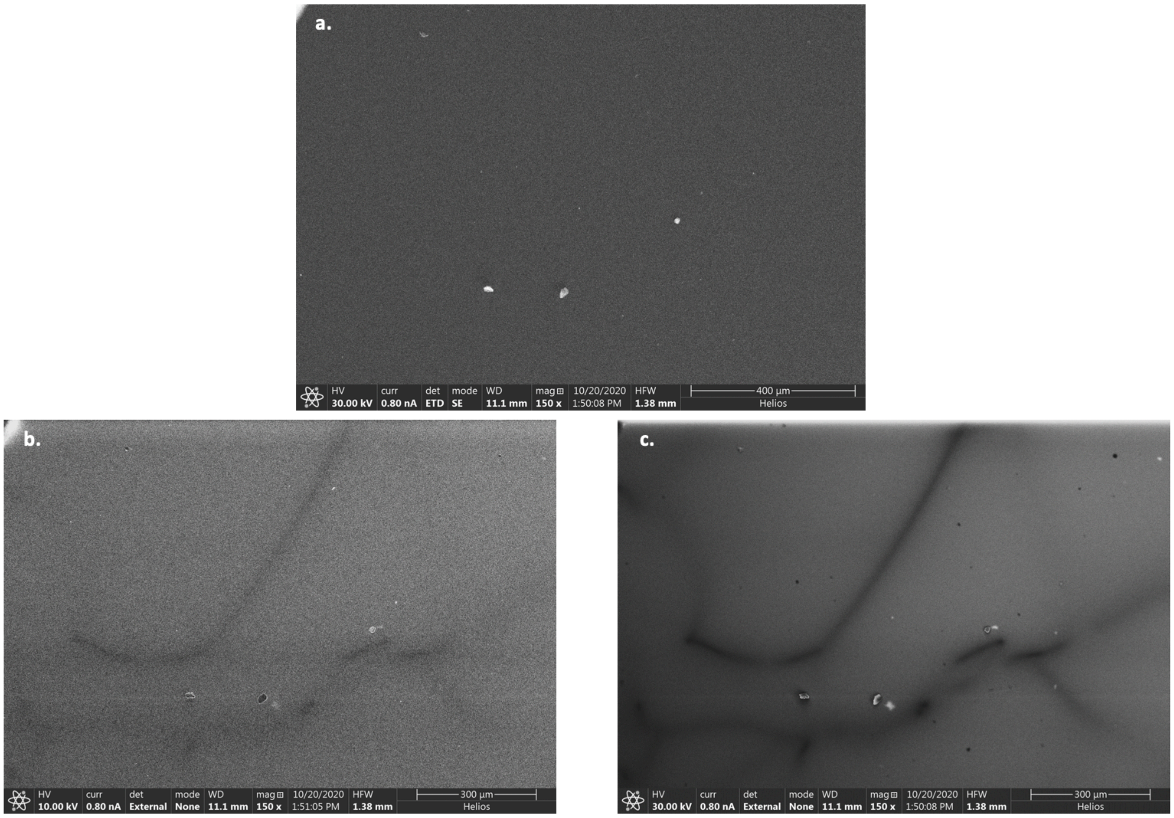

Figure 4.9. SEM micrograph taken from further polished GTAT 1 using a SE detector is shown in (a); images taken on the same location using a CL detector with a beam energy of 10 kV and 30 kV are shown in (c) and (d), respectively.

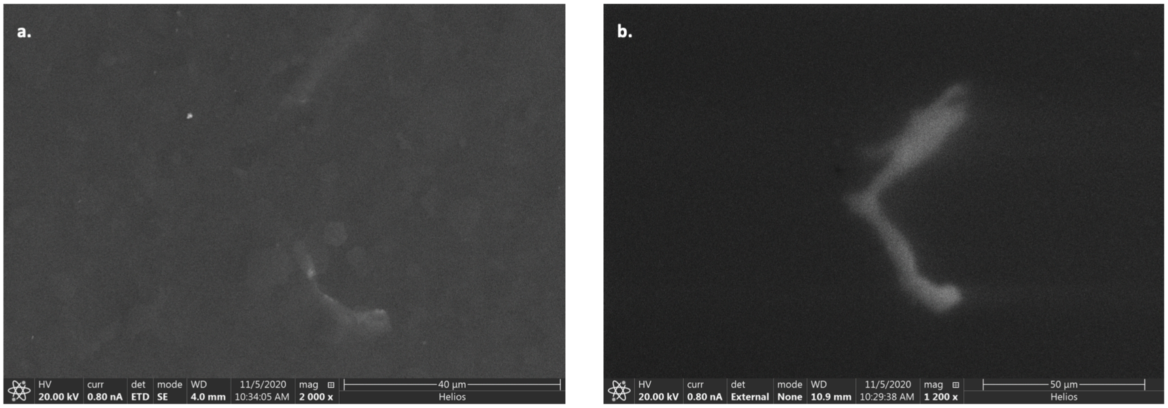

Figure 4.10. SEM micrograph taken from CN SQ 2* using a SE detector is shown in (a); image taken on the same location using a CL detector with a beam energy of 20 kV is shown in (b).

Cross sections from the three samples used for SEM imaging were acquired using FIB and were used for TEM imaging analysis. The goal was to further investigate the subsurface regions to identify any defects due to grinding and polishing. TEM images of the three cross sections are shown in Fig. 4.11. The top of the surface in each image represents the sample surface. As-received Guild 1* material was imaged and the related micrograph in Fig. 4.11a shows various structural defects present under its surface. As previously discussed in Section 3.3.2, dislocations, planar defects, and block misorientations could be introduced by polishing within the first 50 μm under sapphire surface. For Guild 1*, these types of defects were confirmed at a relatively shallow depth, and these findings are in an good agreement with previous reports [98]. Also present in Fig. 4.11a are fringes caused by sample thickness (thick, fuzzy lines) and Bragg contrast (thin lines), but these are common TEM imaging artifacts. Also, minor bend contours were observed, and these are possibly related to sample deformation. Sapphire is known to contain a small amount of residual stress during growth and this stress could be relieved during FIB material removal.

By contrast, not many sub-surface defect structures were found from extra-polished GTAT 1 as is indicated by the micrograph in Fig. 4.11b, but two planar defects (or cracks) appeared at the bottom right of the sample. These defects either already existed in the sample or were created when the internal stress became relieved during sample preparation. No apparent sub-surface and bulk defects were found in CN SQ 2^* as is indicated by the micrograph in Fig. 4.11c. However, several bend contours were observed on individual grains and they stopped at grain boundaries. These features suggest that some incoherencies may occur at the grain boundaries which are related to either residual stress or a chemical environment difference. A residual stress analysis has been performed on CN SQ 2 using a high energy X-ray diffractometer at EAG Laboratories and the number is reported to be -46.1 MPa. Considering the stress optics coefficient for materials such as spinel and sapphire (which is approximately in the 1/TPa range), the change of the refractive index due to the residual stress is very small in the case of CN SQ 2* [18]. Therefore, residual stress is less likely to be a main contributor to the scattering loss in spinel but the amount of the stress could lead to other large-scale structural defects that are associated with the optical losses. Additional details of the residual stress measurement can be found in Appendix A.

The different TEM images of sapphire and spinel indicate that defects at a micron scale exist both at the sub-surface and in the bulk. Based on the results obtained using Guild 1* and extra-polished GTAT 1, it appears that secondary polishing might reduce sub-surface damage associated with grinding and polishing, but more measurements need to be performed to generate a more complete understanding of polishing effects. Scattering losses from these defects are very likely at 1 μm and surface preparations of these window materials must be undertaken with great care.

4.4 Conclusion

In this Chapter, different materials characterization techniques were used to study different types of defects in sapphire and spinel. From the PALS study, it was shown that samples with both higher levels of V_o and V_{Al}-related defects also show a higher surface absorbance at three different wavelengths where PCI measurements were performed. Defect complexes in the near-surface region composed of vacancy clusters as well as dislocations that are introduced during surface grinding and polishing operations affect both optical absorbance and positron lifetimes. From LA-ICP-MS measurements, HEM grown sapphire with higher Ti and Fe concentrations were found to have a larger absorption loss at 1.064 μm. Previous studies indicated that this residual near-IR absorption is related to intervalence charge transfer between Ti^{3+}/Ti^{4+}, Fe^{2+}/Fe^{3+}, and Fe^{2+}/Ti^{4+}.

For sapphire that was grown in an oxidizing environment, its near-IR absorption loss increased due to oxidation of different impurity elements. Similar mechanisms were also found to be responsible for the low, near-IR absorption loss in different spinel samples. SIMS results showed that Si and C were the main surface impurities of polished sapphire, while Raman spectroscopy revealed that the observed surface defects were also associated with Si and C compounds. Finally, SEM-CL and TEM images confirmed the existence of sub-surface damage and bulk defects in sapphire and spinel samples though more data need to be acquired to obtain a statistically meaningful description of these defects. Defects observed from the surface and sub-surface have sizes ranging from hundreds of nanometers to tens of micrometers and ultimately contribute to the measured scatterance losses of sapphire and spinel in this study.

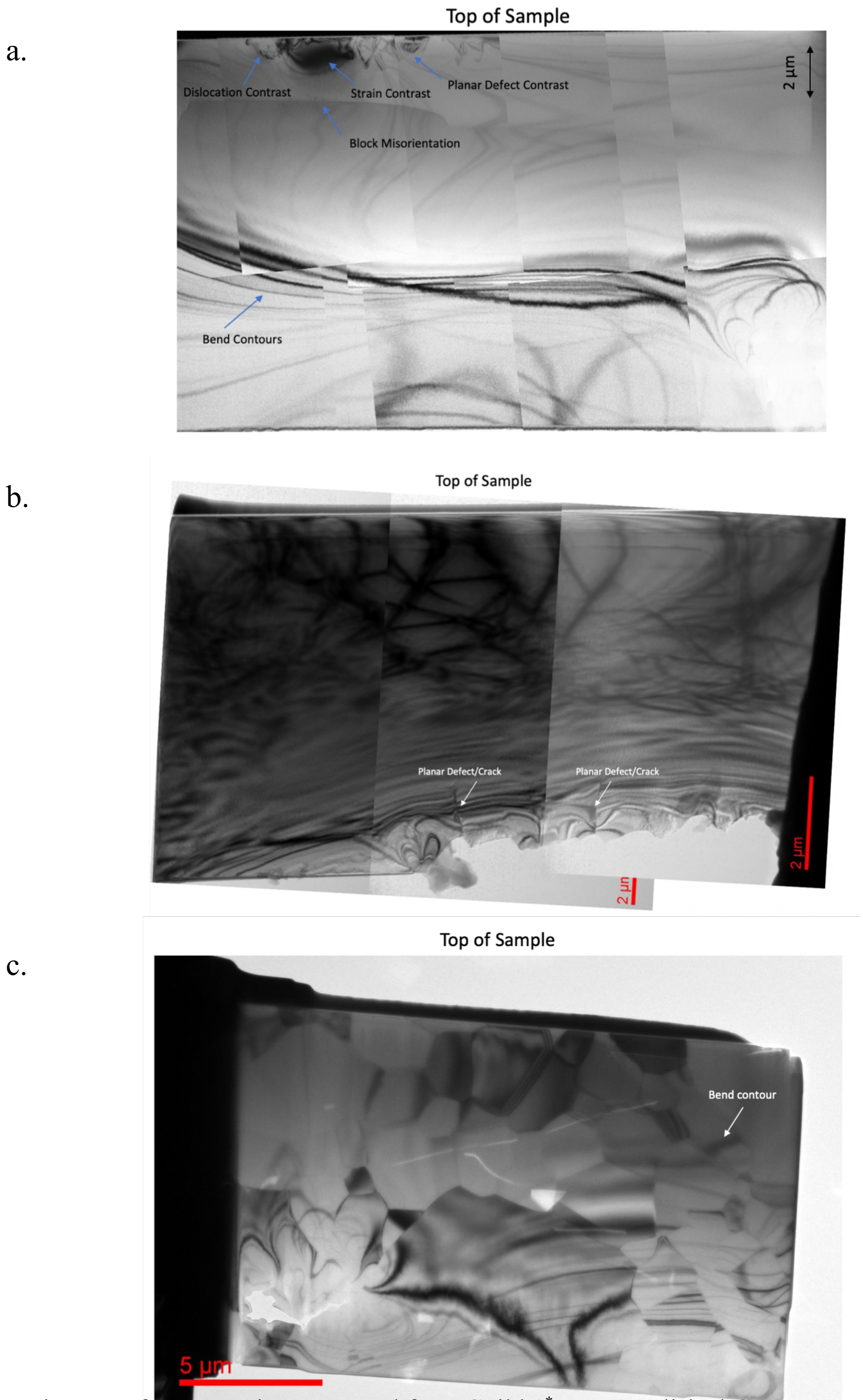

Figure 4.11. TEM images of cross sections prepared from Guild 1*, extra- polished GTAT 1, and CN SQ 2* are shown in (a), (b), and (c), respectively.

Chapter 5 Conclusion

For sapphire and spinel to be considered as the window materials for the next generation of HEL, their optical losses must be reduced to a level that is less than or equal to 1 ppm at the operating wavelength. As illustrated in this work, at 1.064 μm, the lowest absorption coefficient among all materials was found to be at 10^{-5} cm and the lowest scatterance at 10^{-5}. These losses must be reduced in these materials by at least a factor of 10 to satisfy the projected operating requirements for HELs. **Throughout this study, it has been found that the defects contributing to both types of loss are extrinsic, which means there are likely methods that can be developed to minimize or eliminate them during the manufacturing process.**

Different trace impurity elements and vacancy-type defects have been observed in both sapphire and spinel samples. Most of these impurities originate from the raw powder used to synthesize the final product. Powder treatments have been shown to effectively reduce the impurity concentration level but could not completely eliminate these impurities. As discussed in Chapter 4, even 1 ppb level of certain impurities could result in absorption loss of 1 ppm. Even if the impurity concentration is decreased, the homogeneity of the impurity distribution within the sample should also be inspected for large windows. Optical polishing of sapphire and spinel should also be carefully done as it introduces new surface impurities to these materials that result in absorption losses. Both cationic and anionic vacancies were found to be prevalent in these materials due to different growth atmospheres and parameters. Although vacancy concentrations can be changed through annealing or growing in a specific environment, the oxidation/reduction state of different impurity elements should also be monitored since these could lead to additional absorption loss. **Polishing-induced contamination, dislocations and vacancies were found to be correlated**

with sapphire surface absorbance and these types of defects could be reduced through improvements to surface preparation techniques.

Scattering of single-crystal sapphire was found to be dominated by surface-related effects while that of polycrystalline spinel appeared to be bulk dominated. Scratches, digs, and surface impurities were found on sapphire and spinel even after a secondary polishing process. Given many of their sizes being comparable to 1.064 μm, they contributed to the scattering losses observed in different samples. Moreover, some of the extra-polished sapphire also exhibited inhomogeneous surface topography resulting in scatterance variations across the sample surface. Additionally, different sub-surface damage has been observed in sapphire samples in both as-received and extra-polished conditions. **Although a finer polishing process could eliminate or reduce surface scratches and digs, it is not clear if it also mitigates the problems associated with sub-surface damage since polishing often results in structural defects near the surface.**

In spinel, a large scattering loss has been observed and the primary cause was shown to be related to grain boundaries. Impurities trapped at the boundaries induce changes of refractive index that result in a milky appearance that arises from multiple scattering events. Although sintering aids could be used to reduce grain boundary scattering, a residual scattering loss due to these aids could still occur. **Also, no apparent pores were observed in all spinel samples but they could still exist at a much smaller size though, in that case, they would contribute less to the total scatterance** [110]**.** To reduce the scatter level in sapphire and spinel samples, the surface must be characterized after every grinding and polishing step to ensure a minimal defect content.

For future studies, more samples with known growth parameters should be characterized to seek quantitative relationships between different defects and loss levels. While it might be easier to produce a small, nearly defect-free sapphire or spinel sample, much more effort is clearly required to manufacture a large window. Indeed, sapphire has been once considered as a mirror substrate candidate for laser interferometers such as Advanced LIGO and Virgo to detect gravitational waves. However, due to its 10 to 100 ppm/cm level of optical absorption and the inhomogeneity of defect distribution, the final substrate choice became fused silica since it has a better optical performance [162], [163]. Yet, the exact mechanisms behind the weak absorption loss still remain unclear at this point although findings suggest the localized absorption is linked to the change in the refractive index in that region [163]. **Therefore, to fully understand the observed defect mechanisms, more in-depth defect analysis must be conducted.**

Appendices

Appendix A: Residual Stress Measurement of Spinel Using X-ray Diffraction

Method

The CN SQ 2 sample was mounted using double-sided adhesive tape on an Al stub which was subsequently mounted to a goniometric stage with x, y, z, phi, and psi motions on the diffractometer. XRD data was collected by a coupled theta/two theta scan on a Bruker D8 Discover diffractometer equipped with a micro-focus copper X-ray tube with Montel optics, 0.5 mm collimator, and a Vantec 500 2D area detector. Unlike traditional point detectors, the 2D detector accepts diffraction from crystallites oriented in a wide variety of tilt angles with respect to the incident X-ray beam. This results in reasonable diffraction intensity even though the spot size analyzed is very small. With no collimation around the 2D detector, the peak positions are very sensitive to sample height. To ensure that the sample height is correct, the diffractometer employs a laser and camera system oriented so that the sample is in the correct position when the laser beam is in the center of the camera system. The sample was oscillated 2 mm in both the X and Y directions to average over a larger area on the sample.

Result

Residual stress of a material can be determined by collecting symmetric theta/two-theta XRD patterns of a specific crystallographic reflection at various Psi angles where the sample is tilted with respect the X-ray source and detector. Residual stress will cause the position of the peak to shift with increasing sample tilt (Psi angle). Ideally, a well resolved peak at a high angle is used as the sensitivity to changes in peak position increases with increasing two-theta angle. The peaks at different Psi angles are profile fit and the d-spacing of the peaks are plotted vs the corresponding

Sin^{2}Psi value. A linear regression line is fit to the data points and the Sin^{2}Psi plot and the residual stress are calculated using the slope of the line and the elastic constants of the material (Young's modulus and Poisson ratio). A Young's modulus of 276 GPa and a Poisson ratio of 0.26 was used to calculate the residual stress.

The highest angle peak that could be used for this analysis was the spinel (840) reflection located near 117.1 degrees two-theta. An overlay of the XRD data collected at 7 different Psi angles are shown for the sample in Fig. 6.1. From the overlay plot, the (840) peak appears to shift to higher angle as the Psi value increases. Each pattern was subsequently profile fit to obtain the d-sapcing information. The Sin^{2}Psi residual stress plot is shown in Fig. 6.2. The regression line shows a very slight negative slope with increasing sin^{2}psi value indicating a small compressive stress in present in the material. The residual stress is calculated to be -46.1 MPa from the regression line and elastic constants.

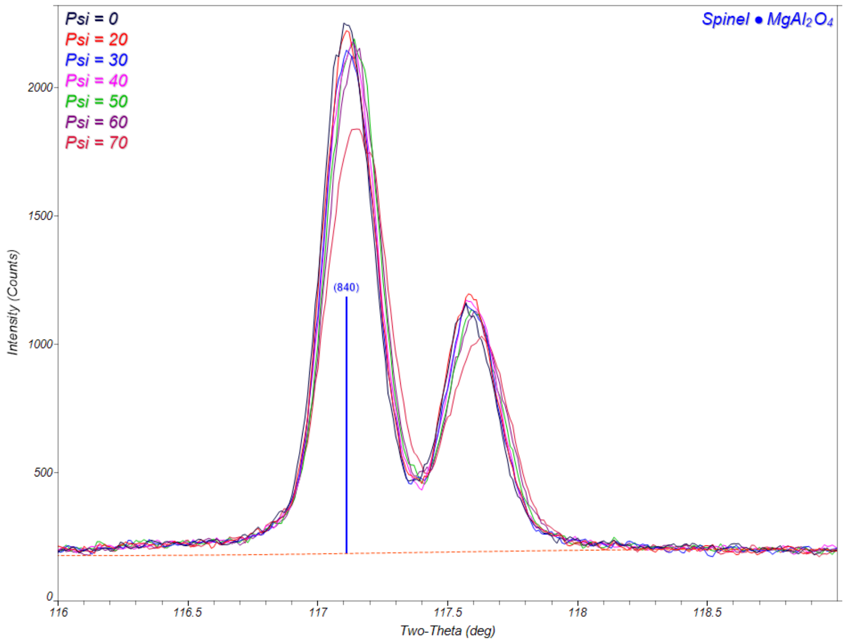

Figure 6.1 An overlay of the XRD data of CN SQ 2 collected at 7 different Psi angles for the (840) reflection peak at 117 degrees

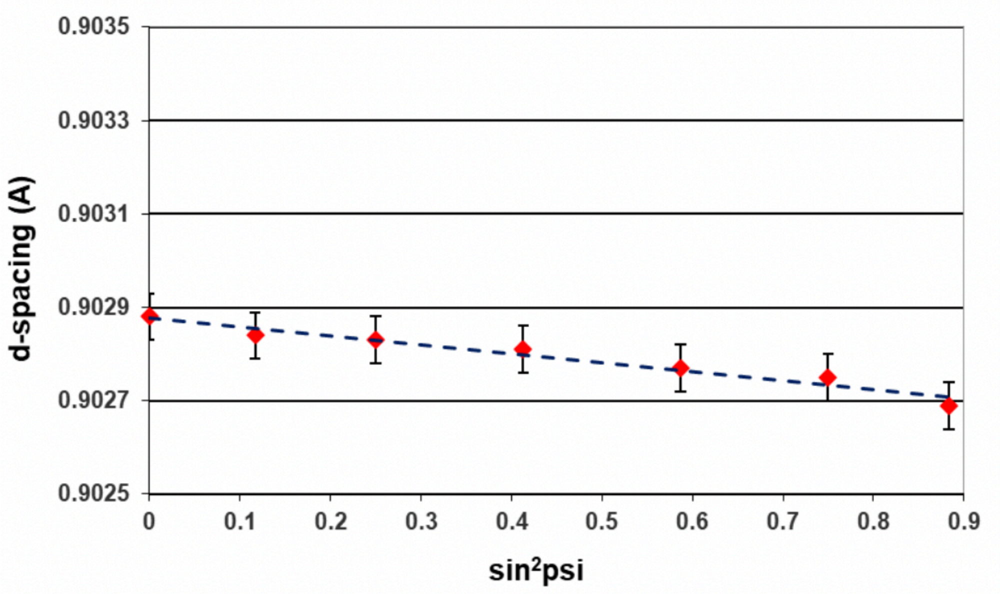

Figure 6.2 Measured d-spacing at each Psi rotation is plotted with $\sin^2$(Psi)

References

[1] G. P. Perram, M. A. Marciniak, and M. Goda, “High energy laser weapons: technology overview,” *Laser Technol. Def. Secur.*, vol. 5414, no. September, pp. 1–25, 2004.

[2] D. H. Kiel, “Is this the time for a high-energy laser weapon program?,” *Opt. Eng.*, vol. 52, no. 2, p. 021008, 2012.

[3] M. J. Lavan and J. J. Wachs, “U.S. Army High Energy Laser (HEL) technology program,” *Technol. Opt. Countermeas. VIII*, vol. 8187, no. October 2011, p. 818704, 2011.

[4] J. Sanghera *et al.*, “Transparent ceramics for high-energy laser systems,” *Opt. Mater. (Amst).*, 2011.

[5] F. C. Beach and I. R. McNab, “Present and Future Naval Applications for Pulsed Power,” *IEEE Pulsed Power*, pp. 1–7, 2005.

[6] M. E. Thomas, “Low-level background absorption in durable window materials,” in *Proc.of SPIE*, 2017, vol. 10179, p. 101790B.

[7] J. Ma, M. E. Thomas, P. McGuiggan, and J. Spicer, “Weak absorption and scattering losses from the visible to the near infrared in single-crystal sapphire materials,” *Opt. Eng.*, vol. 59, no. 8, p. 087101, 2020.

[8] C. A. Klein, “Figures of merit for high-energy laser-window materials: thermal lensing and thermal stresses,” in *Proc.SPIE Laser-Induced Damage in Optical Materials 6403*, 2006, p. 640308.

[9] C. A. Klein, “Materials for high-energy laser windows: how thermal lensing and thermal stresses control the performance,” *Opt. Mater. Struct. Technol. III*, vol. 6666, no. September 2007, p. 66660Z, 2007.

[10] Y. Niu, W. Liu, H. Liu, C. Wang, H. Niu, and D. Man, “Design and comparison of laser windows for high-power lasers,” *High-Power Lasers Appl. VII*, vol. 9266, no. November 2014, p. 92660B, 2014.

[11] M. E. Thomas, *Optical Propagation in Linear Media*. Oxford University Press, 2006.

[12] D. L. Wood, “Weak Absorption Tails in Amorphous Semiconductors,” *Phys. Rev. B*, vol. 5, no. 8, pp. 3144–3151, 1972.

[13] W. J. Chung, B. J. Park, H. S. Seo, J. T. Ahn, M. H. Lee, and Y. G. Choi, “Effects of the weak absorption tail on the transmission loss of Ge-Sb-Se optical fibers,” *J. Am. Ceram. Soc.*, vol. 88, no. 5, pp. 1205–1208, 2005.

[14] M. E. Thomas, D. M. Brown, and J. B. Spicer, “Requirements for a high energy laser window and components,” in *Electromagnetic Window Symposium (EMWS)*, 2018, pp. 1–7.

[15] C. A. Klein, “Figures of merit for high-energy laser-window materials: thermal lensing and thermal stresses,” *Proc. SPIE*, vol. 640308, no. January 2007, 2017.

[16] E. R. Dobrovinskaya, L. A. Lytvynov, and V. Pishchik, *Sapphire: Material, Manufacturing, Applications*. 2009.

[17] C. A. Klein and R. L. Gentilman, “Flexural strength of sapphire: measurements performed at SoRI, UMass, and UDRI,” in *Proc. SPIE 4452, Inorganic Optical Materials III*, 2001, vol. 4452, no. November 2001, pp. 66–84.

[18] R. Waxler and E. Farbaugh, “Photoelastic Constants of Ruby,” *J Res Nat Bur Stand Sect A Phys Chem*, vol. 74 A, no. 2, pp. 215–220, 1970.

[19] M. V. Parish, M. R. Pascucci, J. J. Gannon, and D. C. Harris, “Strength characteristics of transparent alumina and spinel ceramics,” *Wind. Dome Technol. Mater. XV*, vol. 10179,

no. May 2017, p. 101790G, 2017.

[20] E. Bruschini, S. Speziale, G. B. Andreozzi, F. Bosi, and U. Hålenius, "The elasticity of MgAl2O4-MnAl2O4 spinels by Brillouin scattering and an empirical approach for bulk modulus prediction," *Am. Mineral.*, vol. 100, no. 2–3, pp. 644–651, 2015.

[21] H. Harder *et al.*, "Fracture of Polycrystalline MgAl2O4," *J. Am. Ceram. Soc.*, vol. 1978, no. 31, pp. 619–623, 1980.

[22] D. C. Harris *et al.*, "Refractive index of infrared- transparent polycrystalline alumina," *Opt. Eng.*, vol. 56, no. 7, 2020.

[23] W. J. Tropf and M. E. Thomas, "Aluminum Oxide (Al2O3) Revisited," in *Handbook of Optical Constants of Solids III*, E. D. Palik, Ed. Academic Press, 1998, pp. 651–682.

[24] W. J. Tropf and M. E. Thomas, *Handbook of Optical Constants of Solids II*. Orlando: Academic Press, 1991.

[25] J. Stover, *Optical Scattering: Measurement and Analysis*. SPIE, 2012.

[26] D. J. Lockwood, *Encyclopedia of Color Science and Technology*. 2016.

[27] M. S. Akselrod and F. J. Bruni, "Modern trends in crystal growth and new applications of sapphire," *J. Cryst. Growth*, vol. 360, no. 1, pp. 134–145, 2012.

[28] G. Wang *et al.*, "Preparation, quality characterization, service performance evaluation and its modification of sapphire crystal for optical window and dome application," *Mater. Des.*, vol. 31, pp. 706–711, 2010.

[29] H. Tang, H. Li, and J. Xu, "Growth and Development of Sapphire Crystal for LED Applications," in *Advanced Topics on Crystal Growth*, InTech, 2013.

[30] J. D. Katz, "Microwave Sintering," *Annu. Rev. Mater. Sci.*, vol. 22, pp. 153–170, 1992.

[31] G. Villalobos *et al.*, "Low absorption magnesium aluminate spinel windows for high energy laser applications," *J. Mater. Res.*, vol. 29, no. 19, pp. 2266–2271, 2014.

[32] W. Kim *et al.*, "Overview of transparent optical ceramics for high-energy lasers at NRL," *Appl Opt*, vol. 54, no. 31, pp. F210-21, 2015.

[33] M. Sokol, M. Halabi, S. Kalabukhov, and N. Frage, "Nano-structured MgAl2O4spinel consolidated by high pressure spark plasma sintering (HPSPS)," *J. Eur. Ceram. Soc.*, vol. 37, no. 2, pp. 755–762, 2017.

[34] M. E. Innocenzi, R. T. Swimm, M. Bass, R. H. French, A. B. Villaverde, and M. R. Kokta, "Room-temperature optical absorption in undoped α-Al2O 3," *J. Appl. Phys.*, vol. 67, p. 7542, 1990.

[35] J. Carrasco, J. R. B. Gomes, and F. Illas, "Theoretical study of bulk and surface oxygen and aluminum vacancies in α-Al2O3," *Phys. Rev. B - Condens. Matter Mater. Phys.*, vol. 69, no. 6, pp. 1–13, 2004.

[36] J. Xu *et al.*, "Microdefects in Al2O3 films and interfaces revealed by positron lifetime spectroscopy," *Appl. Phys. Lett.*, vol. 71, no. 21, pp. 3165–3167, 1997.

[37] B. D. Evans and M. Stapelbroek, "Optical properties of the F+ center in crystalline Al2O3," *Phys. Rev. B*, vol. 18, no. 12, pp. 7089–7098, 1978.

[38] K. P. D. Lagerlo and R. W. Grimes, "The Defect Chemistry of Sapphire (a-Al2O3)," *Acta Mater.*, vol. 46, no. 16, pp. 5689–5700, 1998.

[39] K. . and Lee and J. H. J. Crawford, "Luminescence of the F center in sapphire," *Phys. Rev. B*, vol. 19, no. 6, pp. 3217–3221, 1979.

[40] V. T. Gritsyna, I. V. Afanasyev-Charkin, V. A. Kobyakov, and K. E. Sickafus, "Structure and electronic states of defects in spinel of different compositions MgO·nAl2O3:Me," *J. Am. Ceram. Soc.*, vol. 82, no. 12, pp. 3365–3373, 1999.

[41] L. S. Cain, G. J. Pogatshnik, and Y. Chen, “Optical transitions in neutron-irradiated MgA1204 spinel crystals,” *Phys. Rev. B*, vol. 37, no. 5, pp. 2645–2652, 1988.

[42] T. A. Bazilevskaya, V. T. Gritsyna, D. V. Orlinski, L. V. Udalova, and A. V. Voitsenya, “The effect of composition, processing conditions, and irradiation, on lattice defects in spinel ceramics,” *J. Nucl. Mater.*, vol. 253, no. 1–3, pp. 133–140, 1998.

[43] X. Xiang, G. Zhang, X. Wang, T. Tang, and Y. Shi, “A new perspective on the process of intrinsic point defects in α-Al2O3,” *Phys. Chem. Chem. Phys.*, vol. 17, no. 43, pp. 29134–29141, 2015.

[44] M. Izerrouken, Y. Djouadi, and H. Zirour, “Annealing process of F- and F+-centers in Al2O 3 single crystal induced by fast neutrons irradiation,” *Nucl. Instruments Methods Phys. Res. Sect. B Beam Interact. with Mater. Atoms*, vol. 319, pp. 29–33, 2014.

[45] S. Kawaminami, K. Mochizuki, S. Hashimoto, N. Adachi, and T. Ota, “Coloration of Ti-doped sapphire grown by the flame-fusion method,” *J. Asian Ceram. Soc.*, vol. 1, no. 4, pp. 362–367, 2013.

[46] M. H. Lewis, “Defects in spinel crystals grown by the verneuil process,” *Philos. Mag.*, vol. 14, no. 131, pp. 1003–1018, 1966.

[47] A. Ibarra, F. J. Lopez, and M. J. de Castro, “V centers in MgA12O4 spinels,” *Phys. Rev. B*, vol. 44, no. 14, pp. 7256–7262, 1991.

[48] F. Benabid, M. Notcutt, V. Loriette, L. Ju, and D. G. Blair, “X-ray induced absorption of high-purity sapphire and investigation of the origin of the residual absorption at 1064 nm,” *J. Phys. D. Appl. Phys.*, vol. 33, no. 6, pp. 589–594, 2000.

[49] E. R. Dobrovinskaya, L. A. Litvinov, and V. V. Pishchik, “Morphology and structural perfection of shaped sapphire,” *J. Cryst. Growth*, vol. 50, no. 1, pp. 341–344, 1980.

[50] C. J. Ting and H. Y. Lu, “Hot-pressing of magnesium aluminate spinel - II. Microstructure development,” *Acta Mater.*, vol. 47, no. 3, pp. 831–840, 1999.

[51] A. Rothman, S. Kalabukhov, N. Sverdlov, M. P. Dariel, and N. Frage, “The effect of grain size on the mechanical and optical properties of spark plasma sintering-processed magnesium aluminate spinel MgAl2O 4,” *Int. J. Appl. Ceram. Technol.*, vol. 11, no. 1, pp. 146–153, 2014.

[52] Y. Chiang and W. D. Kingery, “Grain-Boundary Migration in Nonstoichiometric Solid Solutions of Magnesium Aluminate Spinel: II, Effects of Grain-Boundary Nonstoichiometry,” *J. Am. Ceram. Soc.*, vol. 73, no. 5, pp. 1153–1158, 1990.

[53] N. Nuns, F. Béclin, and J. Crampon, “Grain-Boundary characterization in a nonstoichiometric fine-grained magnesium aluminate spinel: Effects of defect segregation at the space-charge layers,” *J. Am. Ceram. Soc.*, vol. 92, no. 4, pp. 870–875, 2009.

[54] A. F. Dericioglu and Y. Kagawa, “Effects of grain boundary microcracking on the light transmittance of sintered transparent MgAl2O4,” *J. Eur. Ceram. Soc.*, vol. 23, no. 6, pp. 951–959, 2003.

[55] M. Mark, H. Traxler, R. Schiftner, B. Kleinpaß, and W. Knabl, “Molybdenum and tungsten in sapphire crystal growth industry,” *Proc. 19th Plansee Semin. 2017*, pp. 1–12, 2017.

[56] E. A. Ghezal *et al.*, “Effect of pulling rate on bubbles distribution in sapphire crystals grown by the micropulling down (μ-PD) technique,” *Cryst. Growth Des.*, vol. 12, no. 8, pp. 4098–4103, 2012.

[57] H. Li, “Bubbles propagation in undoped and Titanium (Ti3 +) -doped sapphire crystals grown by Czochralski (Cz) technique,” Université Claude Bernard - Lyon I, 2014.

[58] A. Pille, "Annika Pille. Development of optically transparent alumina and spinel ceramics with fine microstruc- ture. Mechanics," Université Sorbonne Paris Cité, 2018.

[59] M. R. du Merac, "The role of impurities, LIF, and processing on the sintering, microstructure, and optical properties of transparent polycrystalline magnesium aluminate (MgAl2O4) spinel," Colorado School of Mines, 2014.

[60] G. Wang *et al.*, "Preparation, quality characterization, service performance evaluation and its modification of sapphire crystal for optical window and dome application," *Mater. Des.*, vol. 31, no. 2, pp. 706–711, Feb. 2010.

[61] B. S. Patel and Z. H. Zaidi, "The suitability of sapphire for laser windows," *Meas. Sci. Technol.*, vol. 10, no. 3, pp. 146–151, 1999.

[62] J. Ma, M. B. Airola, M. E. Thomas, and J. Spicer, "Measurements of weak scattering and absorption in spinel and sapphire from the near infrared to the visible," *Proc. SPIE*, vol. 10985, p. 1098502, 2019.

[63] N. Waasem *et al.*, "Photoacoustic absorption spectrometer for highly transparent dielectrics with parts-per-million sensitivity," in *Review of Scientific Instruments*, 2013, vol. 84, no. 2.

[64] M. Leidinger, S. Fieberg, N. Waasem, K. Buse, and I. Breunig, "Comparative study on three highly sensitive absorption measurement techniques characterizing lithium niobate over its entire transparent spectral range," vol. 23, no. 17, pp. 1324–1333, 2015.

[65] D. C. Harris *et al.*, "Optical and thermal properties of spinel with revised (increased) absorption at 4 to 5 μm wavelengths and comparison with sapphire," *Opt. Eng.*, vol. 52, no. 8, p. 87113, 2013.

[66] N. Waasem *et al.*, "Photoacoustic absorption spectrometer for highly transparent dielectrics with parts- per-million sensitivity Photoacoustic absorption spectrometer for highly transparent dielectrics with parts-per-million sensitivity," vol. 023109, 2013.

[67] S. Fieberg, N. Waasem, F. Kühnemann, and K. Buse, "Sensitive absorption measurements in bulk material and coatings using a photothermal and a photoacoustic spectrometer," *Proc. SPIE*, vol. 8964, p. 896410, 2014.

[68] P. Pellegrino, "Trace chemical vapor detection by photothermal interferometry," *Proc. SPIE*, vol. 4205, 2001.

[69] A. Alexandrovski, M. Fejer, A. Markosian, and R. Route, "Photothermal common-path interferometry (PCI): new developments," *Proc. SPIE*, vol. 7193, no. February 2009, p. 71930D, 2009.

[70] B. D. Evans, "Optical transmission in undoped crystalline α-Al2O 3 grown by several techniques," *J. Appl. Phys.*, vol. 70, p. 3995, 1991.

[71] B. D. Evans and M. Stapelbroek, "Optical properties of the F+ center in crystalline Al2O3," *Phys. Rev. B*, vol. 18, no. 12, pp. 7089–7098, 1978.

[72] H. H. Kusuma, B. Astuti, and Z. Ibrahim, "Absorption and emission properties of ruby (Cr:Al2O3) single crystal," *J. Phys. Conf. Ser.*, vol. 1170, no. 1, 2019.

[73] E. Loh, "Ultraviolet Absorption and Excitation Spectrum of Ruby and Sapphire," *J. Chem. Phys.*, vol. 44, no. 5, pp. 1940–1945, 1966.

[74] Y. Rugitani, K. Tagawa, and K. Kato, "Optical absorption spectra of iron (III) and chromium (III) doped in synthetic yttrium-aluminium-garnets (YAG)," *Mineral. J.*, vol. 7, no. 5, pp. 445–455, 1974.

[75] K. DeArmond and L. S. Forster, "Electronic transitions in chromium (III) complexes-I. Absorption spectra of β-diketone chelates," *Spectrochim. Acta*, vol. 19, no. 9, pp. 1393–

1401, 1963.

[76] M. E. Thomas and G. Hunt, "A computer code for modeling optical properties of materials II," in *Proc.SPIE 10985 Windows and Domes Technologies and Materials*, 2019, p. XVI 109850K.

[77] T. F. Deutsch, "Absorption coefficient of infrared laser window materials," *J. Phys. Chem. Solids*, vol. 34, no. 12, pp. 2091–2104, 1973.

[78] M. E. Thomas, *Optical Propagation in Linear Media: Atmospheric Gases and Particles, Solid-State Components, and Water*. Oxford University Press, 2006.

[79] D. Viechnicki and F. Schmid, "Crystal growth using the heat exchanger method (HEM)," *J. Cryst. Growth*, vol. 26, no. 1, pp. 162–164, 1974.

[80] D. Y. Smith and D. L. Dexter, "Optical Absorption Strengths of Defects in Insulators*: The f-Sum Rule, Smakula's Equation, Effective Fields, and Application to Color Centers in Alkali Halides," *Prog. Opt.*, vol. 10C, no. 165–228, 1972.

[81] D. L. Dexter, "Theory of the Optical Properties of Imperfections in Nonmetals," *Solid State Phys. - Adv. Res. Appl.*, vol. 6, no. C, pp. 353–411, 1958.

[82] F. Benabid, M. Notcutt, L. Ju, and D. G. Blair, "Rayleigh scattering in sapphire test mass for laser interferometric gravitational-wave detectors I. Measurement of scattering attenuation coefficient," *Opt. Commun.*, vol. 167, no. 1, pp. 7–13, 1999.

[83] M. Guillong and D. Günther, "Quasi 'non-destructive' laser ablation-inductively coupled plasma-mass spectrometry fingerprinting of sapphires," *Spectrochim. Acta - Part B At. Spectrosc.*, vol. 56, no. 7, pp. 1219–1231, 2001.

[84] A. Abduriyim and H. Kitawaki, "Applications of laser ablation-inductively coupled plasma-mass spectrometry (LA-ICP-MS) to gemology," *Gems Gemol.*, vol. 42, no. 2, pp. 98–118, 2006.

[85] H. Guo, C. Wu, H. Hu, D. Shi, J. Shi, and S. Hu, "Seed crystal producing device of sapphire crystal growing furnace," CN103572366A, 2012.

[86] J. K. Bristow, D. Tiana, S. C. Parker, and A. Walsh, "Defect chemistry of Ti and Fe impurities and aggregates in Al 2O3," *J. Mater. Chem. A*, vol. 2, no. 17, pp. 6198–6208, 2014.

[87] A. Sanchez, A. J. Strauss, R. L. Aggarwal, and R. E. Fahey, "Crystal Growth, Spectroscopy, and Laser Characteristics of Ti: Al," *IEEE J. Quantum Electron.*, vol. 24, no. 6, pp. 995–1002, 1988.

[88] W. R. Helms and J. G. Mullen, "Study of pure and doped cobaltous and nickelous oxide," *Phys. Rev. B*, vol. 4, no. 3, pp. 750–757, 1971.

[89] J. Tauc, A. Menth, and D. L. Wood, "Optical and magnetic investigations of the localized states in semiconducting glasses," *Phys. Rev. Lett.*, vol. 25, no. 11, pp. 749–752, 1970.

[90] D. L. Wood and J. Tauc, "Weak absorption tails in amorphous semiconductors," *Phys. Rev. B*, vol. 5, no. 8, pp. 3144–3151, 1972.

[91] H. Mori and T. Izawa, "A new loss mechanism in ultralow loss optical fiber materials," *J. Appl. Phys.*, vol. 51, no. 4, pp. 2270–2271, 1980.

[92] H. Hasegawa, Y. Kamimura, K. Edagawa, and I. Yonenaga, "Dislocation-related optical absorption in plastically deformed GaN," *J. Appl. Phys.*, vol. 102, no. 2, pp. 4–7, 2007.

[93] H. Iber, E. Peiner, and A. Schlachetzki, "The effect of dislocations on the optical absorption of heteroepitaxial InP and GaAs on Si," *J. Appl. Phys.*, vol. 79, no. 12, pp. 9273–9277, 1996.

[94] A. Kolyubakin, Y. Osip'yan, and S. Shevchenko, "Dislocation States in Germanium," *Zh.*

Eksp. Teor. Fiz, vol. 93, pp. 248–254, 1987.

[95] F. Seitz, “Speculations on the properties of the silver halide crystals,” *Rev. Mod. Phys.*, vol. 23, no. 4, pp. 328–352, 1951.

[96] T. Blue, F. Goldner, F. Poc, J. Greene, and R. Fielder, “Testing of Sapphire Optical Fiber and Sensors in Intense Radiation Fields, when Subjected to Very High Temperatures Proposal,” *NEUP Final Rep.*, 2012.

[97] T. Suratwala *et al.*, “Chemistry and Formation of the Beilby Layer during Polishing of Fused Silica Glass,” *J. Am. Ceram. Soc.*, vol. 98, no. 8, pp. 2395–2402, 2015.

[98] T. Saito, T. Hirayama, T. Yamamoto, and Y. Ikuhara, “Lattice strain and dislocations in polished surfaces on sapphire,” *J. Am. Ceram. Soc.*, vol. 88, no. 8, pp. 2277–2285, 2005.

[99] V. Quemener, L. Vines, E. V. Monakhov, and B. G. Svensson, “Electronic properties of vacancy related defects in ZnO induced by mechanical polishing,” *Appl. Phys. Lett.*, vol. 99, no. 11, pp. 8–11, 2011.

[100] L. E. Bausa, I. Vergara, and J. Garcis-Sole, “Laser-excited luminescence in Ti-doped MgAl2O4 spinel,” *J. Appl. Phys.*, vol. 68, no. 736–740, 1990.

[101] S. N. Qadri *et al.*, “Spinel optics for high energy lasers,” in *Proc. SPIE 10985, Window and Dome Technologies and Materials XVI, 1098508*, 2019, no. 1098508, pp. 1–10.

[102] A. F. Dericioglu, A. R. Boccaccini, I. Dlouhy, and Y. Kagawa, “Effect of chemical composition on the optical properties and fracture toughness of transparent magnesium aluminate spinel ceramics,” *Mater. Trans.*, vol. 46, no. 5, pp. 996–1003, 2005.

[103] A. Jouini *et al.*, “Ti-doped MgAl2O4 spinel single crystals grown by the micro-pulling-down method for laser application: Growth and strong visible blue emission,” *J. Mater. Res.*, vol. 21, no. 9, pp. 2337–2344, 2006.

[104] Z. Erlangung and D. Naturwissenschaften, “Interfaces in Transparent Polycrystalline MgAl2O4 Spinel,” Technische Universität Darmstadt, 2018.

[105] S. S. De Souza and A. R. Blak, “Defect simulation in MgAl2O4 spinels,” *Radiat. Eff. Defects Solids*, vol. 146, no. 1–4, pp. 123–129, 1998.

[106] I. Reimanis and H. J. Kleebe, “A review on the sintering and microstructure development of transparent spinel (MgAl 2O 4),” *J. Am. Ceram. Soc.*, vol. 92, no. 7, pp. 1472–1480, 2009.

[107] U. Hålenius, H. Skogby, and G. B. Andreozzi, “Influence of cation distribution on the optical absorption spectra of Fe3+-bearing spinel s.s.-hercynite crystals: Evidence for electron transitions in VIFe2+-VIFe3+ clusters,” *Phys. Chem. Miner.*, vol. 29, no. 5, pp. 319–330, 2002.

[108] S. T. Yang *et al.*, “Comparing the use of mid-infrared versus far-infrared lasers for mitigating damage growth on fused silica,” *Appl. Opt.*, vol. 49, no. 14, pp. 2606–2616, 2010.

[109] M. Seitz, N. Stoddard, B. Glick, and J. C. Stover, “Evaluation of sapphire at II-VI Optical Systems for HEL applications,” in *Proc. SPIE 10985, Window and Dome Technologies and Materials XVI,* 2019, vol. 1098507, no. May 2019, pp. 1–7.

[110] R. M. Springer, M. E. Thomas, and R. I. Joseph, “Analysis and Comparison of Single-Crystal and Polycrystalline Nd:YAG, Scatter,” *IEEE J. Quantum Electron.*, vol. 51, no. 8, p. 1700408, 2015.

[111] M. E. Thomas and D. D. Duncan, “BRDF and BSDF models for diffuse surface and bulk scatter from transparent windows,” *Proc. SPIE 6545, Wind. Dome Technol. Mater. X,* vol. 6545, p. 65450I, 2007.

[112] D. D. Duncan, D. V. Hahn, and M. E. Thomas, "Physics-based polarimetric BRDF models," *Proc.SPIE 5192, Opt. Diagnostic Methods Inorg. Mater. III*, vol. 5192, 2003.

[113] D. M. Aikens, "Meaningful surface roughness and quality tolerances," in *International Optical Design Conference and Optical Fabrication and Testing OSA Technical Digest (CD)*, 2010, p. ITuD3.

[114] I. T. Lewis, A. G. Ledebuhr, and M. L. Bernt, "Stray-light implications of scratch/dig specifications," *Opt. Scatt. Appl. Meas. Theory.SPIE.*, vol. 1530, no. December 1991, pp. 22–34, 1991.

[115] B. Bussiere, N. Sanner, M. Sentis, and O. Uteza, "Importance of surface topography on pulsed laser-induced damage threshold of Sapphire crystals," *Sci. Rep.*, vol. 7, no. 1, pp. 1–10, 2017.

[116] O. Kienzle, J. Staub, and T. Tschudi, "Light scattering from transparent substrates: Theory and experiment," *Phys. Rev. B*, vol. 50, no. 3, pp. 1848–1860, 1994.

[117] E. Fest, *Stray Light Analysis and Control*. SPIE, 2013.

[118] M. B. Airola, M. E. Thomas, J. Ma, D. V. Hahn, C. Hibbitts, and D. Blaney, "Angle dependent scatter in CVD ZnSe and single crystal CaF2 from the infrared through the NIR," in *Proc. SPIE 10985,* 2019, p. 1098504.

[119] G. I. Finch, "The Beilby layer on non-metals [2]," *Nature*, vol. 138, no. 3502. p. 1010, 1936.

[120] J. A. Randi, J. C. Lambropoulos, and S. D. Jacobs, "Subsurface damage in some single crystalline optical materials," *Appl. Opt.*, vol. 44, no. 12, pp. 2241–2249, 2005.

[121] G. I. Finch, "The Beilby Layer on Non-Metals," *Nature*, vol. 138, p. 1010, 1936.

[122] W. L. Cong, P. F. Zhang, and Z. J. Pei, "Experimental investigations on material removal rate and surface roughness in lapping of substrate wafers: A literature review," *Key Eng. Mater.*, vol. 404, pp. 22–31, 2009.

[123] O. Weis, "Direct contact superpolishing of sapphire," *Appl. Opt.*, vol. 31, no. 22, p. 4355, 1992.

[124] B. Hader and O. Weis, "Superpolishing Sapphire: A Method to Produce Atomically Flat and Damage Free Surfaces," *Surf. Sci.*, vol. 220, pp. 118–130, 1989.

[125] W. C. JOHNSON, D. F. STEIN, and R. W. RICE, "Analysis of Grain-Boundary Impurities and Fluoride Additives in Hot-Pressed Oxides by Auger Electron Spectroscopy," *J. Am. Ceram. Soc.*, vol. 57, no. 8, pp. 342–344, 1974.

[126] W. Kim *et al.*, "Low Loss Spinel Windows for High Energy Lasers," in *Proc. of SPIE Window and Dome Technologies and Materials XIV 9453*, 2015.

[127] I. Ganesh, S. Bhattacharjee, B. P. Saha, R. Johnson, and Y. R. Mahajan, "A new sintering aid for magnesium aluminate spinel," *Ceram. Int.*, vol. 27, no. 7, pp. 773–779, 2001.

[128] S. Roy, H. Lingertat, C. Brecher, and V. Sarin, "Optical Properties of Anisotropic Polycrystalline Ce+3 activated LSO," *Opt Mater (Amst).*, vol. 35, no. 5, pp. 827–832, 2013.

[129] J. G. J. Peelen and R. Metselaar, "Light scattering by pores in polycrystalline materials: Transmission properties of alumina," *J. Appl. Phys.*, vol. 45, no. 1, pp. 216–220, 1974.

[130] C. J. Liu and E. F. Sieckmann, "Refractive index of calcium oxide," *J. Appl. Phys.*, vol. 37, no. 6, pp. 2450–2452, 1966.

[131] X. Hu, T. Koyanagi, Y. Katoh, and B. D. Wirth, "Positron annihilation spectroscopy investigation of vacancy defects in neutron-irradiated 3C-SiC," *Phys. Rev. B*, vol. 95, no. 10, pp. 1–11, 2017.

[132] R. T. Cox, “Electron spin resonance studies of holes trapped at Mg2+, Li+ and cation vacancies in Al2O3,” *Solid State Commun.*, vol. 9, no. 22, pp. 1989–1992, 1971.
[133] K. H. Lee, G. E. Holmberg, and J. H. Crawford, “Optical and ESR studies of hole centers in γ-irradiated Al2O3,” *Phys. Status Solidi*, vol. 39, no. 2, pp. 669–674, 1977.
[134] G. Zhang, Y. Lu, and X. Wang, “Hydrogen interactions with intrinsic point defects in hydrogen permeation barrier of α-Al2O3: A first-principles study,” *Phys. Chem. Chem. Phys.*, vol. 16, no. 33, pp. 17523–17530, 2014.
[135] G. Molnár *et al.*, “Photoluminescence and thermoluminescence of titanium ions in sapphire crystals,” *Radiat. Meas.*, vol. 33, no. 5, pp. 663–667, 2001.
[136] S. E. Kulkova, L. Y. Zagorskaya, and I. R. Shein, “Electronic structure of α-Al 2O 3 in the bulk and on the surface,” *Russ. Phys. J.*, vol. 48, no. 11, pp. 1127–1133, 2005.
[137] G. Moya, J. Kansy, A. Si Ahmed, J. Liebault, F. Moya, and D. Gæuriot, “Positron lifetime measurements in sintered alumina,” *Phys. Status Solidi Appl. Res.*, vol. 198, no. 1, pp. 215–223, 2003.
[138] H. E. Schaefer and M. Forster, “As-grown metal oxides and electron-irradiated Al2O3 studied by positron lifetime measurements,” *Mater. Sci. Eng. A*, vol. 109, no. C, pp. 161–167, 1989.
[139] N. Djourelov *et al.*, “Structure characterization of spark plasma sintered alumina by positron annihilation lifetime spectroscopy,” *Phys. Status Solidi Appl. Mater. Sci.*, vol. 208, no. 4, pp. 795–802, 2011.
[140] J. C. Han *et al.*, “Neutron irradiation and post annealing effect on sapphire by positron annihilation,” *Appl. Radiat. Isot.*, vol. 68, no. 9, pp. 1699–1702, 2010.
[141] K. P. Muthe *et al.*, “Positron annihilation and thermoluminescence studies of thermally induced defects in α-Al2O3 single crystals,” *J. Phys. D. Appl. Phys.*, vol. 42, no. 10, 2009.
[142] M. Hornak, “Energetics, Kinetics, and Optical Absorption of Point Defects in Sapphire,” The Ohio State University, 2016.
[143] M. Eldrup and B. N. Singh, “Studies of defects and defect agglomerates by positron annihilation spectroscopy,” *J. Nucl. Mater.*, vol. 251, pp. 132–138, 1997.
[144] G. Dlubek, “Positron Studies of Decomposition Phenomena in Al Alloys,” *Mater. Sci. Forum*, vol. 13–14, pp. 11–32, 1987.
[145] F. A. Selim, M. H. Weber, D. Solodovnikov, and K. G. Lynn, “Nature of native defects in ZnO,” *Phys. Rev. Lett.*, vol. 99, no. 8, pp. 1–4, 2007.
[146] C. H. Qiu, C. Hoggatt, W. Melton, M. W. Leksono, and J. I. Pankove, “Study of defect states in GaN films by photoconductivity measurement Study of defect states in GaN films by photoconductivity measurement,” *Appl. Phys. Lett.*, vol. 66, no. 2712, pp. 1–4, 1995.
[147] C. Hidalgo, G. González-Doncel, S. Linderoth, and J. San Juan, “Structure of dislocations in Al and Fe as studied by positron-annihilation spectroscopy,” *Phys. Rev. B*, vol. 45, no. 13, 1992.
[148] A. R. Moon and M. R. Phillips, “Defect Clustering and Color in Fe,Ti: alpha-Al2O3,” vol. 77, no. 2, pp. 356–367, 1994.
[149] W. Thiemsorn, K. Keowkamnerd, P. Suwannathada, H. Hessenkemper, and S. Phanichaphant, “Redox ratio and optical absorption of polyvalent ions in industrial glasses,” *Bull. Mater. Sci.*, vol. 30, no. 5, pp. 487–495, 2007.
[150] X. Zhang, A. Brenier, J. Wang, and H. Zhang, “Absorption cross-sections of Cr4+:YAG at 946 and 914 nm,” *Opt. Mater. (Amst).*, vol. 26, no. 3, pp. 293–296, 2004.

[151] M. Marchiò, M. Leonardi, M. Bazzan, and R. Flaminio, “3D characterization of low optical absorption structures in large crystalline sapphire substrates for gravitational wave detectors,” *Sci. Rep.*, pp. 1–8, 2021.

[152] P. O. Nilsson and G. Forssell, “Optical properties of calcium,” *Phys. Rev. B*, vol. 16, no. 8, pp. 3352–3358, 1977.

[153] H. H. Glascock and E. B. Hensley, “Fundamental optical absorption, electrical conductivity, and thermoelectric power of calcium oxide,” *Phys. Rev.*, vol. 131, no. 2, pp. 649–652, 1963.

[154] V. D’Ippolito, G. B. Andreozzi, U. Hålenius, H. Skogby, K. Hametner, and D. Günther, “Color mechanisms in spinel: cobalt and iron interplay for the blue color,” *Phys. Chem. Miner.*, vol. 42, no. 6, pp. 431–439, 2015.

[155] C. R. M. Jackson *et al.*, “Visible To Near-Infrared Spectra of Iron-Bearing Spinel With Application To Sinus Aestuum and Lunar Spinel Anorthosite,” *Am. Mineral.*, vol. 99, pp. 1821–1833, 2014.

[156] V. Volovšek, K. Furić, L. Bistričić, and M. Leskovac, “Micro raman spectroscopy of silica nanoparticles treated with aminopropylsilanetriol,” *Macromol. Symp.*, vol. 265, no. 1, pp. 178–182, 2008.

[157] L. Ruggiero *et al.*, “Raman and ATR FT-IR investigations of innovative silica nanocontaniers loaded with a biocide for stone conservation treatments,” *arXiv*, pp. 1–11, 2019.

[158] J. R. Dennison and M. Holtz, “Raman spectroscopy of carbon materials,” *Spectrosc. (Santa Monica)*, vol. 11, no. 8, pp. 38–46, 1996.

[159] A. van Blaaderen and A. Vrij, “Synthesis and Characterization of Colloidal Dispersions of Fluorescent, Monodisperse Silica Spheres,” *Langmuir*, vol. 8, no. 12, pp. 2921–2931, 1992.

[160] J. Neauport, P. Cormont, P. Legros, C. Ambard, and J. Destribats, “Imaging subsurface damage of grinded fused silica optics by confocal fluorescence microscopy,” *Opt. Express*, vol. 17, no. 5, p. 3543, 2009.

[161] S. R. Hemelaar *et al.*, “Nanodiamonds as multi-purpose labels for microscopy,” *Sci. Rep.*, vol. 7, no. 1, pp. 1–9, 2017.

[162] E. Hirose *et al.*, “Characterization of Core Optics in Gravitational-Wave Detectors: Case Study of KAGRA Sapphire Mirrors,” *Phys. Rev. Appl.*, vol. 14, no. 1, p. 1, 2020.

[163] E. Hirose *et al.*, “Sapphire mirror for the KAGRA gravitational wave detector,” *Phys. Rev. D - Part. Fields, Gravit. Cosmol.*, vol. 89, no. 6, pp. 1–7, 2014.

Curriculum Vitae

Jessica Ma
jma42@jhu.edu
Certified PMP, Six Sigma Green Belt

EDUCATION

Johns Hopkins University (JHU), Baltimore, MD
Master of Science in Materials Science and Engineering, Dec 2017
Doctor of Philosophy in Materials Science and Engineering, Mar 2021

Worcester Polytechnic Institute (WPI), Worcester, MA
Bachelor of Science in Mechanical Engineering with Honor, Concentration in Material Science, May 2015

RESEARCH AND TECHNICAL EXPERIENCES

Johns Hopkins University Applied Physics Laboratory (JHUAPL) Laurel, MD, US
Ph.D. Candidate August 2015-Present
Weak Absorption and Scattering in High-Energy Laser (HEL) Materials
Sponsored by JHUAPL

- Utilize laser based non-destructive techniques to evaluate weak optical loss in HEL window materials.
- Analyze experimental data by using different analytics tools to seek the underlying mechanisms that cause weak loss phenomena.
- Perform various materials characterizations including AFM, Raman spectroscopy, and UV-VIS, etc. to study materials' physical properties
- Use physical models to explain and predict optical properties of laser window materials.

Improvements in Thermal Battery Capabilities Sponsored by Missile Defense Agency

- Developed a novel nickel-aluminum mesh-structured pyrotechnic through the electroless deposition method

Syntek Technologies, Inc and Naval Research Laboratory (NRL) Washington, DC, US
Technical Consulting Intern June 2018-May 2019

- Synthesis of Transparent Spinel by Using Microwave Sintering
- Collaborated with scientists at NRL to generate transparent spinel materials using the microwave sintering technique.
- Performed various materials characterization including SEM, XRD, and EDS to evaluate physical properties.

Materials Processing Center, Massachusetts Institute of Technology (MIT) Cambridge, MA, USA
Summer Research Intern June 2014-August 2014

- Worked on the project funded by U.S. Department of Energy to measure the residual stress of nuclear canister plate welds in the field which that susceptible to stress corrosion crack.
- Led a team of three to utilize various material characterization techniques to measure the residual stress including XRD and finite element analysis.

OTHER PROJECT EXPERIENCES

Electronic Waste Recycling Tirana, Albania
Interactive Qualifying Project, WPI October 2013-December 2013

- Assisted a local NGO to promote electronic waste recycling in Albania.

- Improved organization’s current promotional materials and created new materials using Microsoft Word, PowerPoint and Adobe Photoshop. Helped the organization to recruit at least 20 new partners.

Green Initiatives at the Museum of Russian Icons Clinton, MA, USA
Great Problem Seminar, WPI August 2011-December 2011

- Worked on an interdisciplinary team of five to assess the Museum of Russian Icons for its sustainability and energy efficiency based on a LEED standard.
- Utilized an energy audit checklist to analyze the museum environment and collected data by using environmental test instruments such as infrared camera.
- Proposed suggestions on the energy efficiency improvement of the museum.

PUBLICATIONS

J. Ma, C.Li, X.Hu, M.E. Thomas, B.Wirth, J.B. Spicer (2020). “Correlation between vacancy defects and optical properties of synthetic sapphire revealed by positron lifetime spectroscopy”, *Optics Materials Express*, Under Review

J. Ma, M.E. Thomas, P. McGuiggan, J.B. Spicer (2020). “Weak absorption and scattering losses from the visible to the near infrared in single-crystal sapphire materials”, *Optical Engineering*, 59(8), 87-101

Ma J, Airola MB, Thomas ME, Spicer JB (2019). “Measurements of weak scattering and absorption in spinel and sapphire from the near infrared to the visible.”, *Proc. SPIE 10985, Window and Dome Technologies and Materials XVI, 1098504 (13 May 2019);*

M. B. Airola, M. E. Thomas, J. Ma, D. V. Hahn, K. Hibbitts, D. Blaney, “Angle dependent scatter in CVD ZnSe and single crystal CaF2 from the infrared through the NIR.*”, Proc. SPIE 10985, Window and Dome Technologies and Materials XVI, 1098504 (13 May 2019);*

M. E. Thomas, J. Ma,M. B. Airola, P. McGuiggan,"Nondestructive characterization of aged paper using spectral and directional reflection measurements", *Proc. SPIE 10750, Reflection, Scattering, and Diffraction from Surfaces VI, 107500F* (4 September 2018).

Sa, Q., Gratz, E., Heelan, J. A., Ma, S., Apelian, D., & Wang, Y. (2016). “Synthesis of Diverse LiNi$_x$Mn$_y$Co$_z$O2 Cathode Materials from Lithium Ion Battery Recovery Stream”, *Journal of Sustainable Metallurgy*, *2*(3), 248-256.

ORAL PRESENTATIONS

Weak Absorption and Scattering Losses in Single-Crystal Sapphire Windows Due to Bulk and Surface Defects, *2020 Annual Directed Energy S&T Symposium, West Point*, NY, March 2020

Characterization of Weak Scattering and Absorption in Sapphire and Spinel from the Near Infrared to the Visible, *2019 SPIE: Defense+Commercial Sensing,* Baltimore, MD, April 2019

Weak Scattering and Absorption in Sapphire and Spinel from the UV to the IR Region, *2019 Annual Directed Energy S&T Symposium, Destin*, FL, April 2019

POSTER PRESENTATIONS

Effects of Surface Polishing on Surface Scatter in Single-Crystal Sapphire Window Materials, *17th Electromagnetic Window Symposium, Newark, DE,* May 2020

Weak Absorption and Scattering Losses from the Visible to the Near-Infrared in Single-Crystal Sapphire Grown by Different Techniques, *FIO+LS*, Washington D.C., September 2019

Synthesis of Highly Transparent Spinel by Using Microwave Sintering, *2019 Annual Directed Energy S&T Symposium, Destin*, Poster Session, FL, April 2019

Fabrication and Characterization of High Performance, Cost Effective Ni-Al Pyrotechnic Microcomposites, *2018 National Space and Missile Materials Symposium*, Poster Session, Madison, WI, June 2018.